

WAKE VORTEX ALLEVIATION USING RAPIDLY ACTUATED SEGMENTED GURNEY FLAPS

by

Claude G. Matalanis and John K. Eaton

Prepared with support from the
The Stanford Thermal and Fluid Sciences Affiliates and the Office of Naval Research

Report No. 102

Flow Physics and Computation Division
Department of Mechanical Engineering
Stanford University
Stanford, CA 94305-3030

January 2007

© Copyright 2007 by Claude G. Matalanis
All Rights Reserved

Abstract

All bodies that generate lift also generate circulation. The circulation generated by large commercial aircraft remains in their wake in the form of trailing vortices. These vortices can be hazardous to following aircraft due to their strength and persistence. To account for this, airports abide by spacing rules which govern the frequency with which aircraft can take-off and land from their runways when operating in instrument flight rules. These spacing rules have become the limiting factor on increasing airport capacity, and with the increases in air travel predicted for the near future, the problem is becoming more urgent.

One way of approaching this problem is active wake alleviation. The basic idea is to actively embed perturbations in the trailing vortex system of an aircraft which will excite natural instabilities in the wake. The instabilities should result in a wake which is benign to following aircraft in less time than would normally be required, allowing for a reduction in current spacing rules. The main difficulty with such an approach is in achieving perturbations large enough to excite instability without significantly degrading aircraft performance.

Rapidly actuated segmented Gurney flaps, also known as Miniature Trailing Edge Effectors (MiTEs), have shown great potential in solving various aerodynamic problems. Previous work has shown that they can create a large increment in the section lift coefficient of an airfoil local to the spanwise position where they are actuated. Thus, MiTEs may be used to actively alter the shape of a wing lift distribution. This suggests that they might also be useful for active wake alleviation.

We conducted an experimental and computational study to assess the potential for using MiTEs for active wake vortex alleviation. Wind tunnel tests were performed on a half-span model NACA 0012 wing equipped with an array of 13 independent MiTE pairs. The chord-based Reynolds number was around 350,000. Each MiTE could extend 0.015 chord lengths perpendicular to the freestream on the pressure side of the wing. Pressure profiles and a five-hole probe survey in the near wake were used to examine the influence that the MiTEs had upon the wing aerodynamics and the vortex rollup process. Static and dynamic particle image velocimetry (PIV) were used to measure the static and time-dependent response of the vortex in the intermediate wake to various MiTE actuation schemes. These experiments showed that the MiTEs were capable of deflecting the vortex in both the spanwise and lift

directions. A maximum spanwise deflection of 0.041 chord lengths was possible while nearly conserving lift.

The dynamic PIV results combined with results from the pressure profiles and a five-hole probe survey in the intermediate wake were used to form complete, experimentally-based initial conditions for vortex filament computations that were used to compute the far wake evolution. Results from these computations showed that the perturbations created by MiTEs could be used to excite a variety of three-dimensional inviscid vortex instabilities.

Finally, the research performed on MiTEs led to the development of a new, more practical wake alleviation device: the spanwise actuating Gurney flap. A prototype of this device was designed and tested. The tests showed that the same types of perturbations as were seen with the MiTEs could be achieved with this device.

Acknowledgements

This work was sponsored by the Stanford Graduate Fellowship and the Stanford Thermal and Fluid Sciences Affiliates. Also, much of the laboratory equipment used in this work was funded by the Office of Naval Research. We are deeply thankful for the sponsorship of these organizations.

We would like to acknowledge Joo Hyun Lee, George Nelson, and Emin Issakhanian for their help in the laboratory. Also, Dr. Steven Rennich and Dr. Sanjiva Lele assisted us by providing the computational software necessary for this work. Finally, this work would not have been possible without the efforts of our professional machinist, Lakhbir Johal, and our administrative assistant, Amy Osugi. Their help has been invaluable.

Contents

Abstract	iii
Acknowledgements	v
List of Tables	ix
List of Figures	x
Nomenclature	xv
1 Introduction	1
1.1 The Wake Vortex Hazard	1
1.2 Previous Work	4
1.2.1 Detection and Avoidance	6
1.2.2 Passive Wake Alleviation	7
1.2.3 Active Wake Alleviation	11
1.2.4 Other Vortex Instability Work	16
1.3 Miniature Trailing Edge Effectors	17
1.4 Objectives	20
2 Experimental Apparatus and Methods	21
2.1 Experimental Model and Facilities	21
2.1.1 Half-Span Wing	21
2.1.2 MiTEs	24
2.1.3 Wind Tunnel	31
2.2 Measurement Apparatus	32
2.2.1 Pressure Profiles	32
2.2.2 Five-Hole Probe	36
2.2.3 Particle Image Velocimetry	40
2.3 Experimental Uncertainty	48
2.3.1 Pressure Profile Uncertainty	48
2.3.2 Five-Hole Probe Uncertainty	49

2.3.3	PIV Uncertainty	52
3	Experimental Results	53
3.1	Wing Aerodynamic Characteristics	53
3.1.1	Neutral Case	53
3.1.2	MiTE Effects	53
3.2	Near Wake Flow Structure	61
3.2.1	Mean Flow Field Modification	61
3.2.2	Secondary Structures	65
3.3	Intermediate Wake Steady-State Measurements	69
3.4	Intermediate Wake Dynamic Response	80
3.4.1	Active Scheme Design	80
3.4.2	Vortex Transient Response	82
4	Computational Results	88
4.1	Computational Approach	88
4.1.1	Vortex Filament Technique	88
4.1.2	Generation of Initial Conditions	92
4.2	Model Scale Case	93
4.3	Full Scale Cases	97
4.3.1	Three Representative Vortex Configurations	97
4.3.2	One Pair Case	100
4.3.3	Two Pair Co-Rotating Case	100
4.3.4	Two Pair Counter-Rotating Case	101
5	Novel Wake Alleviation Device	112
5.1	Spanwise Actuating Gurney Flap	112
5.1.1	Detailed Prototype Design and Fabrication	114
5.1.2	Wing Aerodynamic Effects	117
5.1.3	Intermediate Wake Results	117
6	Conclusions and Recommendations	121
6.1	Summary of Conclusions	121
6.1.1	Alteration of Lift Distribution	121
6.1.2	Near Wake Effects	122

6.1.3	Intermediate Wake Effects	122
6.1.4	Far Wake Effects	123
6.1.5	Spanwise Actuating Gurney Flap	124
6.2	Recommendations	124
6.3	Closing Remarks	126
A	Calibration of Five-Hole Probe	127
B	Camera Upstream Effect	134

List of Tables

1.1	Spacing matrix given in nautical miles for IFR conditions on a single runway.	4
2.1	Airfoil coordinates.	22
2.2	Logic chart for MiTE control.	29
2.3	Pressure tap locations along the chord of the wing. The upstream most point is omitted on the suction side.	34
2.4	Pressure tap locations along the span of the wing.	34
2.5	Calculated vortex center location (spanwise coordinate only) as filter size is increased.	48
2.6	The uncertainties in pressure profile measurements.	50
3.1	Comparison of measured section lift and drag coefficients to tabulated data.	54
3.2	Increment in lift compared to the neutral case.	61
3.3	Flap configurations for the three active schemes.	82
4.1	Computational parameters for the model scale case.	93
4.2	Computational parameters for the full scale cases.	98

List of Figures

1.1	Schematic depiction of trailing vortices near an airport.	2
1.2	The triangular flap wing used by Ortega et al. Figure reproduced from Ortega et al. (2003).	9
1.3	The passively excited instability examined by Ortega et al. Figure reproduced from Ortega et al. (2003).	10
1.4	The apparatus used by Durston et al. Figure reproduced from Durston et al. (2003).	11
1.5	Late stages of the Crow instability.	12
1.6	Two-dimensional cut of the line vortex systems previously examined. . . .	14
1.7	A Gurney flap on a NACA 0012 airfoil with a blunt trailing edge.	18
1.8	Unsteady behavior associated with rapid flap actuation shown by Solovitz and Eaton. Figure reproduced from Solovitz (2004).	19
2.1	Schematic of the airfoil cross-section.	23
2.2	The wing and MiTEs mounted in the wind tunnel test section.	25
2.3	CAD rendering of the MiTEs used by Solovitz and Eaton (2002)	25
2.4	Schematic of the airfoil and actuator cross-section. All dimensions are given in mm.	26
2.5	Two dimensional view of a MiTE in the XZ plane.	27
2.6	Three dimensional view of a MiTE.	27
2.7	A rear oblique view of the fully-assembled wing equipped with MiTEs. . . .	28
2.8	The bidirectional H-bridge for relaying power to one MiTE pair. It is shown here as it appears on the PCB, dotted lines indicate the opposite side of the PCB.	30
2.9	The mechanical response of the four flaps closest to the tip at test conditions.	31
2.10	Illustration of the parameters used to quantify the MiTE configuration. . .	32
2.11	The location of pressure taps on the wing. Taps are on both the pressure and suction sides. Dimensions are given in mm.	33
2.12	The five-hole probe as it was oriented in the wind tunnel.	37
2.13	Schematic of the five-hole probe control box and surrounding equipment. . .	38
2.14	Circuit diagram of the single-polarity switch for powering the solenoid valves.	39

2.15	Schematic of the entire experimental apparatus configured for PIV.	41
2.16	Picture of the test section configured for PIV experiments.	41
2.17	The optical beam path.	42
2.18	The calibration target used for PIV.	44
2.19	Sample calibration image.	44
2.20	The timing of a dynamic PIV sample.	45
2.21	Two histograms from a typical vector field showing the effect of sub-pixel accuracy equalization.	47
3.1	The spanwise lift distribution for the clean wing at three angles of attack. The uncertainty in C_l is smaller than the symbol size.	54
3.2	The spanwise drag distribution for the clean wing at three angles of attack. The uncertainty in C_d is smaller than the symbol size.	55
3.3	The streamwise pressure coefficient distribution at the spanwise station closest to the root ($Y/a = 0.081$) for the neutral case ($a_{down}/a = 0$) and the full span down case ($a_{down}/a = 0.865$, $Y_{flap}/a = 0.487$). The uncertainty in C_p is smaller than the symbol size.	56
3.4	Spanwise loading distributions for the neutral and full span down cases. The uncertainty in C_l is smaller than the symbol size.	57
3.5	Spanwise drag distributions for the neutral and full span down cases. The uncertainty in C_d is smaller than the symbol size.	58
3.6	Spanwise loading distributions for the neutral case and cases that divide the wing in two halves (a), and into three thirds (b). The uncertainty in C_l is less than or equal to the symbol size.	59
3.7	Spanwise loading distribution near the tip for cases that nearly conserve lift. The uncertainty bars shown on the neutral case apply to all cases at each spanwise location.	60
3.8	The tunnel coordinate system used to present wake data.	62
3.9	Contours of streamwise velocity and vorticity with tangential velocity vectors superimposed for the neutral case at $X/c = 0.20$	63
3.10	Contours of streamwise velocity and vorticity with tangential velocity vectors superimposed for the full span down case at $X/c = 0.20$	64

3.11	Contours of streamwise velocity and vorticity with tangential velocity vectors superimposed for $a_{down}/a = 0.13$, $Y_{flap}/a = 0.788$ at $X/c = 0.20$	66
3.12	Contours of streamwise velocity and vorticity with tangential velocity vectors superimposed for $a_{down}/a = 0.13$, $Y_{flap}/a = 0.788$ at $X/c = 0.83$	67
3.13	The velocity difference field for $a_{down}/a = 0.13$, $Y_{flap}/a = 0.788$	68
3.14	The velocity difference fields for $a_{down}/a = 0.13$, $Y_{flap}/a = 0.854$	70
3.15	Instantaneous velocity and vorticity fields for the neutral case at $X/c = 4.9$. Every other vector is removed for visual clarity.	71
3.16	Ensemble averaged velocity and vorticity fields for the neutral case at $X/c = 4.9$. Every other vector is removed for visual clarity.	71
3.17	Nondimensional velocity contours for the neutral and full span down cases.	72
3.18	Nondimensional velocity and vorticity profiles plotted in vortex centered coordinate system using center averaging technique for the neutral case (solid line) and the full span down case (dotted line). The uncertainty is indicated by the bar shown in the top left corner of each plot.	74
3.19	Nondimensional velocity profiles from five-hole probe measurements plotted in vortex centered coordinate system for neutral and full span down cases. The uncertainty is smaller than the symbol size.	75
3.20	Nondimensional velocity contours for small actuation ratio cases where $Y_{flap}/a = 0.654$ and 0.721	76
3.21	Nondimensional velocity contours for a small actuation ratio case where $Y_{flap}/a = 0.854$	77
3.22	Nondimensional velocity profiles from five-hole probe measurements plotted in vortex centered coordinate system for the neutral case and three cases where $a_{down}/a = 0.13$. The uncertainty is smaller than the symbol size.	78
3.23	Mean vortex center locations measured by PIV for large a_{down}/a . The vortex location at $X/c = 2.8$ for each configuration is denoted by a dashed circle around the symbol. The uncertainty in both directions is indicated by the symbol size of the neutral case.	79
3.24	Mean vortex center locations measured by PIV for cases where $a_{down}/a = 0.13$. The vortex location at $X/c = 2.8$ for each configuration is denoted by a dotted circle around the symbol. The uncertainty in both directions is indicated by the symbol size of the neutral case.	81

3.25	Mean vortex center locations for the two active wake alleviation schemes examined.	83
3.26	Transient response of the vortex center location for the simple MiTE actuation scheme where configuration 1 is the neutral case and configuration 2 is $(Y/a)_{flap} = 0.854$, $a_{down}/a = 0.13$. The uncertainty is smaller than the symbol size.	86
3.27	Transient response of the vortex center location to MiTE actuation schemes A and B.	87
4.1	Relationship between cut-off length and chosen domain size.	91
4.2	Parametric study on the influence of d_{cut}/b' and λ/b' upon T_{link}	91
4.3	Initial condition generated from transient response data for scheme A. . . .	94
4.4	A perspective view of the filaments for the model scale case at four points in time.	95
4.5	Snapshots in time of the filaments for the model scale case in the XY and XZ planes.	96
4.6	Diagram of the three vortex configurations examined.	99
4.7	The spanwise loading distributions required to generate the vortex configurations examined.	100
4.8	Snapshots of the filaments for the 2PCR-long case. The strong, outboard vortex pair (vortices 1 and 2) is shown in red.	102
4.9	Snapshots of the filaments for the 2PCR-long case in the XY plane. The strong, outboard vortex pair (vortices 1 and 2) is shown in black.	103
4.10	Snapshots of the filaments for the 2PCR-short case. The strong, outboard vortex pair (vortices 1 and 2) is shown in red.	104
4.11	Snapshots of the filaments for the 2PCR-short case in the XY plane. The strong, outboard vortex pair (vortices 1 and 2) is shown in black.	105
4.12	The time evolution (1-4) of the accelerated instability mechanism of Rennich and Lele. Figure reproduced from Rennich and Lele (1999).	106
4.13	Snapshots of the filaments for the 2PCTR case. The strong, outboard vortex pair (vortices 1 and 2) is shown in red.	108
4.14	Snapshots of the filaments for the 2PCTR case in the XY plane. The strong, outboard vortex pair (vortices 1 and 2) is shown in black.	109

4.15	The time evolution of the spanwise power spectrum at two wavelengths ($\lambda_1 \approx 9.36b_{12}$, $\lambda_2 \approx 12.07b_{34}$) for the 2PCTR case.	110
4.16	The time evolution of the nondimensional displacement measure of one out-board vortex for all cases.	110
5.1	Conceptual design of the spanwise actuating Gurney flap shown in two configurations.	113
5.2	A two-dimensional view of the assembled actuator in the XZ plane. . . .	114
5.3	An exploded Solidworks rendering of the wing and spanwise actuating Gurney flap.	115
5.4	A schematic of the solid flap with hole for the leadscrew and gap for nut. .	116
5.5	An exploded view of the housing, cover plate, and tip cap.	117
5.6	The wing and spanwise actuating Gurney flap assembled and mounted in the wind tunnel.	118
5.7	The root streamwise pressure profile for the wing equipped with spanwise actuating Gurney flap set to $Y_{flap}/a = 0.654$	119
5.8	Mean vortex center locations for different Y_{flap}/a values at $X/c = 4.66$. The uncertainty in both directions for all points is shown on one point.	120
A.1	A schematic of the calibration jet used for five-hole probe calibration. . . .	128
A.2	A schematic of the five-hole probe orientation and hole locations. Figure taken from Pauley (1988).	128
A.3	A picture of the five-hole probe mounted on the calibration jet.	129
A.4	An outline of the method used to process raw five-hole probe data to derive velocity measurements.	131
A.5	Calibration data for determining pitch angle.	132
A.6	Calibration data for determining yaw angle.	132
A.7	Calibration data for determining static pressure coefficient.	133
A.8	Calibration data for determining total pressure coefficient.	133
B.1	A schematic representation of the modeled geometry.	135
B.2	Contours of velocity magnitude in the XZ plane.	135
B.3	Streamwise velocity profile at the measurement plane.	136
B.4	Lift direction velocity profile at the measurement plane.	136

Nomenclature

Roman Symbols

A	Tangential flow parameter for calculating cut-off length (see Eq. 4.2).
a	Wing half-span.
a_{down}	Spanwise length of down MiTEs.
AR	Aspect ratio, $AR = 2a/c$.
b	Wing span.
b'	Spanwise vortex separation distance.
c	Chord length.
C	Streamwise flow parameter for calculating cut-off length (see Eq. 4.3).
C_{l_0}	Section lift coefficient at wing root.
$C_{p_{pitch}}$	Five-hole probe pitch pressure coefficient.
$C_{p_{static}}$	Five-hole probe static pressure coefficient.
$C_{p_{total}}$	Five-hole probe total pressure coefficient.
$C_{p_{yaw}}$	Five-hole probe yaw pressure coefficient.
C_a	Section axial force coefficient.
C_d	Section drag coefficient.
C_l	Section lift coefficient.
C_L	Total lift coefficient.
C_n	Section normal force coefficient.
C_p	Pressure coefficient.
CF	Calibration factor.
d_{cut}	Cut-off parameter for filament computations (see Eq. 4.1).
f'	Focal length.
G_{YY}	Power spectrum of spanwise vortex center location with respect to streamwise wavelength.
L	Lift.
L'	Lift per unit span.
L'_0	Lift per unit span at wing root.
p	Pressure.

p_S	Reference static pressure.
p_T	Reference total pressure.
r	Radial distance from vortex center.
Re	Reynolds number.
t^*	Nondimensional time based on flow timescale, $t^* = t/t_{flow}$.
t_{flow}	Flow timescale, $t_{flow} = c/U_\infty$.
T_{link}	Time to close approach of vortices.
U, V, W	Streamwise, spanwise, lift mean velocity components.
U_∞	Freestream velocity.
$U_{neutral}$	Streamwise velocity field when all MiTEs in the neutral position.
V_θ	Tangential velocity component.
$V1$	MiTE voltage.
$V2$	H-bridge voltage.
X, Y, Z	Streamwise, spanwise, lift directions (tunnel coordinate system).
X', Y', Z'	Streamwise, spanwise, lift directions (airfoil coordinate system).
$\Delta Y, \Delta Z$	Spanwise, lift directions (vortex centered coordinate system).
Y_{flap}	Geometric centroid of down MiTEs.

Subscripts

12	In two pair configurations, the outboard pair of vortices.
34	In two pair configurations, the inboard pair of vortices.
<i>drift</i>	Thermal drift of pressure transducer.
<i>ell</i>	Elliptical loading distribution.
<i>stat</i>	Statistical.
<i>trav</i>	Mechanical traverse.
<i>XDR</i>	Pressure transducer.

Greek

α	Angle of attack, or five-hole probe pitch angle.
----------	--

β	Five-hole probe yaw angle.
Γ	Circulation.
Γ_0	Circulation at wing root.
Δ	Uncertainty in quantity (unless otherwise specified).
δ_Δ	Maximum peak to peak displacement of the vortex center projected on the YZ plane.
λ	Streamwise perturbation wavelength.
ρ	Density.
σ	Standard deviation.
τ	Nondimensional time based on elliptical loading distribution, $\tau = (\Gamma_{ell}/(2\pi b'_{ell}))t$.
ω	Vorticity.

Abbreviations

1P	One pair vortex configuration.
2PCR	Two pair co-rotating vortex configuration.
2PCTR	Two pair counter-rotating vortex configuration.
CCD	Charge-coupled device.
CNC	Computer numerical control.
CW	Continuous wave.
DAQ	Data acquisition board.
DIO	Digital input/output.
DNS	Direct numerical simulation.
FAA	Federal Aviation Administration.
ICAO	International Civil Aviation Organization.
IFR	Instrument flight rules.
LES	Large Eddy Simulation.
MiTE	Miniature Trailing Edge Effector.
MOSFET	Metal-oxide-semiconductor field-effect transistor.
PIV	Particle image velocimetry.
PTFE	Polytetrafluoroethylene.
RANS	Reynolds averaged Navier-Stokes.
VFR	Visual flight rules.

Chapter 1

Introduction

1.1 The Wake Vortex Hazard

All bodies that generate lift must also generate circulation in the flow that they travel through. In the case of fixed wing aircraft, the circulation generated results in a sheet of vorticity immediately behind the aircraft whose rotationality is about the streamwise axis. Further into the wake, the vortex sheet typically rolls up into discrete trailing vortices that extend far behind the generating aircraft (See Fig. 1.1). For large aircraft, these vortices tend to be strong and persistent, thus, they can pose a serious threat to any smaller aircraft that may encounter them. This problem is referred to as the wake vortex hazard.

Before the major increase in commercial air travel that took place in and after the late 1960s, trailing vortices were generally regarded with little concern in terms of safety. The spacing between aircraft near airports was either left to the pilots or set at a constant 3 nautical miles (nm) depending on visibility conditions (Mack 1996; Chambers 2003). It was not until 1970 when the Federal Aviation Administration (FAA) implemented the first set of rules designed to prevent wake vortex encounters. The International Civil Aviation Organization (ICAO), adopted very similar rules at that time as well (Gerz et al. 2002). This was mostly a response to the introduction of the Boeing 747, the world's first jumbo jet. These first rules resulted mainly in a new classification system for aircraft (based on weight) and a new set of procedures for air traffic controllers and pilots which included mandatory spacing between aircraft operating near airports. Soon after the introduction of these spacing rules, it became clear that in the long term, airport capacity would be affected, and work began to try to solve this problem in the mid-1970s. Now that airport traffic has reached pre-9/11 volume with further increases predicted in the coming years, and with the pending introduction of another 400+ passenger aircraft, the problem has become much more urgent.

To illustrate the most fundamental aspects of this problem, we consider an aircraft with a simple loading distribution, where the section lift, L' , decreases from a maximum of L'_0 at the root of the aircraft to zero at the wing tips. Two counter-rotating vortices with strength

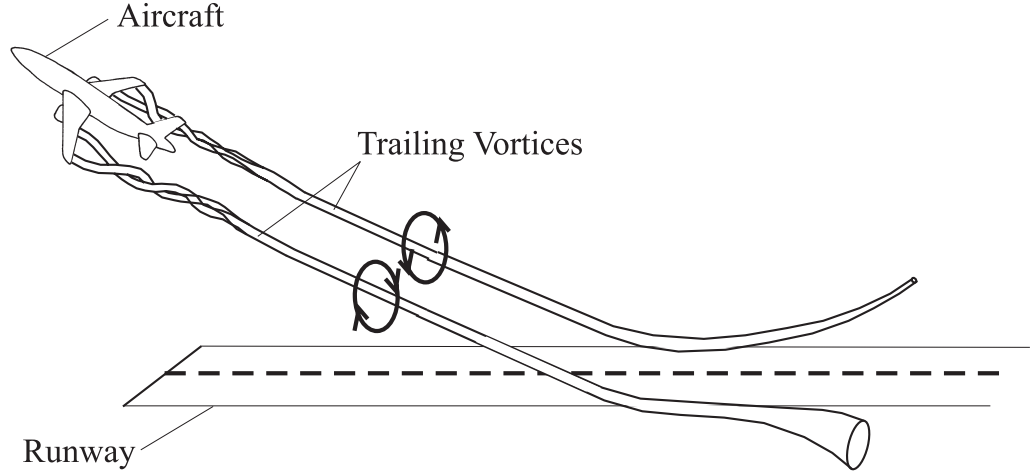


Fig. 1.1. Schematic depiction of trailing vortices near an airport.

$\pm\Gamma$ remain in the wake. The strength of the vortices is directly related to the weight and velocity of the aircraft by the equation

$$\Gamma = \frac{L'_0}{\rho U_\infty}, \quad (1.1)$$

where U_∞ is the velocity of the aircraft, and ρ is the density of the fluid. Thus, the vortex strength is linearly proportional to lift, and inversely proportional to aircraft velocity. To facilitate take-off and landing, it is generally desirable to minimize aircraft velocity while generating lift approximately equal to the weight of the aircraft. At take-off, the required lift is particularly large due to the amount of fuel being carried by the aircraft at that time. Thus, the aircraft requirements at take-off and landing serve to strengthen the vortices generated, and thus, magnify the problem.

The vortices created by the aircraft are counter-rotating, thus, in the absence of any other velocity field, they advect each other downward and slightly forward (depending on the angle of ascent). They move at a constant velocity $\Gamma/(2\pi b')$, where b' is the spanwise distance between the two vortices. Once they come close to the ground, they tend to move apart from each other horizontally. All of this is shown schematically in Fig. 1.1. The behavior outlined here can be dangerous to other aircraft entering or leaving the airspace for several reasons. First, trailing vortices can be extremely stable and have long lifespans. This is especially true on calm days with low atmospheric turbulence. Second, the rate of climb of most commercial aircraft shortly after take-off tends to be quite high. Rates of

4000 to 6000 feet per minute are not uncommon. Thus, after a short time, an aircraft may climb so high that its vortices will not have reached the ground before another aircraft takes off on a different flight path that intersects those vortices. Finally, crosswinds on runways are not uncommon and can easily cause one vortex that would otherwise roll away from the runway to linger on it.

The current technique for managing the wake vortex hazard is to enforce spacing rules at airports, which limit the minimum distance between consecutive aircraft taking off from and landing at their runways. The minimum distance required between two aircraft is mainly a function of visibility conditions and the relative sizes of the aircraft involved. For good visibility conditions, when visual flight rules (VFR) are in effect, the spacing between aircraft is the responsibility of the pilot of the following aircraft. For poor visibility, when instrument flight rules (IFR) are in effect, the spacing is the responsibility of the air traffic controller who must adhere to FAA rules.

These rules have evolved over the years in response to various concerns that have arisen. Most recently, in the early 1990s, several wake vortex encounters occurred at airports in the U.S. involving small airplanes landing behind Boeing 757 aircraft (Chambers 2003). Some of the incidents resulted in loss of life, while others caused the pilot to have to make drastic control surface deflections in order to land safely. As a result, in 1996, the FAA modified their spacing rules to account for this. The current matrix of required spacings is shown in Table 1.1. The size designations are based on maximum take-off weight. A “small” aircraft is less than 41,000 lbs, “large” is between 41,000 and 255,000 lbs, and “heavy” is greater than 255,000 lbs. The Boeing 757 based on weight would be either a heavy or large, however, if less than 255,000 lbs, it receives its own category as shown in Table 1.1. The -300 version would be a heavy while the -200 version receives its own category. This table gives the required spacing between aircraft operating on a single runway in IFR conditions. Other factors can make the rules even more prohibitive than this. If, for example, an airport in IFR conditions has two parallel runways that are less than 2500 feet apart laterally, the airport cannot treat those runways independently and is effectively reduced to one runway.

The spacing rules currently in place are essentially empirical, and based on worst case scenarios. It has been shown over time that with these rules in place, aircraft accidents directly due to wake vortex encounters are extremely improbable. It is largely agreed upon that the rules work because they are grossly conservative allowing far more distance than is really needed. This is supported by the fact that in VFR conditions, pilots tend to leave

Table 1.1. Spacing matrix given in nautical miles for IFR conditions on a single runway.

Leader	Follower		
	Small	Large	Heavy
Small	3	3	3
Large	4	3	3
B757	5	4	4
Heavy	6	5	4

far less space than the IFR rules would impose, and encounters are still rare (Mack 1996).

What actually happens to the wake vortices during the waiting period is unclear. Rennich (1997) argues that in this time, wake vortices have had so much time to descend by mutual induction that by the time another aircraft is present, the vortices are completely remote from any possible flight path. Spalart (1998) gives a detailed account of other arguments that have been made as to why the current spacing rules work. The “predictable decay” argument asserts that the spacing rules allow adequate time for the vortices to individually diffuse such that if a vortex encounter occurs, the effect on the follower would be mild. On the other hand, the “stochastic collapse” argument states that spacings are large enough to practically guarantee that some instability will destroy the vortices before the follower approaches. Spalart also mentions that no spacing rule was ever explicitly derived from either argument.

Finally, we note that the decay times implied by current spacing rules, conservative as they may be, can still be outlasted by wake vortices. Crouch et al. (2001) point out that there have been experiments and computations suggesting that vortices can remain coherent at distances larger than the current spacing rules would impose. Not surprisingly, it has been reported that at London-Heathrow airport, roughly 80 vortex encounters occur every year (Gerz et al. 2002). Most, however, probably occur in VFR conditions.

1.2 Previous Work

Aircraft spacing rules have become the major limiting factor on increasing airport traffic. Expanding airports to add more runways would be a legitimate solution, however, most large

airports are in major metropolitan areas where even if it were possible, expansion would be difficult and costly. Also, one major airport suffering delays is enough to send ripples through the entire system causing problems for many other airports. Thus, expansion would be necessary at several major airports in order to have an impact. Furthermore, strict noise regulations are in place at many airports. This makes expansion even more difficult in that new runways would have to be sufficiently far from residential areas. A better approach to the wake vortex hazard would be to find a way to increase the capacity of the airports and runways currently in use by reducing the required spacing between aircraft.

In the 1970s, many attempts at such a solution were made. A large amount of research was conducted, a variety of techniques was explored, and much fundamental knowledge about the problem was gained. Although some techniques showed promise, none emerged as a clear and practical solution. As time passed through the 1980s, and airport delays never reached the extreme levels that had been feared, the problem was largely forgotten. In the 1990s, when air traffic increases again became a growing concern, more attempts were made with more sophisticated experimental and computational techniques.

The strategies that have been explored can be divided into two main categories: detection and avoidance, and wake alleviation. With detection and avoidance, the basic idea is to know where the wake vortices are after take-off or landing, and to determine whether or not they pose a problem to following aircraft. The necessary spacing for the following aircraft can then be determined and implemented. This would occur for each take-off and landing. Since the present spacing rules are based on worst case scenarios, modified spacings based on the actual situation will very often reduce the necessary spacing and allow more aircraft to pass through an airport.

With passive and active wake alleviation strategies, the idea is to somehow render the wake of the generating aircraft safe within a short amount of time, thus, reducing the necessary spacing for worst case scenarios. We define passive strategies as ones that require no time-dependent forcing of any kind, and active strategies as ones that do.

This section is by no means a complete account of all of the work that has been done regarding the wake vortex hazard. The purpose of this section is to provide a summary of the efforts that have been made in the last 40 years, focusing on major progress that has been made and the positive and negative features of the strategies that have been studied.

1.2.1 Detection and Avoidance

For most take-offs and landings, shorter spacing could be used without incident, but there is no obvious way to determine when and where it is safe to do so. For detection and avoidance strategies, the aim is to survey the airspace near the airport to determine whether or not it is safe for another aircraft to take-off or land. The necessary spacing is determined for each aircraft that enters or leaves that airspace. Thus, no time is wasted waiting for wakes that are not there or are no longer a threat.

The main difficulty for these strategies is in constantly measuring a rather large airspace quickly and with reasonable accuracy. Measurement techniques for doing so have been researched and developed since the wake vortex hazard first became a problem. Laser doppler radar (lidar) was among the first techniques studied for making velocity measurements in large airspaces at long ranges. This technique relies upon optically measuring the velocity of aerosols in the flow field. Huffaker et al. (1970) discuss the theory and an early application of this technique. A continuous wave (CW) laser was used, and measurement ranges greater than 500 meters were achieved. Simulations were performed by Thomson and Meng (1976) to further study this technique as well as the complementary analytical techniques that would be necessary to apply it at an actual airport. Later, Hannon and Thomson (1994) experimented with pulsed lidar rather than CW. It was shown that although the finite pulse time limits the accuracy in velocity measurements, much greater ranges (> 2 km) could be achieved. Harris et al. (2002) and Keane et al. (2002) used a pulsed lidar system oriented in the axial direction to determine if such systems could be used for airborne vortex detection. They successfully measured the wakes of several large aircraft.

Another technique for making these measurements is radar-acoustic detection. This technique relies upon overlapping a radar and acoustic beam and measuring the resulting radar backscatter which occurs due to slight changes in the index of refraction of air caused by the acoustic beam (Rubin 2000). Rubin et al. (2000) demonstrated that a radar acoustic sounding system could be used to accurately detect and measure wake vortices of several commercial aircraft of different sizes. The results compared well to CW lidar measurements. In addition to these experiments, this technique has shown promise in numerical studies that have been done (Boluriaan and Morris 2001; Boluriaan and Morris 2002; Shariff and Wray 2002).

Finally, attempts have been made to integrate wake detection systems, real-time weather conditions, and vortex decay and transport predictions into a single system for dynamically

determining aircraft separation distances. The Aircraft Vortex Spacing System (AVOSS) developed by NASA is an example of such a system. This project is constantly evolving to incorporate new developments that occur in each contributing discipline. A thorough description of the system is given in Hinton (1996).

The main problems with the detection and avoidance strategies that have been explored are that they are costly, and not yet reliable enough to be implemented. Furthermore, even if detection and avoidance techniques could be made completely effective, on calm days, when dangerous vortices tend to linger in the airspace, the system would be of no help in preventing delays. Wake alleviation techniques address the problem more directly.

1.2.2 Passive Wake Alleviation

Passive wake alleviation strategies rely upon modifying the vortex wake of the generating aircraft in a steady fashion with no time-dependent forcing. The idea is to either modify the vortex rollup process such that the resultant wake is too weak or diffuse to be of danger to following aircraft, or to passively excite some instability that will lead to rapid diffusion of vorticity.

Much of the early research into solving the wake vortex hazard passively involved altering the vortex rollup process in the near wake by changing the planform shape, thus, modifying the loading distribution. Rossow (1975, 1977) performed theoretical studies using 2D inviscid computations in search of loading distributions that would create wakes that would either not roll up, or would have very diffuse vorticity fields. Loading distributions where the section lift coefficient decreases linearly from root to tip as well as jagged loading distributions with large, abrupt variations in section lift were examined. It was found that both of these types of loading distributions tended to produce wakes with a more diffuse vorticity field. Attempts at optimizing the distribution shape were made. The wakes produced by the optimal distribution displayed notable decreases in the induced rolling moment that would be experienced by a following aircraft when compared to typical loading distributions. Holbrook et al. (1985) performed experiments with a variable twist wing that found the same general results. Corsiglia and Dunham Jr. (1976) performed a variety of experiments, including flight tests, and showed that the standard landing configuration of a Boeing 747 could be slightly modified to move more of the lift inboard and produce a less hazardous wake. More recently, Graham et al. (2003) performed experiments that showed that a more diffuse wake could be achieved by a notched loading distribution that

creates discrete vortices that tend not to merge.

In addition to simply modifying the planform shape, numerous static devices that could be added on to existing planforms have been studied. Lezius (1975) examined the decay of trailing vortices from a wing with and without a triangular leading edge extension at the wing tip. Flow visualizations performed in a water tow tank seemed to show that the modified wing tip produced a much more diffuse wake than the clean wing, but no quantitative measurements were made. Patterson (1975) experimented with splines mounted directly downstream of the wing tip such that their bluff shape would interfere directly with the tip vortex. They were found to be effective in increasing core size, but they also created a large drag penalty. Other splines as well as various wing tip shapes were revisited in experiments by Traub et al. (1998) who noted similar results. Croom (1977) examined the use of spoilers on the suction side of wings typically used as air brakes on commercial aircraft. Wind tunnel and flight tests were performed. Again, significant increases in the vortex core size were achieved.

A large amount of work has gone into the idea of using fins mounted on the suction or pressure side of wings in order to modify the loading distribution and/or add another discrete vortex to the wake that might interact with the tip vortex in a beneficial way. Rossow (1978) performed wind tunnel tests and attempted to determine an optimal placing and orientation for a fin. It was found that a fin on the suction side of the wing creating a vortex that is counter-rotating with respect to the tip vortex tended to produce the most benign wake. Later, Schell et al. (2000), Özger et al. (2001), Heyes and Smith (2005), and Schöll et al. (2006) experimented with various fin designs on both research planforms as well as realistic aircraft wing shapes. Again, it was shown that more diffuse wakes could be achieved.

The idea of blowing air jets near the wing tips was examined by Patterson (1975) and Tanaka et al. (1978), then later by Simpson et al. (2002) and Zhou and Zhang (2004). Significant increases in vortex core size (factors of 5 in some cases) were achieved in the experiments conducted.

Most recently, other passive techniques have been researched wherein the goal was to use a passive device to excite some natural instability in the trailing vortex system. Ortega et al. (2002) and Ortega et al. (2003) performed tow tank experiments with a rectangular wing equipped with triangular flaps at the tips that extend the trailing edge as shown in Fig. 1.2. These flaps create a pair of inboard flap vortices that are counter-rotating with respect

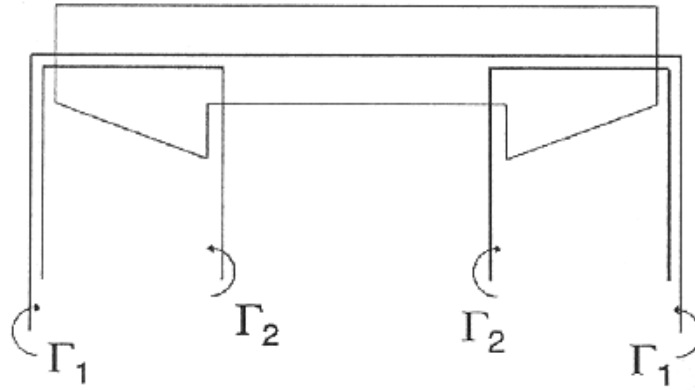


Fig. 1.2. The triangular flap wing used by Ortega et al. Figure reproduced from Ortega et al. (2003).

to the tip vortices. Various flap sizes were examined such that the strength of the inboard vortices ranged from -40% to -70% of the outboard vortex strength. It was shown that the trailing vortex system created by the flapped wing undergoes a rapidly growing instability wherein each flap vortex becomes entangled with its outboard counterpart in a periodic fashion. This dramatic process is shown in the flow visualizations of Fig. 1.3. The vorticity is rendered far less coherent as the instability grows rapidly. Stumpf (2004) demonstrated this same mechanism numerically using RANS and LES to model the wake of a real aircraft. Durston et al. (2005) used tail wings as shown in Fig. 1.4, rather than triangular flaps, to produce the same instability with equal success. Haverkamp et al. (2003) also followed the work of Ortega et al. using triangular flaps to passively excite the same vortex instability.

The main advantage to using passive techniques is the simplicity associated with them. The absence of time-dependent forcing allows most of the proposed devices to be easy to construct. Many of these techniques, however, come with significant drag and lift penalties as well as additional fatigue on the planform. Drag and lift penalties could, perhaps, be overcome by having the device present in the flow only when needed and stowed when it is not. However, this would likely add great complexity and weight to the aircraft.

The problem common to all of the above mentioned techniques is that in general, if the same amount of lift is produced, the same amount of circulation tends to be present in the wake regardless of how it is distributed. Thus, the hazard for the follower may remain. As Spalart (1998) points out, an increase in vortex core diameter from 0.5 m to 1 m is little help to a following aircraft with a span of 30 m. Furthermore, it is widely accepted that

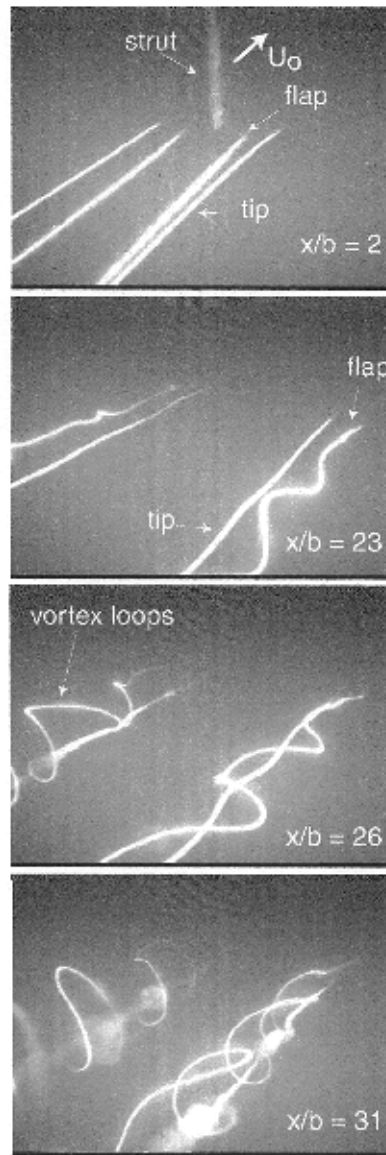


Fig. 1.3. The passively excited instability examined by Ortega et al. Figure reproduced from Ortega et al. (2003).

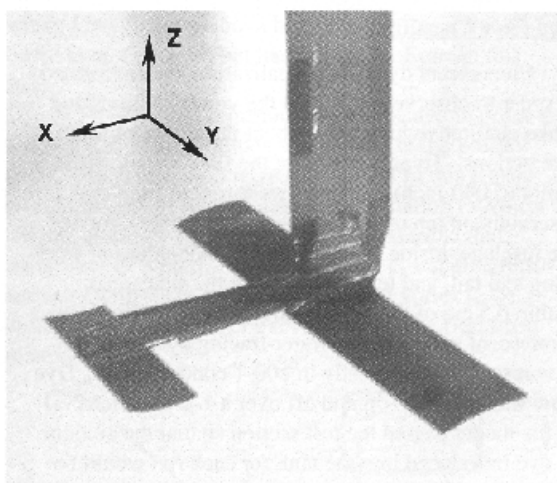


Fig. 1.4. The apparatus used by Durston et al. Figure reproduced from Durston et al. (2003).

a system of trailing vortices whose vorticity is more diffuse tends to be less susceptible to instability than a strong, tightly rolled-up vortex. If the stochastic collapse model discussed earlier is the more accurate description of how trailing vortices ultimately disappear, then these passive techniques may, in fact, increase vortex longevity and aggravate the problem. It is for these reasons that none of the techniques discussed above have emerged as a clear and practical aerodynamic solution to the wake vortex hazard.

1.2.3 Active Wake Alleviation

Active wake alleviation strategies rely upon some time-dependent forcing to perturb the wake of an aircraft and excite natural instabilities. The instability should then lead to the rapid destruction or attenuation of the vortex system.

Crow (1970) was the first to analyze the stability of two counter-rotating vortices. His analysis modeled the system as inviscid line vortices in three dimensions. The velocities were found by integrating the Biot-Savart law, and the singularity at the vortex center was removed by truncating the integral at a specific cut-off distance. His analysis revealed the existence of an inviscid, long wavelength sinusoidal instability whose amplitude grows exponentially in time and would likely lead to periodic linking of the vortex pair to produce a series of vortex rings. This confirmed what had often been observed on clear days in the

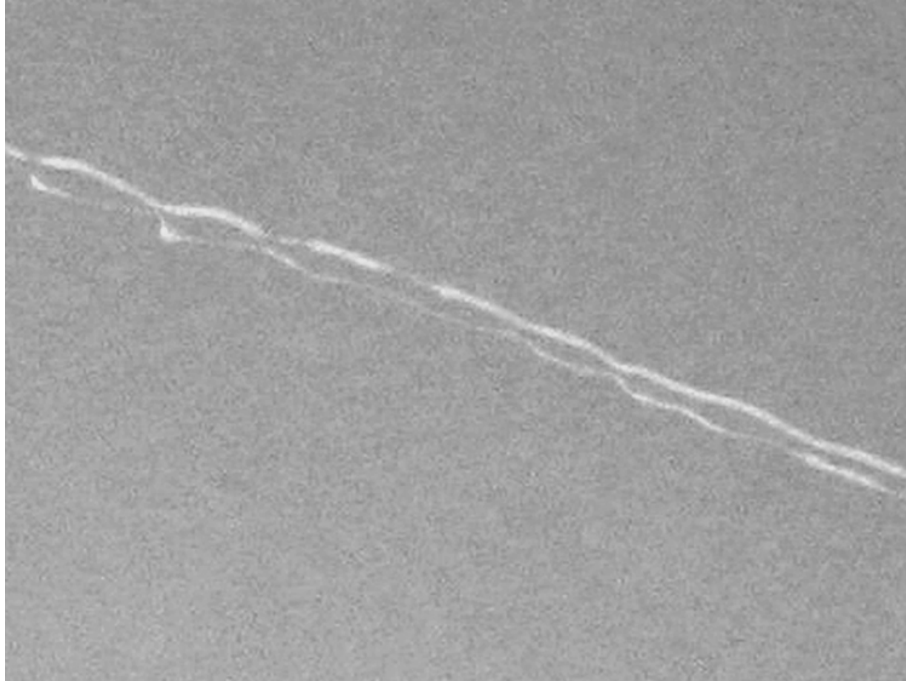


Fig. 1.5. Late stages of the Crow instability.

contrails left by large aircraft (Fig. 1.5). Atmospheric turbulence was cited as the typical method by which this instability is excited. Chevalier (1973) later performed flight tests that demonstrated how elevator oscillations could be used to excite the Crow instability. Later, Crow and Bate Jr. (1976) incorporated the effects of atmospheric turbulence in the development of a new model for wake lifespan. They concluded that atmospheric turbulence levels would often be unable to excite Crow instability within a short enough time to change spacing rules. This would later be confirmed by the DNS computations of Spalart and Wray (1996). Crow and Bate then proposed a simple active scheme for exciting the Crow instability while maintaining constant lift. The idea was to periodically oscillate the inboard and outboard flaps of an aircraft such that a significant fraction of the lift moves inboard and outboard while the total lift of the aircraft is held constant.

Working with a more fundamental configuration, Bilanin and Widnall (1973) conducted tow tank experiments on a full span NACA 0012 wing equipped with conventional inboard and outboard flaps, each a quarter-span in length. Periodic flap oscillations were used to move a large fraction of the lift inboard and outboard while keeping lift constant to $\pm 2\%$. They showed that this kind of forcing could indeed be used to excite Crow instability

and bring about rapid destruction of the vortex pair. The strong forcing used in this work affected both the strength and core size of the vortices. Flow visualizations indicated that at late stages in the instability, vortex breakdown would occur slightly upstream of the points of maximum separation between vortices. This was viewed as fortuitous in that even the coherence of the resultant vortex rings would be attenuated. Their work demonstrated the feasibility of using loading distribution oscillations to excite Crow instability, but they also confirmed that the core size and strength of the vortices do have an effect on the evolution of the instability. Later, Widnall (1975), in a thorough review of the vortex filament work done up to that point, analytically described the influence that core size and axial velocities have upon the kinematics of the vortex filaments. They also showed that the cut-off distance parameter used by Crow (1970) can be modified to account for these effects.

Barber and Tymczyszyn (1980) conducted flight tests with large commercial aircraft wherein lateral-control oscillations in time were made in order to excite Crow instability. Although the spoiler deflections were too large to be feasible during take-off or landing, they demonstrated that Crow instability could be excited in this fashion and completely destroy the wake within three nautical miles of the generating aircraft. The tow tank experiments of Jordan (1983) further supported this conclusion.

Rossow (1986, 1987) considered the use of roll oscillations of the aircraft as a means for exciting Crow instability. Using vortex filament computations, he showed that this was possible. Although this could be achieved while maintaining constant lift, the negative impact upon passenger comfort associated with roll oscillations is the main problem with such a strategy.

Rennich and Lele (1997, 1999) carefully studied the evolution of the Crow instability using both vortex filament and high accuracy Navier-Stokes computations. They confirmed the validity of Crow's analysis and showed that the Crow instability could be excited by perturbations of the loading distribution similar to what Crow and Bate had suggested. Rennich and Lele also examined wakes consisting of four vortices with the inboard pair counter-rotating with respect to the outboard pair (see Fig. 1.6). They perturbed the shape of the loading distribution of the model in time with a very small sinusoidal oscillation that conserved total lift. They discovered a rapidly growing instability mechanism with growth rates seven times greater than that of pure Crow instability. Computations were carried out through the linking process, and significant reductions in the lifespan of the wake were shown. The evolution of this instability mechanism, however, was highly sensitive to

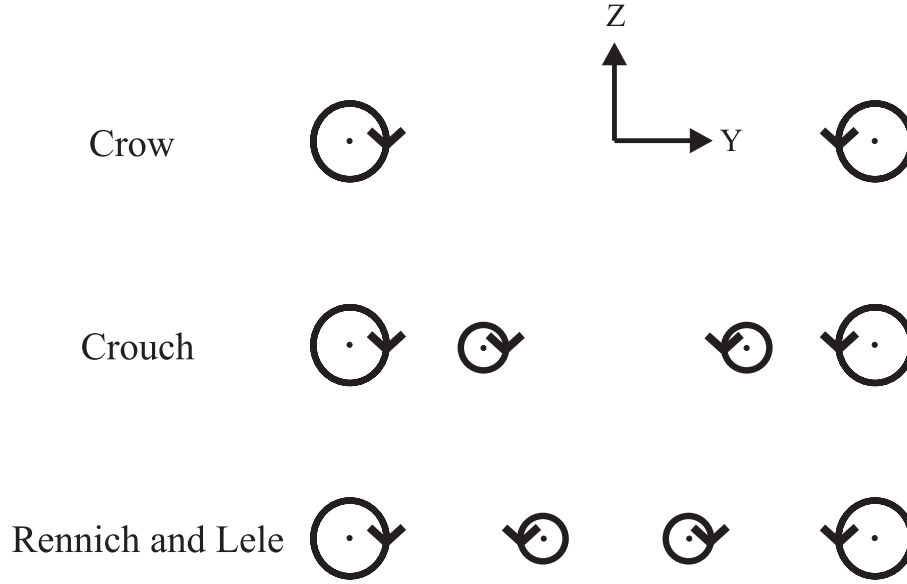


Fig. 1.6. Two-dimensional cut of the line vortex systems previously examined.

the spacing of the vortices, and the loading distribution required to produce the necessary vortex configuration would be difficult to achieve. Nonetheless, they showed that even small perturbations in vortex location ($<10\%$ span) could be used to excite vortex instability. This remains the most rapidly growing mechanism known that can bring about the destruction of a four vortex system.

Extending the stability analysis of Crow to a four vortex system with the inboard vortices co-rotating with respect to the outboard vortices (see Fig. 1.6), Crouch (1997) showed that such a system is subject to three modes of instability, all with notably higher growth rates than pure Crow instability. Crouch et al. (2001) later performed DNS and tow tank experiments on representative commercial aircraft vortex configurations. They demonstrated that the long streamwise wavelength mode previously analyzed could be excited with periodic oscillations of the conventional inboard and outboard flaps while holding lift nearly constant. Significant decreases in linking time were achieved. They also demonstrated the capability of exciting pure Crow instability on a two vortex configuration, but the amount of forcing required was significantly greater. In all cases, the additional mechanical requirements and fatigue on the conventional flaps in producing such a perturbation were likely the greatest problems with this strategy.

Fabre and Jacquin (2000) examined the four vortex system studied by Rennich and Lele

with vortex filament computations and stability analysis. They found that in addition to the accelerated instability shown by Rennich and Lele, there exists an even faster growing instability mode which corresponds essentially to a pure Crow instability on the inboard pair. This mode by itself, however, would not lead to linking of the strong outboard vortices. Fabre et al. (2002) then performed a wider parametric study of the same four vortex configuration. Again using vortex filament computations and stability analysis, they confirmed that the fastest growing instability mode on that configuration capable of bringing about linking of the strong outboard vortex pair was the mechanism shown by Rennich and Lele.

Rebours et al. (2004) experimentally examined the excitation of Crow instability in a water tunnel on vortices created by vortex generators and perturbed them using an oscillating strip downstream of the generators. They used a novel technique to acquire data on the development of Crow instability, and also examined the sensitivity of the instability to the excitation frequency.

Heyes and Smith (2004) and Bearman et al. (2006) were able to excite Crow instability in wind tunnel experiments using pulsed spanwise blowing of a jet sheet from the wing tips. It was shown that the vortex would respond to a varying range of pulsing frequencies but as the frequency was increased, the amplitude of the response became smaller. Static vortex displacements from the nominal position as large as 12% chord in the spanwise direction were achieved, however, this required rather high blowing rates, and no evaluation of the aerodynamic effects upon the wing were performed. It is likely that total lift was not conserved.

Building upon their passive instability work, Haverkamp et al. (2005) performed tow tank experiments where inboard and outboard flaps were periodically oscillated, similar to the experiments of Bilanin and Widnall (1973). Significant reduction in the trailing vortex lifespan was observed.

Considering the various instabilities that trailing vortices are subject to, Greenblatt et al. (2005) studied the use of synthetic jet actuators at the trailing edge of a flapped NACA 0015 wing as a means of controlling flow separation on the wing and, thus, perturbing the trailing vortex. They showed that if used in a specific way, these actuators could perturb the trailing vortex by as much as 3.1% chord in the spanwise direction, and that the perturbations could be achieved at reasonably high frequencies. This was done while holding the lift constant. The mechanism responsible for perturbing the vortex, however,

was dependent on streamwise separation of the flow about the flap. This could easily limit the applicability of this technique since flow separation can be unpredictable, and is not a desirable attribute for real airfoils.

Finally, an exploratory computational study was done by Orlandi et al. (1998, 2001) wherein the possibility of exciting vortex instability through thermal perturbations was considered. The vortices would need to be periodically heated by either redirecting jet engine exhaust, or by auxiliary burners mounted on the wings. A DNS study showed potential for such a technique despite the difficult practical issues.

1.2.4 Other Vortex Instability Work

The wake vortex hazard has motivated a great amount of fundamental research on vortex instability wherein only the dynamics of the vortex system is considered, and no attempt to aerodynamically apply the mechanism is made. Various instabilities involving vortex rings, single line vortices, co-rotating and counter-rotating vortex pairs, and multiple vortex pairs have been examined. We briefly discuss here some of the important findings that show promise with regard to wake alleviation.

Much of the passive alleviation work described above is encouraged by the large amount of fundamental research that has shown how a single vortex is susceptible to various instabilities. The experiments of Singh and Uberoi (1976) showed the existence of a sinusoidal instability of a single laminar vortex with a wavelength on the order of the vortex core diameter (much shorter than Crow instability). This instability leads to a large increase in core diameter and the onset of turbulent fluctuations. Khorrami (1991) would later analytically demonstrate the existence of this instability and show that it was caused by viscosity. Viscosity had been viewed previously as a stabilizing factor.

Examining a pair of counter-rotating vortices, Thomas and Auerbach (1994) were the first to show the simultaneous development of both long and short-wave instabilities on a vortex pair. They showed that neither instability would develop with only one vortex present, thus, the two distinct modes were cooperative. Leweke and Williamson (1998) went on to carefully examine the cooperative instability in detail, and show how the short-wave instability becomes more important after the Crow instability has reduced the vortex pair to an array of vortex rings. Laporte and Corjon (2000) later reproduced these experimental results numerically using DNS. Note that the vortices examined by these researchers are laminar, and thus, not very representative of aircraft trailing vortices. However, Fabre and

Jacquín (2004) would later demonstrate the existence of short-wave cooperative instabilities on different types of vortices that are more representative of aircraft wake vortices.

Finally, we note that the main reason that long wavelength instabilities are generally preferred for wake alleviation techniques is that no short wavelength instability has ever demonstrated the ability to bring together counter-rotating vortices of opposite sign. However, short wavelength instabilities can be useful if the goal is merely to diffuse coherent vortices, or to destroy the vortex rings that form in the late stages of long wavelength instabilities.

1.3 Miniature Trailing Edge Effectors

The main difficulty in achieving an active wake alleviation strategy is in finding an appropriate way to perturb the trailing vortices. A practically applicable scheme must perturb them in time at an appropriate frequency without significantly changing the total lift experienced by the wing. Miniature Trailing Edge Effectors (MiTEs) seem well suited for this.

A Gurney flap is a small tab ($\approx 1\text{-}2\%c$) placed at the trailing edge of an airfoil oriented perpendicular to the flow (see Fig. 1.7). Solovitz (2002) provides a comprehensive review of previous research on Gurney flaps. It has been shown that Gurney flaps are capable of significantly increasing the section lift coefficient of an airfoil ($> 10\%$) without incurring a large increase in drag. They do this by effectively changing the airfoil camber thereby increasing the circulation about it. Since Gurney flaps are small, they accomplish this while remaining inside the airfoil boundary layer.

Gurney flaps can run along the entire span of an airfoil, or they can be segmented and placed along only certain spanwise portions. Miniature Trailing Edge Effectors (MiTEs) are spanwise segmented Gurney flaps placed at discrete spanwise locations. They can be applied in arrays along the span, individually controlled, and rapidly actuated.

Solovitz and Eaton (2004a, 2004b) performed a comprehensive study on the aerodynamic effects of an array of MiTEs on the trailing edge of a full span model airfoil. They performed wind tunnel tests on a MESO5 airfoil that spanned the entire wind tunnel test section. The model was two-dimensional in the sense that the shape of the clean airfoil was constant along the entire span, however, the airfoil was equipped with an array of individually controlled MiTEs along the span, thus, allowing spanwise variation in MiTE configuration.

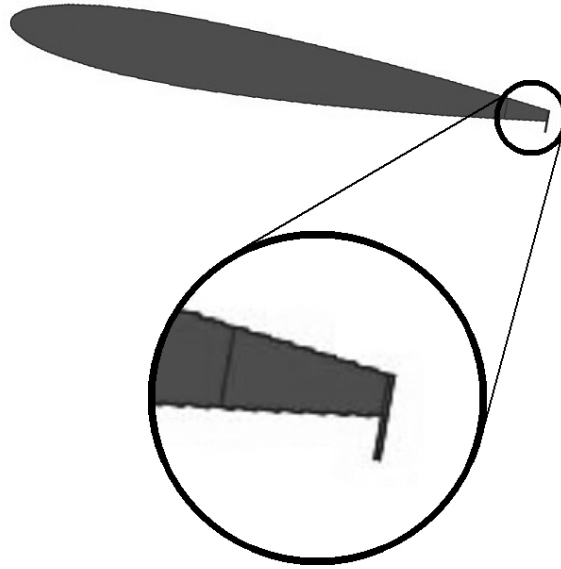


Fig. 1.7. A Gurney flap on a NACA 0012 airfoil with a blunt trailing edge.

The spanwise influence of MiTEs upon the section lift coefficient and steady flow structure in the wake was examined. They showed that when applied in large groups, a single additional MiTE could have a large spanwise influence, but a single MiTE or small group of MiTEs operating independently did not. When applied individually, a single MiTE still had a strong effect upon the section lift coefficient at its particular spanwise location, but this influence was limited to roughly one MiTE span away in either spanwise direction. This was shown with both pressure profile measurements and particle image velocimetry (PIV) of the flow field immediately downstream of the trailing edge. This result demonstrated the ability that MiTEs have to control the shape of the spanwise loading distribution of a wing.

The dynamic response of the flow to MiTE actuation was also examined. Time accurate measurements of the flow field immediately downstream of the airfoil trailing edge were made using dynamic PIV. The results showed that when the MiTE actuation time was slow compared to the timescales of the flow, the response of the flow tended to be quasi-steady. For this case, in the amount of time taken for the flap to move from one position to another, several vortices were shed from the flap. If, however, the MiTE actuation time was fast compared to the flow timescales, different behavior was seen. The vortex shedding became phase-locked with the motion of the flap, and a significant overshoot in MiTE effectiveness

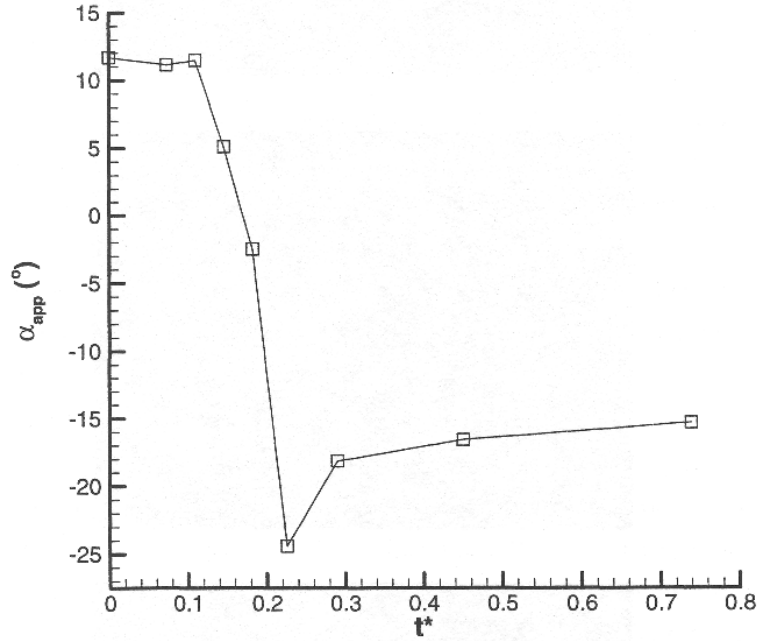


Fig. 1.8. Unsteady behavior associated with rapid flap actuation shown by Solovitz and Eaton. Figure reproduced from Solovitz (2004).

was noted. Fig. 1.8 plots the average downwash angle in the wake of the flap as a function of time while the flap moves from the up to the down position. The average flow angle is a qualitative measure of the lift produced (more negative implies more lift). Clearly, as the flap moves to the down position, an overshoot in lift occurs before approaching a steady-state value. This demonstrates additional potential that MiTEs can have if actuated rapidly.

As discussed before, an effective way of perturbing a wing tip vortex is to alter the shape of the spanwise loading distribution. The specific way in which this is achieved, however, has direct consequences on the perturbation imparted to the vortex. The known characteristics of MiTEs discussed above suggest that they can be used to significantly alter the spanwise loading distribution of a wing in time while maintaining constant lift. The effect MiTEs can have upon the trailing vortex and the subsequent evolution of vortex instabilities is the subject of this work.

1.4 Objectives

The overall objective of this work is to assess the potential that MiTEs have for active wake alleviation. An experimental study is performed using a model wing with an array of MiTEs placed in a wind tunnel. The main objective of the experimental work is to measure the effects that MiTEs can have upon a wing and its trailing vortex. Pressure measurements on the wing are performed to determine the effect upon the spanwise loading distribution. A near wake study using a five-hole probe is conducted to examine the nature and development of the perturbation imparted to the vortex. Finally, steady and dynamic PIV measurements are performed in the intermediate wake in order to quantify the steady and time-dependent effect of MiTEs upon the trailing vortex.

The experimental results are used to form a complete initial condition for a vortex filament computation. The main objective of the computational study is to examine how different vortex configurations with embedded MiTE perturbations might evolve after long amounts of time. The model scale configuration and several full scale configurations are examined.

Chapter 2

Experimental Apparatus and Methods

2.1 Experimental Model and Facilities

2.1.1 Half-Span Wing

The half-span model used in this work consisted of a wing with an untapered NACA 0012 profile, chord length $c = 300$ mm, half-span $a = 619$ mm, and overall aspect ratio $AR = 2a/c = 4.1$. The half-span was measured from the root to the furthest spanwise point on the tip. For describing the geometry, we use an airfoil coordinate system denoted by prime symbols and shown in Fig. 2.1. The origin is at the leading edge of the airfoil and the X' axis runs along the chord line. The coordinates for the upper half of the airfoil shape are given in Table 2.1. We designed the shape by starting with a standard NACA 0012 geometry with a chord length of 319.2 mm. Next, we truncated the airfoil shape at 300 mm downstream of the leading edge, disregarding the final 19.2 mm and creating a blunt trailing edge of thickness $0.02c$. The tip of the wing was rounded with a semi-circle with radius of curvature varying according to the local thickness of the wing.

Since the test conditions were at lower Reynolds number than actual flight conditions, a boundary layer trip consisting of embossed V's on Dymo tape was placed at $X'/c = 0.4$ in order to ensure uniform transition to turbulence. The trip extended across the entire span on both the pressure and suction sides, and was 9.4 mm wide in the streamwise direction. The embossed V's protruded into the flow roughly 0.6 mm from the surface of the wing.

The wing was fabricated in two halves by CNC machining of Modulan 750, a polyurethane based material with excellent machinability and dimensional stability. We began with a piece of rectangular stock machined to a thickness just over half of the maximum wing thickness. A ball endmill was used to take long spanwise cuts through the block. First, the inside surface was machined, then the piece was inverted and the outside surface was machined. This was done for each half.

Two threaded rods of $3/4''$ and $1/2''$ diameter oriented along the Y' axis and protruding from the root were used to mount the wing in the tunnel and control the angle of attack.

Table 2.1. Airfoil coordinates.

X'/c	$(Z'/c)_{up}$	X'/c	$(Z'/c)_{up}$	X'/c	$(Z'/c)_{up}$
0.000000	0.000000	0.238580	0.062308	0.770078	0.036477
0.000038	0.001079	0.257544	0.062977	0.790059	0.034441
0.000343	0.003255	0.276628	0.063449	0.810036	0.032358
0.000951	0.005485	0.295818	0.063735	0.829988	0.030232
0.001891	0.007786	0.315103	0.063848	0.849917	0.028053
0.003199	0.010154	0.334475	0.063801	0.869854	0.025818
0.004917	0.012552	0.353926	0.063603	0.889807	0.023534
0.007079	0.014957	0.373441	0.063266	0.909735	0.021206
0.009700	0.017360	0.392999	0.062799	0.923333	0.019600
0.012780	0.019767	0.412595	0.062206	1.000000	0.010000
0.016354	0.022206	0.432227	0.061493		
0.020545	0.024702	0.451909	0.060666		
0.025516	0.027294	0.471643	0.059735		
0.031458	0.030023	0.491420	0.058708		
0.038573	0.032890	0.511223	0.057589		
0.047039	0.035874	0.531044	0.056386		
0.057022	0.038954	0.550883	0.055099		
0.068669	0.042078	0.570744	0.053734		
0.081967	0.045164	0.590626	0.052293		
0.096718	0.048113	0.610526	0.050781		
0.112596	0.050841	0.630441	0.049203		
0.129323	0.053303	0.650367	0.047560		
0.146670	0.055473	0.670303	0.045855		
0.164485	0.057357	0.690249	0.044091		
0.182658	0.058966	0.710200	0.042269		
0.201101	0.060318	0.730152	0.040392		
0.219756	0.061426	0.750109	0.038461		

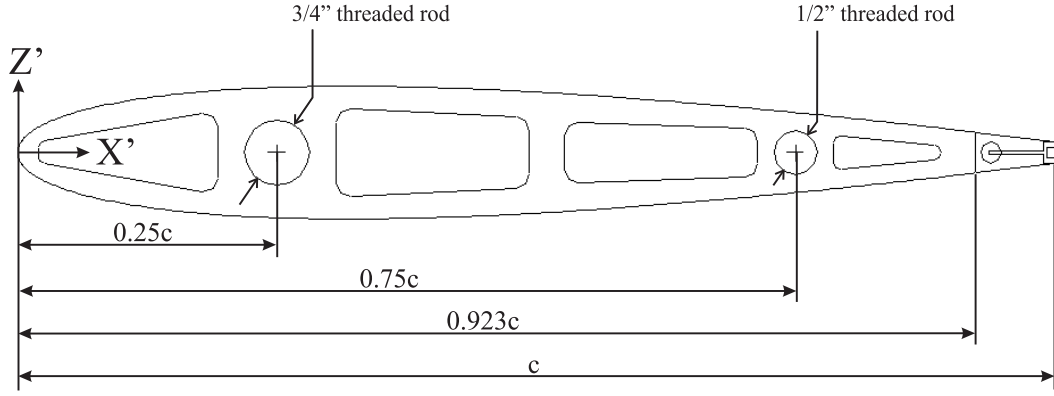


Fig. 2.1. Schematic of the airfoil cross-section.

As illustrated in Fig. 2.1, the inside of the wing had two round channels at $X'/c = 0.25$ and 0.75 for housing these rods. A square nut was embedded inside the wing in the channel at $X'/c = 0.25$ such that this rod could be secured in the wing. The smaller rod at $X'/c = 0.75$ was secured in a hole that was tapped on the inside of the wing tip. Several additional channels were machined on the inside of the wing to create room for tubing and wiring to pass through the wing.

We equipped the wing with 217 0.64 mm diameter pressure taps for measuring the span-wise loading distribution. Each pressure tap was machined into the wing in the following way. A hole of 0.82 mm diameter was drilled perpendicular to the outside surface of the wing at the desired location. A short metal hypodermic tube with 0.82 mm OD and 0.64 mm ID was then tightly fit into the hole. We inserted the tubing such that it protruded very slightly (< 0.5 mm) from the outside surface of the wing. It was secured on the inner surface using epoxy. On the inside of the wing, we connected the metal tubing to $1/32''$ ID Tygon tubing that exited the wing through the root. More epoxy was then applied to ensure a proper seal. Finally, we used a fine metal file to remove the slight protrusions of metal tubing on the outside surface of the wing without removing any Modulan.

To assemble the wing, the two halves were connected to each other using steel nuts and bolts at six locations about the planform. The holes in the wing for these connectors were recessed such that there was no protrusion into the flow. With the bolts inserted and tightened, we carefully filled the recesses with modeling clay such that the shape of the

wing was preserved. The wing tip was machined separately of the same material as the wing and attached to the wing using steel bolts screwed into threaded inserts embedded in the wing. The holes in the wing tip were also recessed and filled. After assembly, the wing was sanded smooth using a rigid sanding block except at the tip where loose sand paper was used. After final assembly, an examination of the wing dimensions at various locations showed that the maximum difference between the design and actual shape was no more than 1.5 mm in any direction.

We mounted the wing along the centerline of the wind tunnel through the removable window furthest upstream in the tunnel test section. Slots were machined into the window by CNC milling allowing us to vary the angle of attack from -8.9° to $+8.9^\circ$. The wing would pivot about the large threaded rod at the quarter chord, and the angle of attack was measured using tick marks placed at one degree intervals engraved in the window by CNC. Air flow through the large slots in the window was prevented by a 2.1 mm thick acrylic plate mounted at the root of the wing seated against the bottom wall inside the tunnel. The plate was sufficiently thin and far from all measurement locations such that its effect was negligible. Figure 2.2 shows a picture of the assembled wing mounted in the wind tunnel.

2.1.2 MiTEs

The MiTEs used by Solovitz (2002) were successful in their intended purpose, but several design problems limited their capabilities. The details of their design and aerodynamic performance are given in Park (2002) and Solovitz (2002) respectively. As shown in Fig. 2.3, the old MiTEs had flaps that could slide up and down in the lift direction along the trailing edge of the MiTE body. A motor in the MiTE body turned a pinion connected to a rack that was fixed to the flap. The main problem with this design was the large number of moving parts. This could result in low reliability, inconsistent actuation between MiTEs, and short lifespan.

We designed and constructed a new generation of MiTEs for this work which was completely different and overcame these problems. The basic concept for the new design was first suggested by Dr. Stefan Bieniawski. A schematic representation is shown in Fig. 2.4. Each MiTE had two possible states, “neutral” and “down”. Like the older design, the flap sat immediately behind the blunt trailing edge in the neutral position. In the down position, the flap extended $0.015c$ perpendicular to the flow on the pressure side of the wing. The flap was moved by a pivot arm that extended directly from the flap to the shaft of a

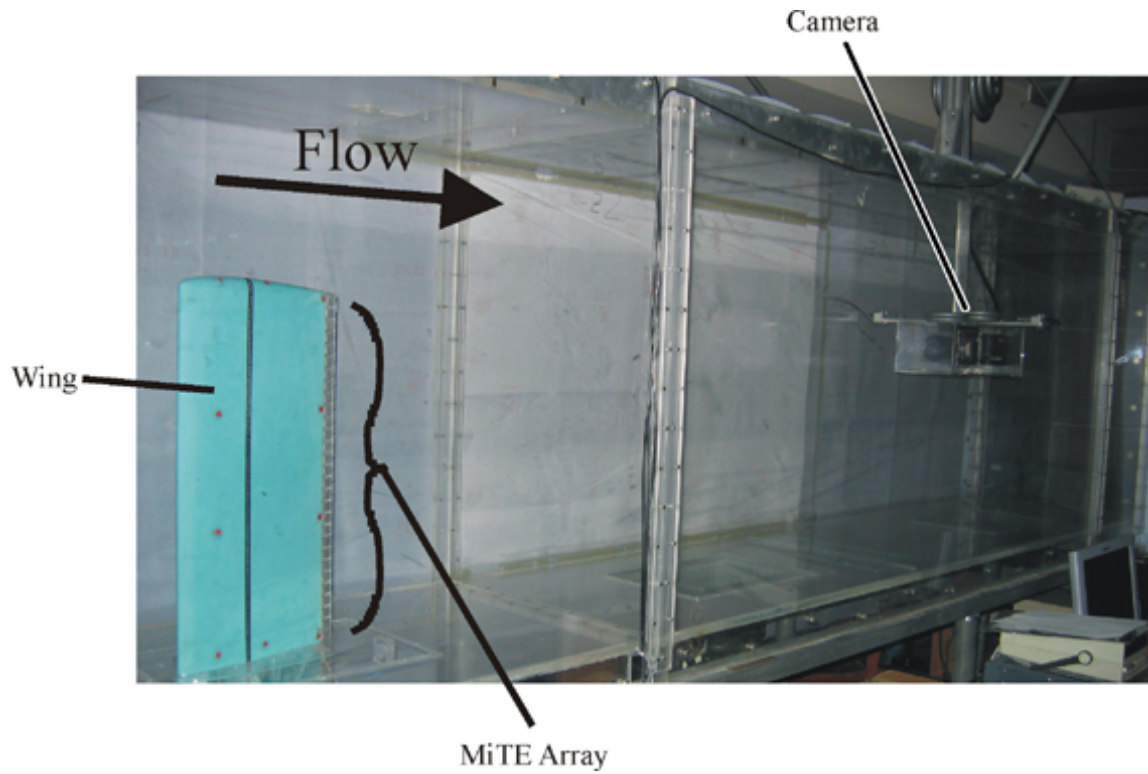


Fig. 2.2. The wing and MiTEs mounted in the wind tunnel test section.

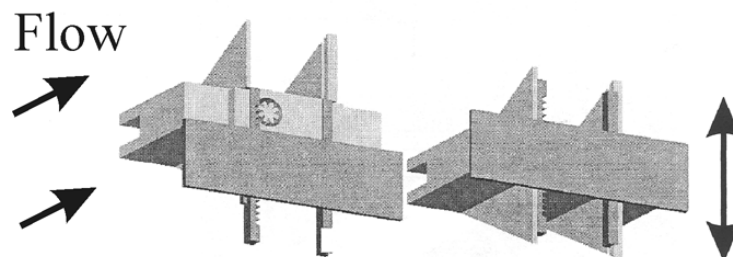


Fig. 2.3. CAD rendering of the MiTEs used by Solovitz and Eaton (2002)

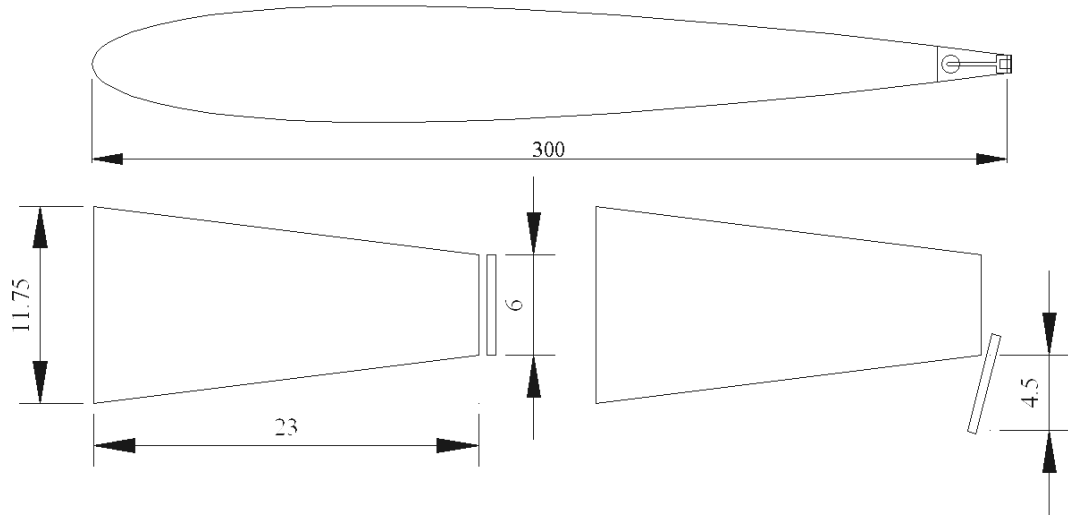


Fig. 2.4. Schematic of the airfoil and actuator cross-section. All dimensions are given in mm.

Namiki 6CD-1201WL-00 DC motor that was mounted inside the body of the MiTE. The motor was approximately 6 mm in diameter and 17 mm long. Each MiTE was $0.077c$ long in the streamwise direction and had a span of $0.03a$. When attached to the wing, there was a 2.7 mm spanwise gap between the bodies of consecutive MiTEs. After final assembly of the wing and MiTEs, in order to limit the leakage of air through these gaps, clear tape was placed along the trailing edge as far as $X'/c \approx 0.98$. Figure 2.5 shows a picture of one MiTE detached from the wing and oriented in the XZ plane, and Fig. 2.6 gives an oblique view of a MiTE. The flap motion was limited by two steel pins that acted as stops. The motor had a significant mechanical advantage as in the previous design, i.e., the force from the flow did not directly counter-act the torque produced by the motor. This allowed the small motor to easily hold the flap in the down position at test conditions.

Because this design was relatively simple, many MiTEs could be manufactured efficiently using standard machining techniques. The body of the MiTE was machined out of solid acrylic, the flap and flap arm were cut from a Delrin sheet by laser ablation, and the steel pins were cut from 0.76 mm diameter music wire. The motors were commercially available and of the type often found in handheld electronic devices. According to manufacturer specifications, they were rated for 7500 RPM at 1.3 V and 80 mA. For all experiments, the motors were run in a stalled condition at constant voltage up to 1.1 V for most of the experiment. The steady-state temperature of their outer surfaces was no more than 33°C .

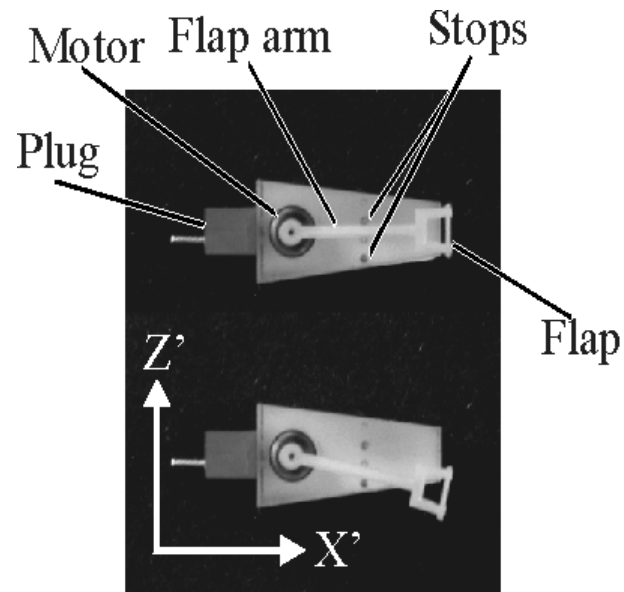


Fig. 2.5. Two dimensional view of a MiTE in the XZ plane.

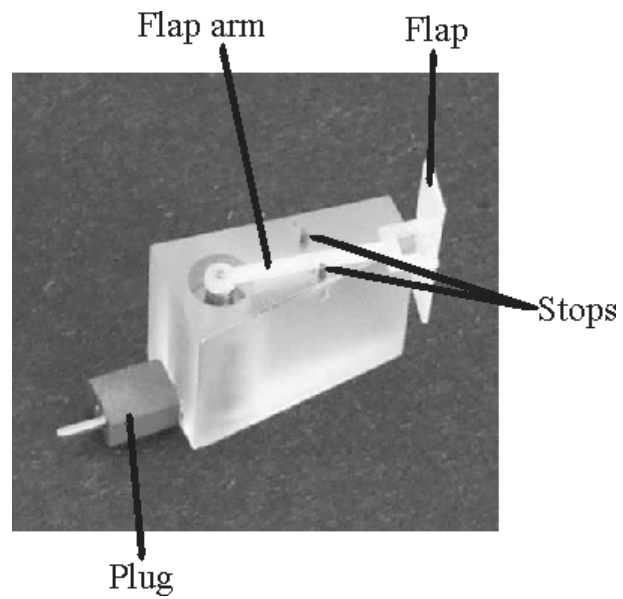


Fig. 2.6. Three dimensional view of a MiTE.



Fig. 2.7. A rear oblique view of the fully-assembled wing equipped with MiTEs.

at this condition. They could be run in a stalled condition for many hours at this voltage with no noticeable degradation in long term performance. Plastic plugs typical in small hobby applications were used for transmitting electrical power to the MiTEs. Each plug consisted of two halves which mated to one another. For each MiTE, one half of the plug was bonded to the upstream side of the MiTE body using epoxy. Its two prongs entered the motor housing through small holes and were soldered to the motor leads. The other half of the plug was embedded inside the wing near the trailing edge. This half had two wires soldered to the prongs that passed through the wing and exited at the root going directly to the MiTE power circuit. The wing was equipped with 27 MiTEs in all, though the one closest to the tip was never used. The 26 MiTEs used were always commanded in pairs. A rear oblique view of the wing with four MiTEs near the tip in the down position is shown in Fig. 2.7.

A Dell Precision 530 workstation with a National Instruments PCI-6025E data acquisition board (DAQ) was used to command the MiTEs. Each flap required two digital

Table 2.2. Logic chart for MiTE control.

Logic Command	Flap Position
01	Neutral
10	Down
00	No power

input/output (DIO) terminals to output a logic level signal from the DAQ. The logic chart is shown in Table 2.2. DIO signals were routed to the MiTE power circuit, a custom built circuit for relaying the necessary power to the motors.

The traces for the MiTE power circuit were printed using ExpressPCB, an online electronic board manufacturing service. The circuit consisted of thirteen bidirectional H-bridges wired in parallel and powered by two constant voltage source power supplies. One was for supplying voltage to the MiTEs ($V1$), and the other was for supplying voltage to the H-bridges ($V2$). $V2$ was set to 10 V, but $V1$ was variable and depended on the number of MiTEs being actuated at once. This was because the whole circuit consisted of many H-bridges connected in parallel. Thus, the resistance seen by the MiTE power supply would decrease with the number of MiTEs being actuated. This would cause the amount of voltage drop that occurs before the current reaches the MiTEs to increase significantly with the number of MiTEs being actuated. When more MiTEs were being actuated at once, $V1$ would need to be increased such that the voltage drop across the MiTEs was always 1.1 V.

The mechanical response of the MiTEs measured using a high speed CCD camera and a strobe light focused on the flaps is shown in Fig. 2.9. The MiTEs began in the neutral (0) position, then at $t^* = 0$, the computer sent a signal commanding them to switch to the down (1) position. After some delay time, the camera shutter opened, and the strobe light flashed once. The image gave the position of the flaps at the set delay time. To measure the flap motion as a function of time, we varied this delay time in 4 ms increments. Ten samples were collected and phase-averaged for each delay time. The right half of Fig. 2.9 is for the same experiment run in reverse, i.e., starting with the flaps in the down position and commanding them back to the neutral position. All mechanical response measurements were conducted with the wind tunnel at full test conditions. Locations of the four flaps closest to the tip were averaged at each time point, with the maximum variation amongst the four being less

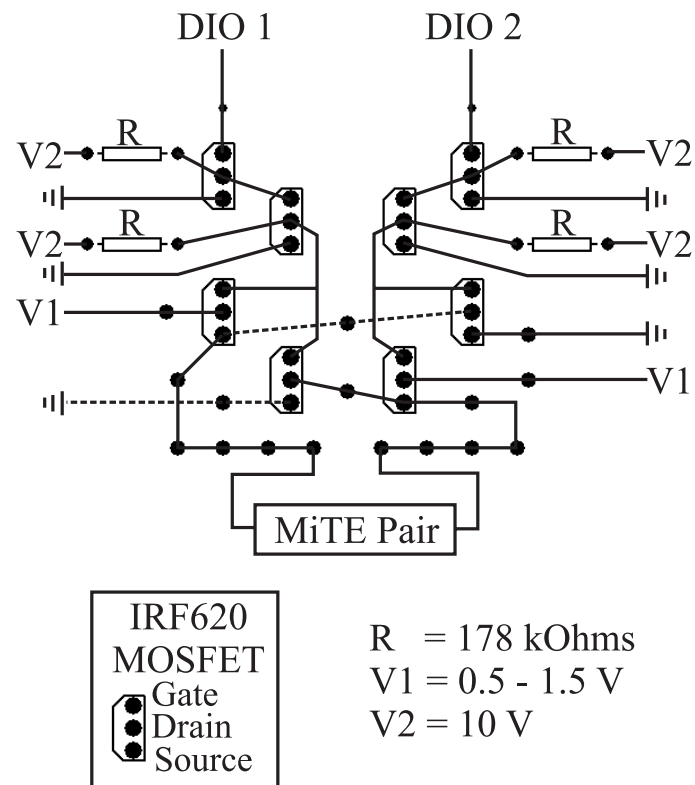


Fig. 2.8. The bidirectional H-bridge for relaying power to one MiTE pair. It is shown here as it appears on the PCB, dotted lines indicate the opposite side of the PCB.

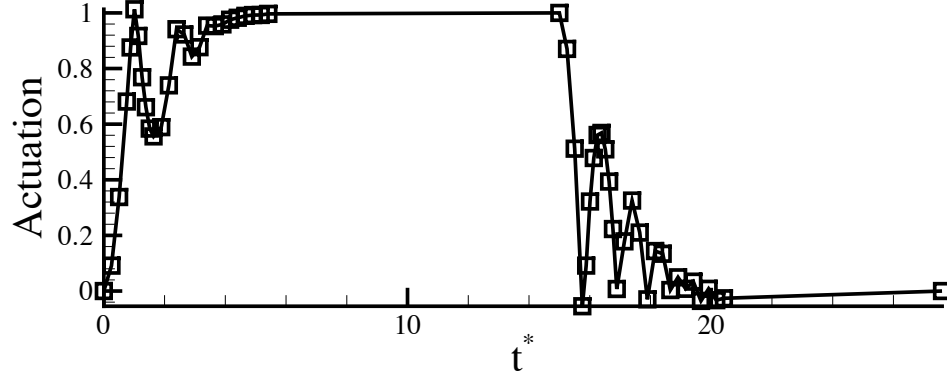


Fig. 2.9. The mechanical response of the four flaps closest to the tip at test conditions.

than 20% of the actuation height. The response was clearly under-damped. In moving from one position to the other, the flap would quickly accelerate then strike the metal stop at high speed causing it bounce several times before coming to rest. All attempts made to dampen this motion resulted in a loss of consistent behavior between MiTEs, and either a very slow actuation time, or only a marginal increase in damping. Short timescales present in the response were roughly $1.0t_{flow}$ ($t_{flow} = c/U_\infty$), while the timescale based on the response envelope was around three to four times t_{flow} . The freestream velocity used here was 18.9 m/s.

In order to quantify a given MiTE configuration, we defined two parameters: Y_{flap} and a_{down} . They are illustrated in Fig. 2.10. Y_{flap} was the spanwise location of the geometric centroid of the down MiTEs measured from the wing root. a_{down} was the spanwise length of down MiTEs. Both of these parameters were nondimensionalized by a . All MiTEs in the down position always formed a continuous group, i.e., no down MiTEs were ever separated by neutral ones.

2.1.3 Wind Tunnel

All tests were conducted in the Stanford Flow Control Wind Tunnel. Details regarding the tunnel are given in Compton (1995). This was a recirculating wind tunnel with a maximum velocity in the test section of 22 m/s, very good flow uniformity, and freestream turbulence intensities less than 0.5%. Test section dimensions were 91 cm high, 61 cm

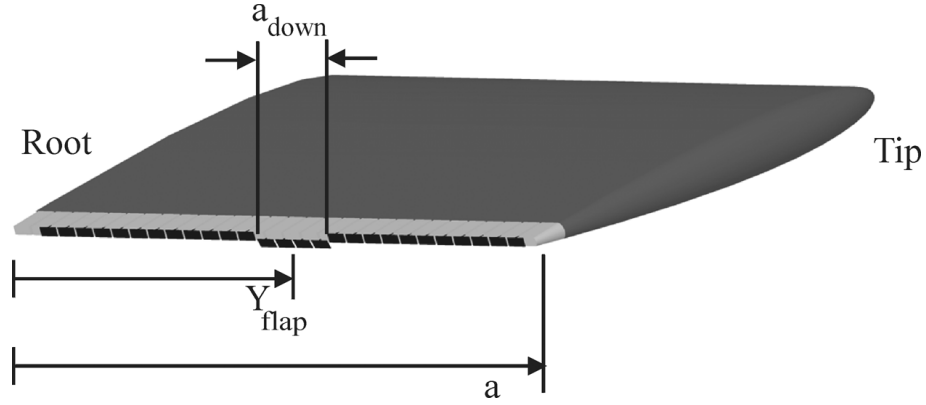


Fig. 2.10. Illustration of the parameters used to quantify the MiTE configuration.

wide, and 3.7 m long. The walls were made of clear 3/4" acrylic. There were three removable windows on the bottom wall of the test section for access to the experimental region. The tunnel was equipped with a heat exchanger for helping to maintain a constant flow temperature when running for long periods of time. In order to measure the velocity and temperature in the wind tunnel, a pitot-static probe and thermocouple probe were located just upstream of the wing and near the tunnel ceiling.

Most experiments were conducted with the wing at an 8.9 degree angle of attack. At this angle, the solid blockage ratio in the tunnel was roughly 7%.

All wind tunnel tests were performed at the following conditions. The freestream velocity was set between 18 and 20 m/s, thus, the Reynolds number with respect to the chord was roughly 350,000. Values of both the tunnel velocity and temperature were recorded for each data set, and used for nondimensionalizing the results. Absolute pressure in the tunnel was not monitored, but auxiliary tests showed it to be roughly 400 Pa greater than atmospheric pressure in the laboratory.

2.2 Measurement Apparatus

2.2.1 Pressure Profiles

In order to determine the forces experienced by the wing, we performed measurements using pressure taps at the locations shown in Fig. 2.11. Seven rows of pressure taps were cosine-spaced across the half-span of the wing in order to achieve better resolution near the tip where the section lift coefficient varied more with respect to spanwise location. Each

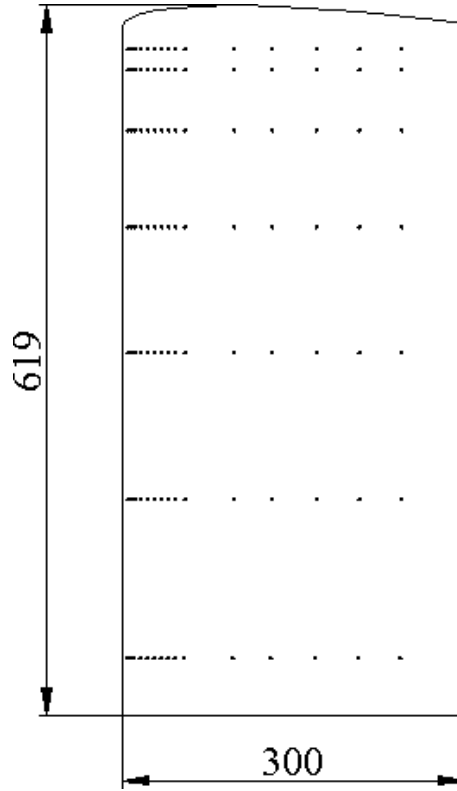


Fig. 2.11. The location of pressure taps on the wing. Taps are on both the pressure and suction sides. Dimensions are given in mm.

row consisted of 31 taps distributed chordwise across the pressure and suction sides of the wing. The taps were more densely spaced closer to the leading edge in order to improve resolution where the streamwise variation was more severe. Exact locations of the taps are given in tables 2.3 and 2.4.

To measure the streamwise profile at one spanwise station, all the tubes from that station were connected to a Scanivalve Model SSS 48C MK4 pressure-switching system using Micro Hose Quick Couplings (Quick-Connects). We controlled the Scanivalve with a Labview program and a National Instruments MIO-16 DAQ.

One Setra Model 264 0-2.5 in H_2O differential pressure transducer was used for these measurements. We connected the high pressure port on the transducer to the total pressure port of the pitot-static probe (p_T) at all times. This was done to ensure that the pressure measured would always be positive. The low pressure port was connected to the output of the Scanivalve such that it could be cycled through any tap (p_i) plus the static port of the

Table 2.3. Pressure tap locations along the chord of the wing. The upstream most point is omitted on the suction side.

X'/c
0.003
0.015
0.025
0.037
0.053
0.073
0.093
0.113
0.133
0.153
0.180
0.323
0.433
0.563
0.687
0.810

Table 2.4. Pressure tap locations along the span of the wing.

Y/a
0.081
0.302
0.509
0.686
0.822
0.908
0.937

pitot-static probe (p_S). Dynamic pressure in the freestream, $p_T - p_S$, was measured at the beginning and end of each spanwise station, and the average was used for calculating the pressure coefficients at that station. We collected 10,000 samples for each tap at 1000 Hz. Before sampling each tap, a 10 s wait time was used to allow any transients to die out.

Pressure coefficient, C_p , at each tap was calculated using

$$C_p = \frac{p_i - p_S}{\frac{1}{2}\rho U_\infty^2} = 1 - \frac{p_T - p_i}{p_T - p_S}. \quad (2.1)$$

The section lift and drag coefficients at each spanwise station were calculated by integrating the pressure coefficient and projecting the quantity in the appropriate direction. We began by calculating the normal and axial coefficients about the airfoil shape using

$$C_n = \oint C_p d\left(\frac{X'}{c}\right), \quad (2.2)$$

$$C_a = \oint C_p d\left(\frac{Z'}{c}\right). \quad (2.3)$$

The lift and drag coefficients could then be found using the angle of attack, α , through

$$C_l = C_n \cos \alpha - C_a \sin \alpha, \quad (2.4)$$

$$C_d = C_a \cos \alpha + C_n \sin \alpha. \quad (2.5)$$

All integration was performed numerically using the trapezoid rule. Since it was not physically possible to place pressure taps near the trailing edge of the wing or on the MiTEs, the furthest streamwise position where we collected pressure data was at $X'/c = 0.81$. The Kutta condition was applied at the trailing edge of the wing, thus, for evaluating the integrals C_p at $X'/c = 1.0$ was assumed to be zero. At the leading edge, there were pressure taps at $X'/c = 0.003$ on the pressure side of the wing. These were sufficiently close to the true leading edge for calculating the lift and drag.

Due to the reasonably small blockage ratio (7% at $\alpha = 8.9^\circ$), no blockage corrections were made. Comparison to tabulated data on standard, sharp trailing edge NACA 0012 airfoils (Jacobs and Sherman 1937) showed very good agreement (<4% difference). These differences could easily be attributed to the blunt trailing edge. Also, the wind tunnel walls created images of the trailing vortex oriented in the streamwise direction. The closest image

vortex induced a very small velocity at the real vortex position (less than 4% of U_∞), thus, no attempts were made to correct for this.

2.2.2 Five-Hole Probe

According to the estimates of Spreiter and Sacks (1951), the point at which the vortex is essentially fully rolled up occurs at $X/c \approx 2.75$. We designate measurements performed upstream of this notional point as near wake measurements, and downstream of this point as intermediate wake measurements.

The primary purpose of taking measurements in the near wake was to examine how the streamwise evolution of the trailing vortex was modified by the MiTEs. We took measurements in the intermediate wake, however, to examine the streamwise and radial velocities in a large enough domain such that all necessary parameters for the vortex filament computations could be determined.

A five-hole probe was used to carry out these measurements so we could efficiently make steady-state measurements of three components of velocity on a large grid, and also take measurements very close to the wing. To do this with particle image velocimetry (PIV) would have been inefficient and difficult due to the number of optical alignments that would have been necessary to measure a large domain, and the glare from scattered light due to background geometry in the region of interest. Also, 2D PIV could not produce the streamwise velocity component in the desired measurement plane.

The probe and its orientation in the wind tunnel are shown in Fig. 2.12. Details regarding this probe are given in Pauley (1988). It was machined out of aluminum, and the tip of the probe was 2.8 mm in diameter and had five facets, each with one hole. The total pressure hole was on the facet which directly faced the freestream, while the other four facets were at 45° angles to that plane. Each hole was approximately 0.5 mm in diameter. The probe was secured to a 3/8" OD stem made of stainless steel with a "cobra head" shape in order to minimize stem interference.

Each hole on the probe tip was plumbed through a thin plastic tube which traveled through the entire stem and exited out of the other end. The tubes were connected to the five-hole probe control box which is shown schematically in Fig. 2.13. The box contained five Setra Model 264 0-2.5 in H_2O transducers, seven Clippard Minimatic (EVO-3) 6 VDC solenoid valves, and a simple relay circuit for converting digital output signals from the DAQ to large current signals for the valves. This circuit consisted of seven single-polarity

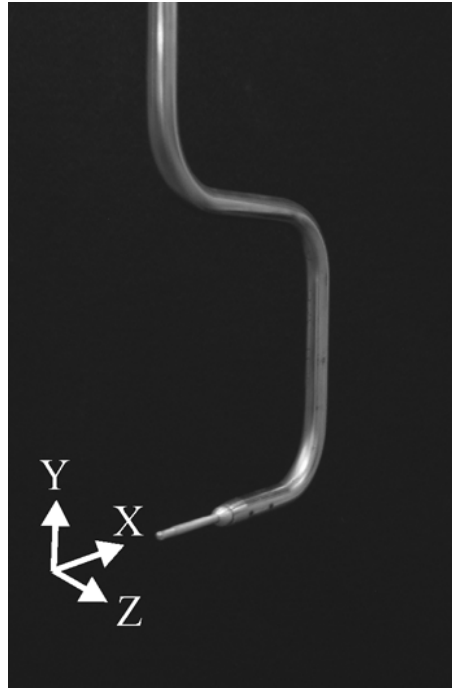


Fig. 2.12. The five-hole probe as it was oriented in the wind tunnel.

switches configured in parallel. A circuit diagram of one switch is shown in Fig. 2.14. This circuit was also printed using ExpressPCB. An external power supply set to 6 V was used for powering the valves.

Five transducers were used in order to simultaneously collect data from all of the probe holes. This allowed for relatively rapid measurements, but also required that five transducers each be calibrated, adding to the uncertainty as will be shown later. As illustrated in Fig. 2.13, the high pressure port on each transducer was connected to the total pressure hole on the pitot-static probe. The solenoid valves were used to frequently reset the zero level on each transducer. In the non-actuated state, the transducers compared tunnel total pressure to probe pressure. In the actuated state, the transducers received total pressure on both sides resulting in no pressure difference. This allowed us to zero the transducer easily during an experiment. The zero level was reset between every ten measurement points in order to eliminate transducer drift as a source of uncertainty.

For each measurement point, the order of events was as follows: the traverse was moved to the correct location, the computer would wait 10 s to allow transients to die out before sampling, then 10,000 samples from each transducer were collected at 1,000 Hz. Velocity

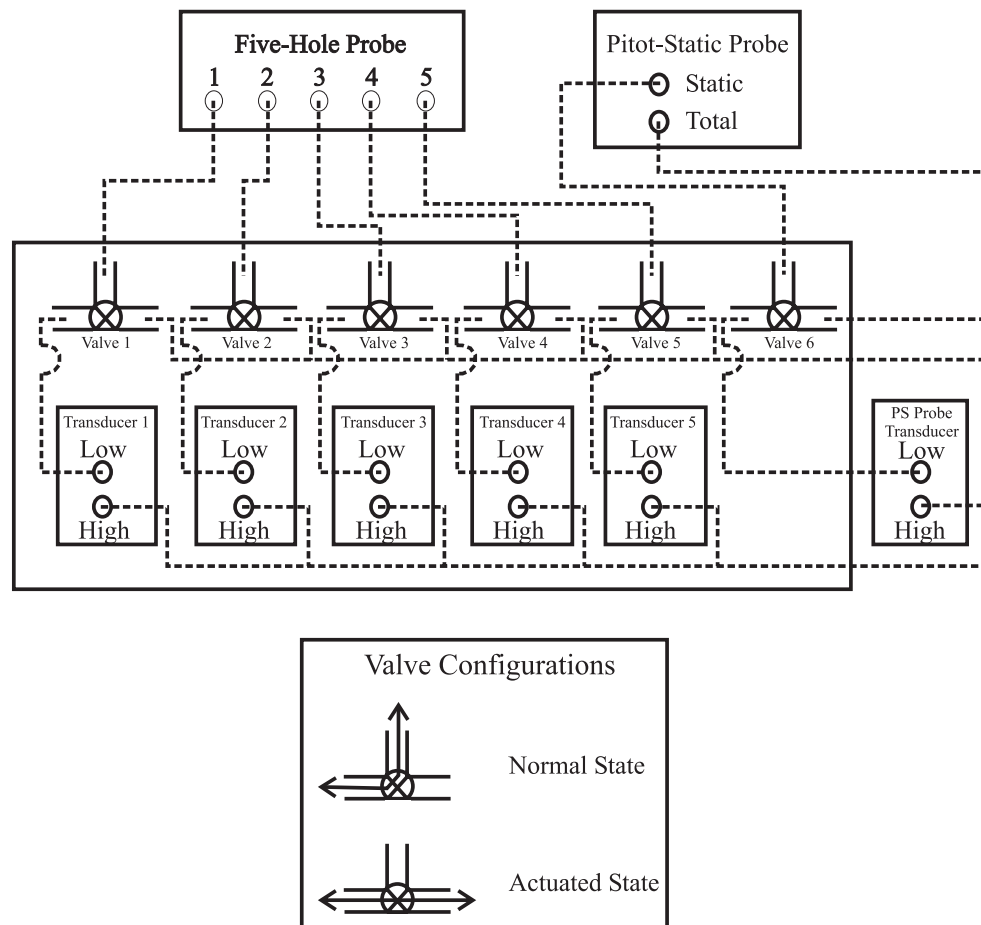


Fig. 2.13. Schematic of the five-hole probe control box and surrounding equipment.

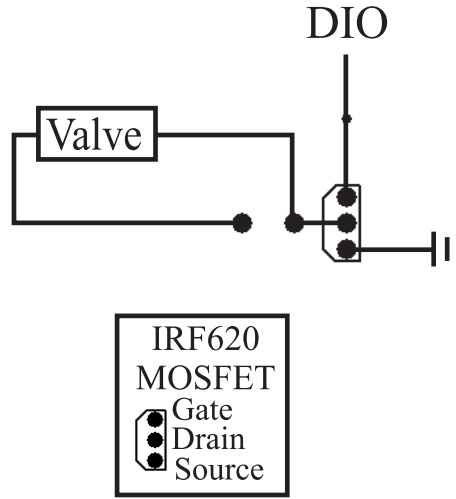


Fig. 2.14. Circuit diagram of the single-polarity switch for powering the solenoid valves.

gradients at most points in the flow were low, and a 10 s wait time was sufficient. To accommodate the small region near the vortex core where gradients were higher, a simple standard deviation filter was used as follows. If the standard deviation in any pressure measurement was greater than the threshold value of 0.5 Pa, the data taken for that point were discarded and the measurement repeated. The threshold value was determined by some simple test cases with synthetic data. This basic idea was recommended by Mr. Greg Zilliac of NASA-Ames Research Center and allowed us to collect data sets within a reasonable amount of time. One dataset consisting of 300 points would require three to four hours of continuous data acquisition.

Three slots in the Z -direction were cut into the ceiling of the wind tunnel at $X/c = 0.20, 0.83$, and 4.9 . Weather-stripping was placed in the slots to minimize air leakage during testing. The stem was secured to a YZ traverse mounted on top of the tunnel. Each axis of the traverse was powered by a Superior Electric Slo-Syn stepper motor. The stepper motors were controlled using Slo-Syn motor controller units. Digital outputs from the DAQ were used to command the motor controllers to position the traverse.

At near wake positions, we examined both a coarse 17×17 grid with 12.5 mm resolution as well as a more refined grid with twice the resolution and a smaller domain size. At the intermediate wake position, only a coarse 17×17 grid with 12.5 mm resolution was examined.

2.2.3 Particle Image Velocimetry

Particle image velocimetry (PIV) measurements were used to obtain high resolution velocity data on the wing tip vortex. This allowed for the details of the vortex core to be measured, and for the vortex center to be accurately located. We used a commercial system from TSI, Inc. consisting of a high power pulsed laser, CCD camera, synchronizer, and data collection software. We designed and constructed the necessary optics for flow illumination using commercially available lens elements.

The entire experimental apparatus configured for PIV is shown schematically in Fig. 2.15. A picture of the wind tunnel as it would appear during PIV experiments is given in Fig. 2.16. In order to limit the amount of ambient light in the images, a vinyl curtain was placed around the entire test section. The flow was illuminated with a Spectra-Physics dual head pulsed Nd:YAG laser capable of over 400 mJ per 10 ns pulse for each head. The energy typically used was between 150 and 200 mJ/pulse, and the wavelength of the emitted beam was 532 nm. To measure the tangential velocities in the vortex, a constant thickness laser sheet was oriented perpendicular to the streamwise direction. This departed from typical PIV configurations in that there was a strong out-of-plane velocity component due to the freestream. However, due to the short time between laser pulses, the thickness of the laser sheet, and the large ratio of tangential to streamwise velocity components, accurate velocity measurements could be made. This type of PIV configuration has been used by others, and is discussed further in Raffel et al. (1998).

A picture of the laser and optics with a sketch of the beam path is shown in Fig. 2.17. The beam produced by the laser was roughly 8 mm in diameter. We used a series of mirrors to direct the beam to the optical rail which carried all of the lens elements. To produce a laser sheet that was roughly 2.5 mm thick, three lens elements were used: a plano-convex element ($f' = 150$ mm) to focus the beam, a plano-concave element ($f' = -50$ mm) to recollimate the beam, and a plano-concave cylindrical element ($f' = -19$ mm) to expand the beam in only one direction making it a sheet. As long as the effective distance between the first two elements was equal to the sum of their focal lengths (100 mm), the system was afocal, and the final result was a sheet of constant thickness. The focal length of the cylindrical lens was chosen such that the sheet was wide enough to provide homogeneous illumination throughout the measurement domain. Note that since this lens configuration combined a positive and negative lens element, high order optical aberrations were quite small. Also, since the intensity thresholds on most anti-reflective coatings were too low for

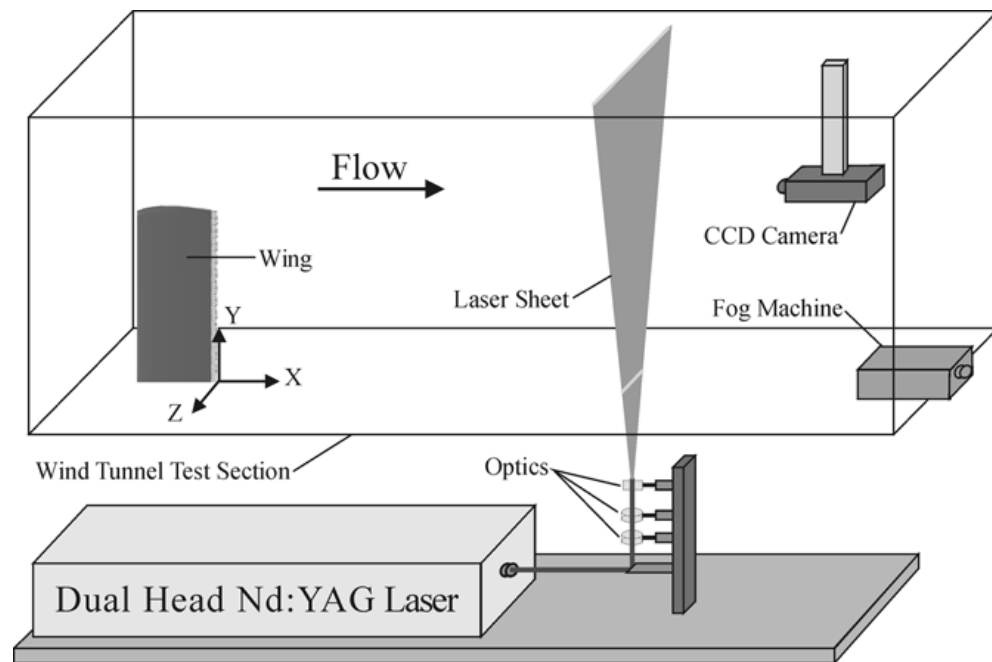


Fig. 2.15. Schematic of the entire experimental apparatus configured for PIV.

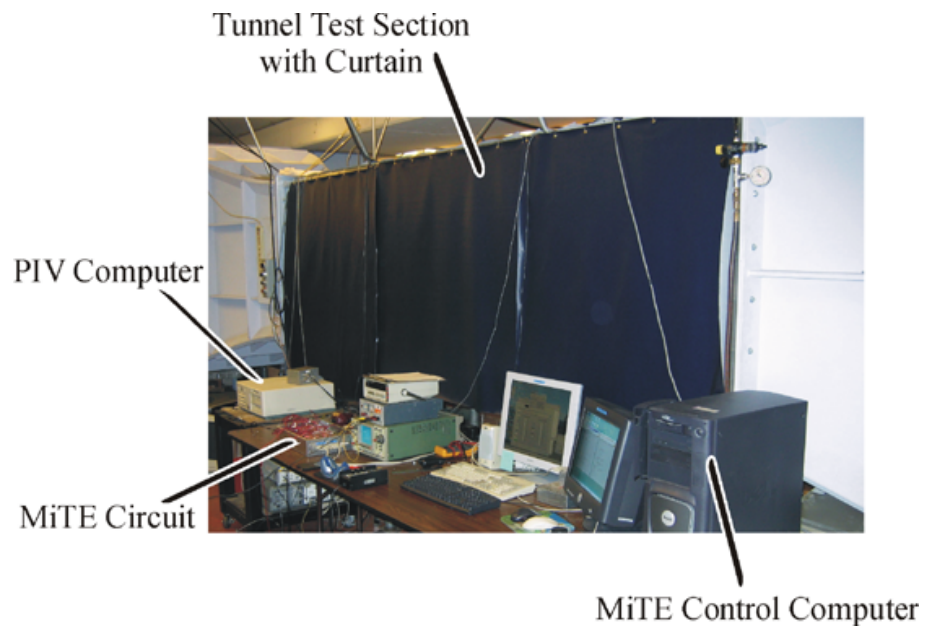


Fig. 2.16. Picture of the test section configured for PIV experiments.

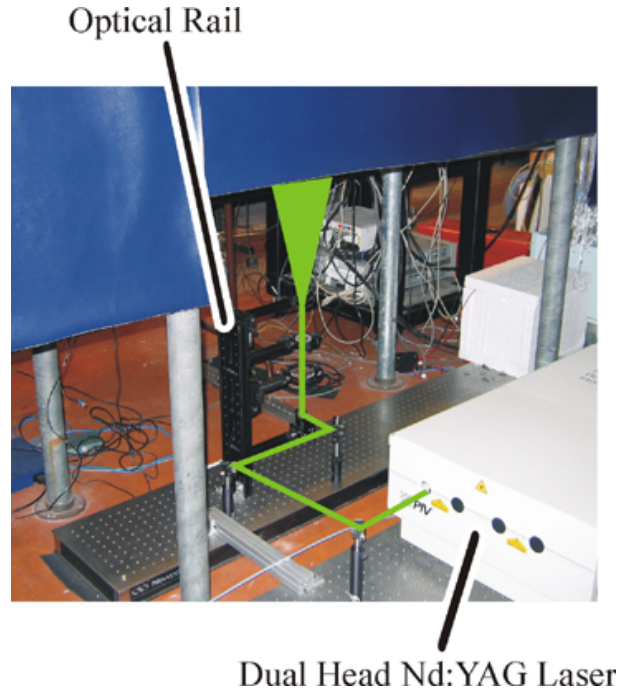


Fig. 2.17. The optical beam path.

this application, all of the lens elements used were made of uncoated BK7 glass.

We conducted PIV measurements at three streamwise positions in the intermediate wake: $X/c = 2.8, 3.8$, and 4.9 . For the first two locations, the laser sheet was passed through the middle tunnel access window. A special window was constructed for this purpose which had a glass center for good optical clarity. For the position furthest downstream, an existing slot in the bottom of the tunnel at $X/c = 4.9$ was covered with glass on the inside of the tunnel. The disturbance to the flow was negligible as the glass thickness was well within the tunnel wall boundary layer.

PIV image pairs were captured using a 12 bit, 1.3 megapixel Kodak 13-8 CCD camera with a Nikon Micro-Nikkor 105 mm lens. The camera was contained in a box to shield it from the flow and suspended inside the wind tunnel with the box front surface roughly 0.75 m downstream of the laser sheet. This is illustrated in Fig. 2.2. To suspend and position the camera, a vertical traverse was mounted on the outside ceiling of the tunnel test section on a cart which rode on rails allowing it to move in the streamwise direction. An aluminum strut was connected to the traverse and passed into the test section through an existing streamwise slot in the ceiling. We connected this vertical strut to a horizontal strut that

spanned the width of the wind tunnel. The horizontal strut was equipped with rubber-coated leadscrews on its ends that could be extended such that they would press against the walls of the wind tunnel to hold the camera securely during testing. We mounted the camera to the horizontal strut using bolts.

The box that shielded the camera was made of aluminum and acrylic with a glass surface in the front for good optical clarity. Its dimensions were 45.7 cm \times 15.2 cm \times 19.1 cm in X , Y , and Z , respectively. Potential flow analysis showed that the effect of the camera box upon the measurement region was negligible. This was confirmed by conducting five-probe measurements both with and without the camera in the tunnel. There was no measurable effect. The camera was cooled using an external air pump to supply the box with a gentle flow of cooling air. The box was equipped with a removable access window on its side to allow for focus and aperture adjustment of the camera lens.

A Rosco fog generator was placed at the very end of the tunnel test section and used to seed the flow. The fog fluid consisted of 50% water and 50% glycerol by volume. The fog droplets remained suspended as the flow circulated through the closed-loop wind tunnel. We controlled the fog machine by a remote trigger switch. During experiments, the level of seed in the flow was maintained manually by periodically pulsing the fog momentary trigger at a low fog volume setting.

To align and calibrate the system, we began with the laser beam optics. The only critical distance amongst the three lens elements on the optical rail was the distance between the two spherical elements. This was adjusted to achieve proper recollimation of the beam. The optical rail was mounted vertically as shown in Fig. 2.17 and placed in the appropriate location beneath the wind tunnel. We then added the remaining lens element and mirrors to produce the desired laser sheet. Reflections from the tunnel surfaces and a digital angle finder were used for aligning and positioning the laser sheet.

The calibration target pictured in Fig. 2.18 was used to position and focus the camera. Once the laser sheet was aligned, the target was mounted inside the tunnel in the measurement region. It was suspended from the tunnel ceiling through the streamwise slot and secured with a bolt. We placed the target such that it bisected the laser sheet thickness in order to ensure that the camera would be focused on the brightest part of the laser sheet. Once the placement was correct, the laser was powered down and an image of the target using only conventional lighting was taken. A sample calibration image is shown in Fig.

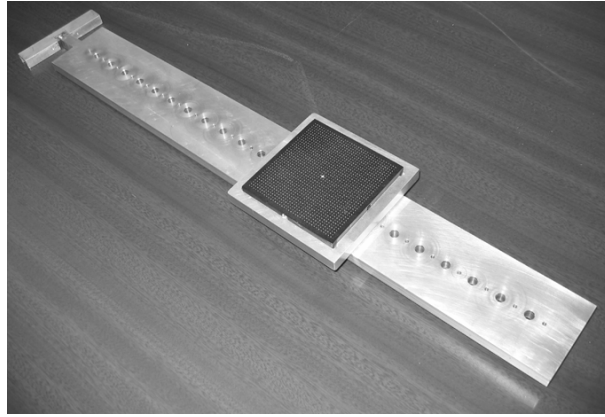


Fig. 2.18. The calibration target used for PIV.

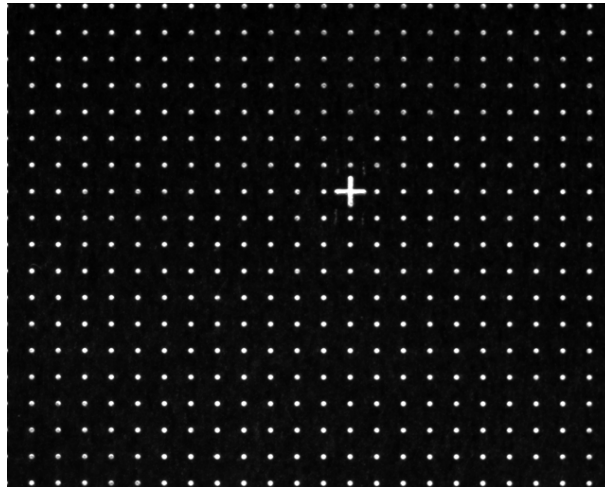


Fig. 2.19. Sample calibration image.

2.19. The calibration factor and cross-hairs location were then noted to be used in post-processing. Calibration factors were around 22 pixels/mm, and the size of the measurement domain was roughly 4.5 cm in the Y direction and 6 cm in the Z direction.

The precise timing between the flashlamps, q-switches, camera, and frame-grabber card was achieved by a TSI Model 610034 synchronizer. Timing parameters were set in the TSI software, and were sent to the synchronizer upon the initiation of a PIV sample. The image pair separation time was 20 μs , the flashlamps were fired at 10 Hz, and data were collected at roughly 1 Hz. All data were saved directly to the computer hard drive.

For each static PIV experiment, we set the MiTEs in a particular configuration and held

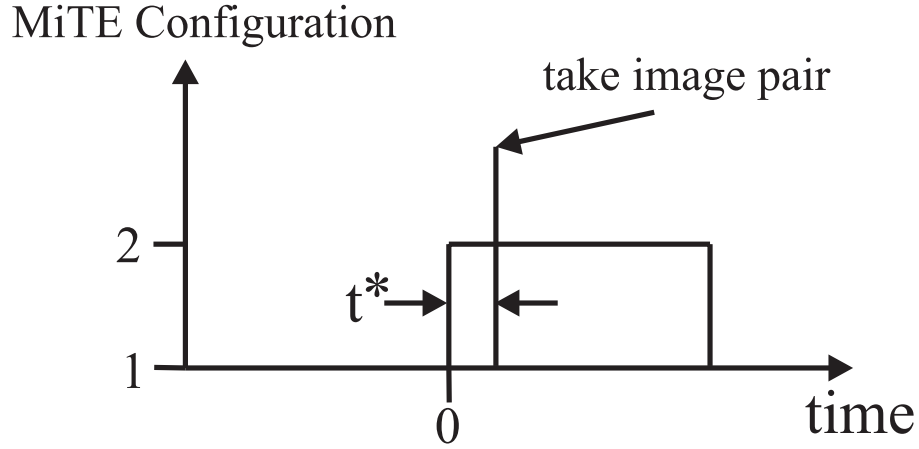


Fig. 2.20. The timing of a dynamic PIV sample.

them there for the duration of the experiment. The resulting vector fields could then be ensemble-averaged to produce steady-state data.

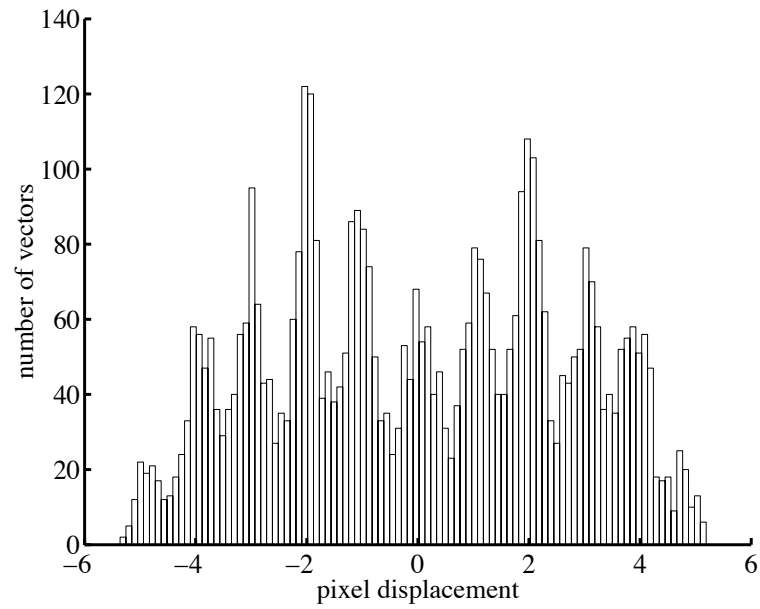
Phase-locked PIV sampling was used to resolve the coherent dynamic flow response to MiTE actuation without the need for a high-speed PIV system. For each dynamic PIV experiment, an actuation scheme that consisted of two static MiTE configurations (1 and 2) was examined. The MiTEs were actuated periodically between configurations 1 and 2. Typically the period was set to 1 s. We were only interested in the transient flow response as the MiTEs moved from one configuration to the other. Thus, the actual period was unimportant. It was selected to insure that all transients had died out and for experimental convenience. A timing diagram for measuring the transient response going from configuration 1 to 2 is shown in Fig. 2.20. The MiTEs were initially in configuration 1, then at time $t^* = 0$, they were commanded to move to configuration 2. At nondimensional time t^* , the computer triggered the PIV system to acquire an image pair. The nondimensional time, t^* , ranged from $0 < t^* < 10$ in intervals of 0.32. The time between the two laser pulses required for a single PIV velocity field measurement was $20 \mu\text{s}$ ($0.0013t_{flow}$). This inter-image separation time was insignificant relative to the t^* interval. A set of 200 image pairs was acquired for each set value of t^* , and the 200 instantaneous velocity fields were averaged to give the phase-averaged velocity field. This process was repeated for a minimum of 18 different values of t^* for the actuation of the MiTEs from configuration 1 to 2, and an additional minimum of 18 values of t^* for the actuation from configuration 2 to 1.

All PIV image pairs were processed using PIVLab2000, a Matlab program developed at

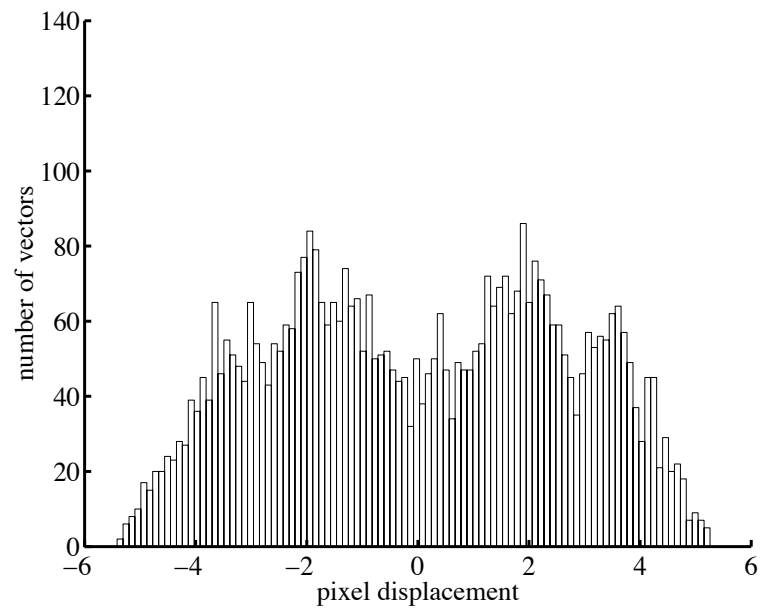
Stanford. The details of this program are given in Han (2001). The program used iterative discrete window offset, and relied heavily on the 2D Fast-Fourier transform functions built into Matlab for performing the necessary convolutions. A 50% overlap was used to increase the number of vectors produced. This resulted in a vector spacing of 0.7 mm. Five iterations were performed. The first iteration performed image shifts on windows that were 64×64 pixels large. All subsequent iterations were on 32×32 pixel windows, with the search range decreasing with each iteration. The consistency filter built into PIVLab2000 was used to eliminate bad vectors. The filter criteria were as follows. For each vector, the surrounding eight vectors were examined. If more than 4 of the surrounding vectors' pixel displacement differed by more than 3 compared to the vector in question, the vector was removed and replaced by an interpolation of the surrounding vectors. Pixel displacements for a typical image pair ranged from 0 to 6. All image pairs had less than 1% of vectors filtered out.

The most important parameter extracted from the PIV data was the vortex center location which we defined as the location of minimum in-plane velocity magnitude. This was done for each individual vector field by the following procedure. First, we computed the in-plane velocity magnitude field, $(V^2 + W^2)^{\frac{1}{2}}$, and convolved it with a 15×15 grid point ($10.5 \text{ mm} \times 10.5 \text{ mm}$) Gaussian kernel. Note that this filtering was only performed in order to find the center; all velocity data presented in this work are unfiltered. Finally, the minimum value of this field was located, and the subgrid minimum was found by three-point linear interpolation. The size of the Gaussian kernel was determined by examining a range of sizes. The center location converged quickly as we increased the kernel size. We took one typical PIV sample and tabulated calculated vortex center location as we increased the filter size. The changes were close to or smaller than the uncertainty in the measurement, but to be as accurate as possible, a 15×15 kernel was used.

The final processing step was to apply the sub-pixel accuracy equalization technique to each instantaneous vector field. This correction technique is discussed in detail by Roth and Katz (2001). It can be used to improve the accuracy of PIV data when integer peak-locking occurs due to small seed particles. Two histograms from a typical vector field are shown in Fig. 2.21. Clearly, the peak-locking is attenuated by this technique. Using synthetic data, Roth and Katz showed that the change tends to improve the accuracy of the data.



(a) Uncorrected



(b) Corrected

Fig. 2.21. Two histograms from a typical vector field showing the effect of sub-pixel accuracy equalization.

Table 2.5. Calculated vortex center location (spanwise coordinate only) as filter size is increased.

Filter Size (gridpoints)	Y_{center} (mm)
3×3	555.07
5×5	554.83
7×7	554.74
9×9	554.71
11×11	554.69
13×13	554.68
15×15	554.67

2.3 Experimental Uncertainty

The experimental uncertainty for each measurement technique is described in the following sections. We use traditional techniques for uncertainty analysis as described in Figliola and Beasley (1995). All uncertainties are based on 95% confidence intervals.

The emphasis in all experiments was on measuring and comparing the results from different MiTE configurations. Thus, we only considered sources of uncertainty that would cause differences between the various cases. Bias errors that affected all datasets in the same way, such as geometric uncertainty in the wing shape or tunnel blockage effects were irrelevant, and were not considered. All cited uncertainties were verified by repeatability tests.

2.3.1 Pressure Profile Uncertainty

The three sources of uncertainty that contribute to the uncertainty in C_p are statistical uncertainty, transducer drift, and uncertainty in angle of attack. The equation for C_p in terms of the transducer output voltage is given by

$$C_p = 1 - \frac{CF(V_i - V_0)}{CF(V_\infty - V_0)}. \quad (2.6)$$

where V_i and V_∞ are the measured transducer outputs for tap i and the static pressure port on the pitot-static tube respectively, V_0 is the transducer zero measured once at the

beginning of each experiment, and CF is the calibration factor. The calibration factor cancels out of the equation for C_p , thus, it does not contribute to the uncertainty.

The statistical uncertainty is based on the highest standard deviation measured for any pressure tap. The number of samples is $N = 10,000$. Contributions of statistical uncertainty from V_i , V_∞ , and V_0 were combined to give the total statistical uncertainty, $(\Delta C_p)_{stat} = \pm 0.0001$.

Transducer drift is due primarily to changes in ambient temperature and results in an error in the transducer zero, V_0 . Auxiliary experiments were performed to determine the maximum amount that the zero value would change over the course of one day with temperature changes of roughly 4°C . The maximum change in V_0 was 2.8 mV. With this, the uncertainty in C_p due to transducer drift was $(\Delta C_p)_{drift} = \pm 0.0044$.

The angle of attack was set to 8.9° by pushing the threaded rod near the trailing edge of the wing to the end of the curved slot in the window. This made setting the angle of attack to 8.9° very repeatable. The uncertainty in angle of attack was approximately $\pm 0.05^\circ$. The uncertainty in C_p at each spanwise station could then be calculated. Spanwise stations closer to the root were more sensitive to angle of attack than stations near the tip. The maximum uncertainty in C_p due to uncertainty in angle of attack, $(\Delta C_p)_\alpha = \pm 0.0078$.

All of these sources of error are combined in root-sum-square fashion to calculate the total uncertainty. The total uncertainty in C_p at each spanwise station is given in Table 2.6.

The uncertainty in C_l and C_d are calculated through Eqs. 2.2 and 2.3 and standard propagation of error. The integrals were performed numerically using the trapezoid rule, thus, to be conservative, the terms in the numerical integral were treated as correlated to one another. ΔC_l at each spanwise location are given in Table 2.6. The uncertainty in C_d at all spanwise locations is ± 0.001 . This low uncertainty in C_d is due to much lower sensitivity to angle of attack.

Finally, the uncertainty in the total lift coefficient, C_L is determined directly from the uncertainties in each C_l value using the same technique. The uncertainty in C_L is ± 0.0031 .

2.3.2 Five-Hole Probe Uncertainty

All velocity measurements were nondimensionalized with the freestream velocity measured during each experiment. This implies that there was a contribution to the uncertainty in the nondimensional velocities from the error in the freestream velocity measurement.

Table 2.6. The uncertainties in pressure profile measurements.

Y/a	ΔC_p	ΔC_l
0.081	± 0.0090	± 0.0045
0.302	± 0.0090	± 0.0045
0.509	± 0.0082	± 0.0041
0.686	± 0.0073	± 0.0037
0.822	± 0.0061	± 0.0031
0.908	± 0.0049	± 0.0025
0.937	± 0.0044	± 0.0022

However, the error in the freestream velocity measurement was very small (± 0.02 m/s), thus, the additional uncertainty on the nondimensional velocities due to this was negligible. We present all velocity uncertainties in dimensional form, and their nondimensional form can be calculated by simply dividing by the nominal freestream velocity of 18.5 m/s.

The three sources of uncertainty in the five-hole probe measurements are transducer uncertainty, uncertainty in the wing angle of attack, and positioning uncertainty due to the traverse system. The uncertainty in the velocities measured by the five-hole probe due to transducer error depended upon the uncertainty in the measurement of each individual pressure, Δp_i , as well as the sensitivity in velocity to changes in pressure, $\partial U_i / \partial p_j$. The uncertainty in any velocity component, U_i , due to transducer error was

$$(\Delta U_i)_{XDR} = \left(\sum_{j=1}^5 \left(\frac{\partial U_i}{\partial p_j} \Delta p_j \right)^2 \right)^{\frac{1}{2}}. \quad (2.7)$$

The sensitivities were determined by perturbation analysis of several data sets. The uncertainty in pressure, Δp_i , was ± 0.1 Pa. This was determined by auxiliary experiments and took into account shift any in the transducer calibration factor. Thus, the uncertainty in each velocity component due to transducer error was

$$(\Delta U)_{XDR} = \pm 0.02 \text{ m/s}, \quad (2.8)$$

$$(\Delta V)_{XDR} = \pm 0.01 \text{ m/s}, \quad (2.9)$$

$$(\Delta W)_{XDR} = \pm 0.01 \text{ m/s.} \quad (2.10)$$

The uncertainty in wing angle of attack contributed to the uncertainty in the tangential velocity components by affecting the circulation in the vortex. We take the sensitivity to angle attack of the root section lift coefficient from the previous section, $\partial C_l / \partial \alpha = 0.078$. We can convert this to circulation sensitivity through differentiating Eq. 1.1 with respect to α to yield

$$\frac{\partial \Gamma_0}{\partial \alpha} = \frac{1}{2} U_\infty c \frac{\partial C_l}{\partial \alpha}. \quad (2.11)$$

For an inviscid vortex,

$$V_\theta = \frac{\Gamma_0}{2\pi r}, \quad (2.12)$$

where V_θ is the tangential velocity, and r is the distance from the vortex center. Thus, differentiating with respect to α yields

$$\frac{\partial V_\theta}{\partial \alpha} = \frac{1}{2\pi r} \frac{\partial \Gamma_0}{\partial \alpha}. \quad (2.13)$$

The value of r was taken to be 15 mm which was roughly equal to the vortex core radius based on maximum tangential velocity. Substituting these values into Eq. 2.13, the sensitivity is

$$\left| \frac{\partial V_\theta}{\partial \alpha} \right| = 2.3 \text{ (m/s)/}^\circ \quad (2.14)$$

Taking the uncertainty in angle of attack to be ± 0.05 degrees as before, the uncertainty in tangential velocity due to uncertainty in angle of attack, $\Delta V_\theta = \pm 0.12 \text{ m/s}$.

Finally, the error due to the traverse bearing resulted in a position uncertainty of $\pm 1 \text{ mm}$. The highest velocity gradient measured is 0.13 (m/s)/mm . Thus, the uncertainty in velocity due to the traverse, $(\Delta U_i)_{trav} = \pm 0.13 \text{ m/s}$.

Combining all of these sources of uncertainty, the total uncertainty in the five-hole probe measurement for each velocity component was

$$(\Delta U) = \pm 0.14 \text{ m/s,} \quad (2.15)$$

$$(\Delta V) = \pm 0.18 \text{ m/s,} \quad (2.16)$$

$$(\Delta W) = \pm 0.18 \text{ m/s.} \quad (2.17)$$

2.3.3 PIV Uncertainty

The uncertainty in the mean velocity measurements from PIV was due to statistical uncertainty and uncertainty in the wing angle of attack. For the statistical uncertainty, we use the maximum standard deviation in velocity $(\sigma_{U_i})_{max} = 1.10$ m/s. For the static PIV, 500 samples were taken, thus $(\Delta U_i)_{stat} = \pm 0.10$ m/s. For the dynamic data, 200 samples were taken, thus, $(\Delta U_i)_{stat} = 0.15$ m/s.

Accounting for the uncertainty in the wing angle of attack in the same manner as we did for the five-hole probe data yielded $\Delta V_\theta = \pm 0.12$ m/s. Adding this, the total uncertainty in velocity was $\Delta U_i = \pm 0.15$ m/s for static data and ± 0.19 m/s for dynamic data. This implied an uncertainty in vorticity, $\Delta \omega = \pm 210$ s⁻¹ for static data and ± 266 s⁻¹ for dynamic data.

The most important parameter extracted from the PIV data was the vortex center location. As previously described, the vortex center was located for each instantaneous velocity field, then all center locations were ensemble-averaged to calculate the mean vortex center location. Statistical uncertainty in the vortex center location measurement was found to be negligible compared to the repeatability in the measurement. This likely was because several factors which were impossible to properly quantify contributed to this uncertainty, such as slight flex in the walls of the wind tunnel or very small shifts in the position of the CCD camera. Thus, the uncertainty calculation that proved to be most conservative was the repeatability in the measurement, ± 0.3 mm. This quantity was based on extensive repeatability tests from experiments run over long periods of time.

Chapter 3

Experimental Results

3.1 Wing Aerodynamic Characteristics

3.1.1 Neutral Case

We began by examining the aerodynamic characteristics of the clean wing (all MiTEs in the neutral position). This was done to establish a baseline and confirm that the characteristics of the wing, with its blunt trailing edge, did not differ substantially from a standard NACA 0012 wing.

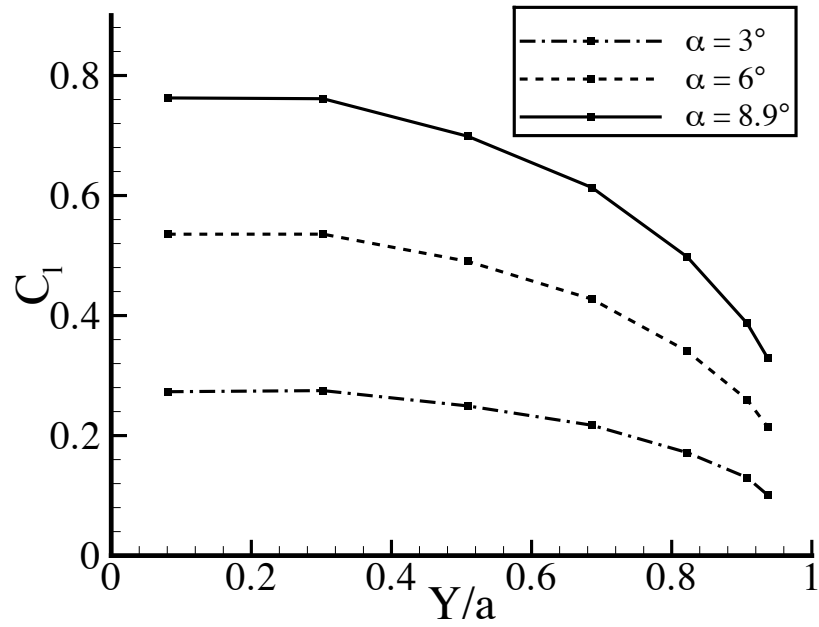
Section lift and drag coefficients, C_l and C_d , along the span of the wing are plotted in Figs. 3.1 and 3.2 respectively. The data showed a standard loading distribution where the lift coefficient was highest at the root, and fell as we approached the tip. The same was true for the drag coefficient. Note that between the two spanwise stations closest to the root, neither the lift nor the drag coefficients changed by very much. Thus, the flow near the root of the wing was essentially two-dimensional, and we could compare the section lift and drag values there to tabulated data on NACA 0012 airfoils. This is shown in Table 3.1. We found very good agreement of section lift coefficient values to tabulated data from Jacobs and Sherman (1937). The drag coefficients on our wing, however, were higher. This was expected due to the large induced drag created by the tip vortex in the current experiment. It was also reasonable to assume that the blunt trailing edge would cause some additional form drag. These results show that the MiTEs and blunt trailing edge had no significant effect on wing performance except for some additional drag. Note that the values taken from Jacobs and Sherman include parasitic drag. At this Reynolds number, however, the parasitic drag is small compared to the form drag (roughly one order of magnitude smaller at $\alpha = 8.9^\circ$).

3.1.2 MiTE Effects

A series of experiments was conducted to assess the influence that the MiTEs have upon the wing. For all of the configurations examined, all MiTEs in the down position formed a

Table 3.1. Comparison of measured section lift and drag coefficients to tabulated data.

α	Current Experiment		Jacobs and Sherman (1937)	
	C_l	C_d	C_l	C_d
3	0.273	0.014	0.31	0.0100
6	0.536	0.044	0.55	0.0124
8.9	0.763	0.086	0.76	0.0182

Fig. 3.1. The spanwise lift distribution for the clean wing at three angles of attack. The uncertainty in C_l is smaller than the symbol size.

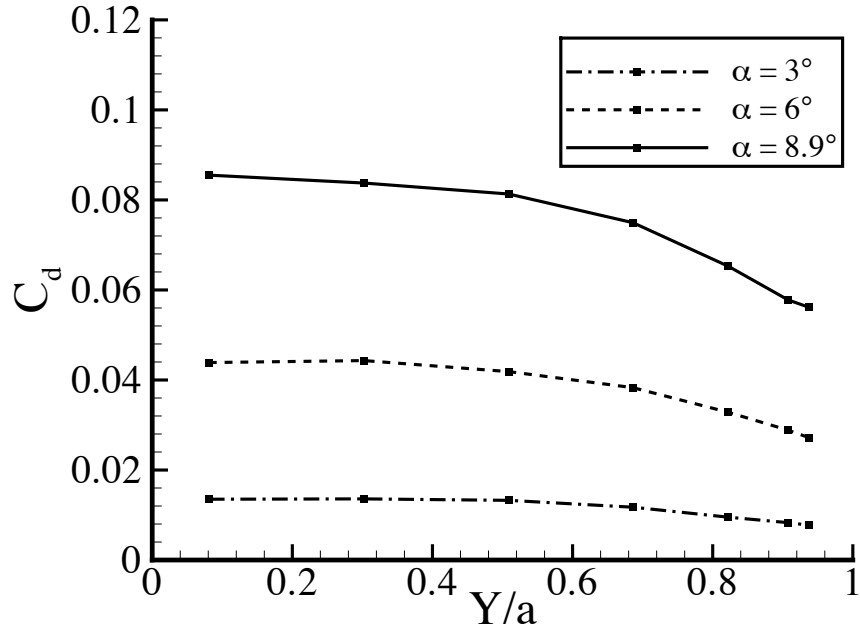


Fig. 3.2. The spanwise drag distribution for the clean wing at three angles of attack. The uncertainty in C_d is smaller than the symbol size.

continuous group, i.e., no down MiTEs were ever separated by neutral ones. We varied both the spanwise fraction of down MiTEs, a_{down}/a , and the nondimensional spanwise centroid of down MiTEs, Y_{flap}/a .

Figure 3.3 is a plot of the pressure coefficient along the chord at the spanwise location closest to the root ($Y/a = 0.081$) where the flow was essentially two-dimensional. Both the neutral case ($a_{down}/a = 0$) and full span down case ($a_{down}/a = 0.865$, $Y_{flap}/a = 0.487$) are shown. It was apparent that the effect of the MiTEs was felt along the entire chord line on both the pressure and suction sides of the wing. This was consistent with previous research (Giguère et al. 1995; Jeffrey and Hurst 1996). Gurney flaps, or in our case, MiTEs, altered the effective shape of the wing in a way that increased the circulation generated about the airfoil section. The additional circulation effected an increase in lift that was distributed chordwise along the entire airfoil. The MiTEs did not bear very much of the additional load by themselves, which was an advantageous feature that helped to mitigate any increase in pitching moment they might have caused.

For the full span down case, the total lift produced by the wing was increased by 12.3%. The effect upon the pressure coefficient at each spanwise location was analogous to the

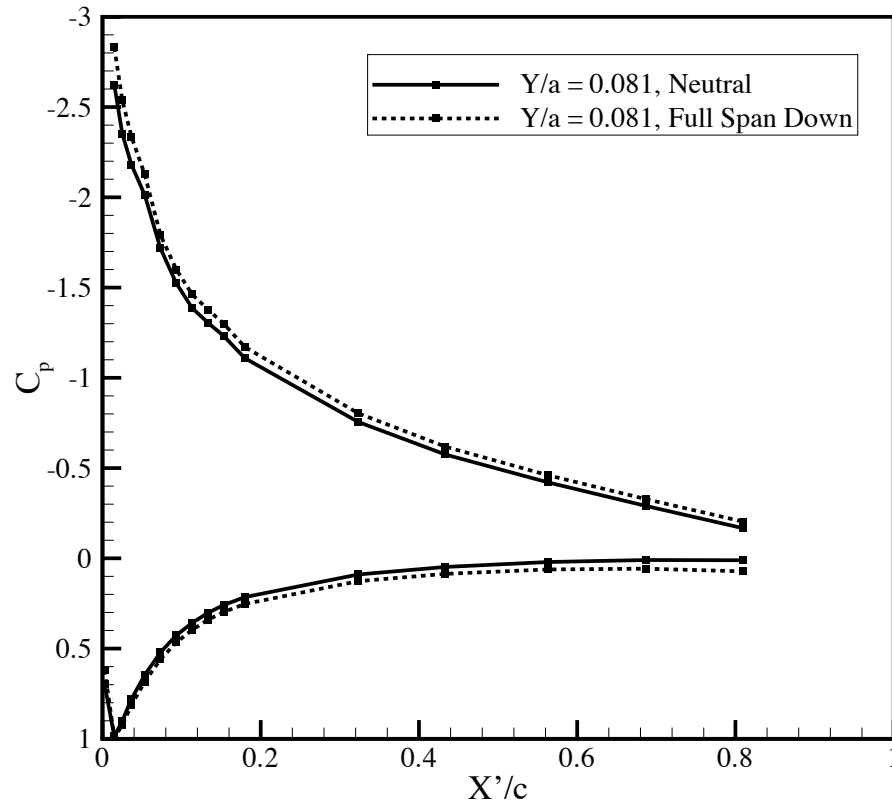


Fig. 3.3. The streamwise pressure coefficient distribution at the spanwise station closest to the root ($Y/a = 0.081$) for the neutral case ($a_{down}/a = 0$) and the full span down case ($a_{down}/a = 0.865$, $Y_{flap}/a = 0.487$). The uncertainty in C_p is smaller than the symbol size.

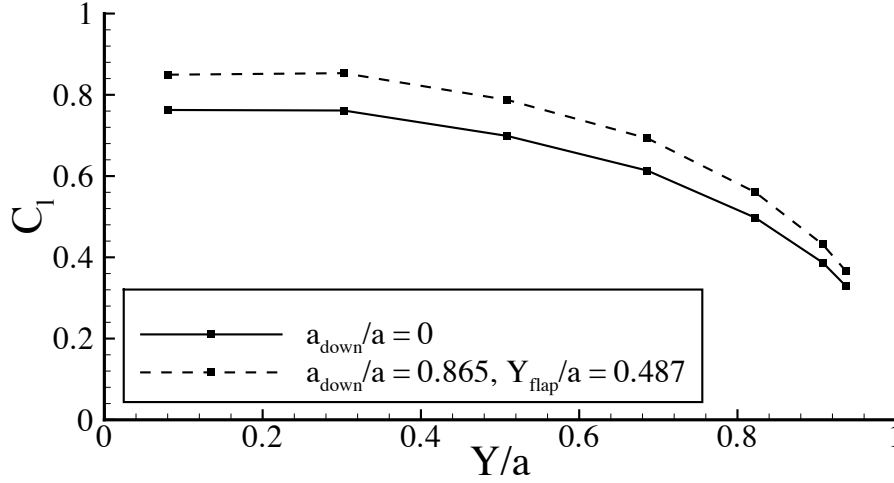


Fig. 3.4. Spanwise loading distributions for the neutral and full span down cases. The uncertainty in C_l is smaller than the symbol size.

location shown in Fig. 3.3. Spanwise loading distributions for the neutral and full span down cases are shown in Fig. 3.4. The increment in section lift coefficient caused by the MiTEs was not a constant across the span, but instead, the increase in C_l was always a fraction between 11.2% and 13.0% of the neutral case C_l . This became an important consideration for designing an active flow control scheme that aimed to conserve total lift.

In Fig. 3.5, we plot the spanwise drag distribution for the same two cases. The MiTEs clearly caused a small increase in drag. This drag increment, however, was 12 times smaller than the lift increment, and was due to the change in the effective shape of the airfoil as well as the lift increase which resulted in more induced drag.

We considered several other MiTE actuation configurations whose loading distributions are shown in Figs. 3.6 and 3.7. First, we considered several configurations where a_{down}/a was relatively large. In Fig. 3.6a, we divided the wing roughly into two halves where one half was held in the down position, and the other was in the neutral position (amounts were not at even fractions due to the discrete locations of the flaps). When the root half was in the down position ($Y_{\text{flap}}/a = 0.253$), the portion of the lift curve towards the root experienced the greatest increment in lift, and as we moved towards the tip, the effect faded away. Note that the effect was still felt at the spanwise station closest to the tip, but it was significantly smaller. For the case where the tip half of the wing was in the down position ($Y_{\text{flap}}/a = 0.687$), we saw the same effect in reverse. In this configuration, the lift increment

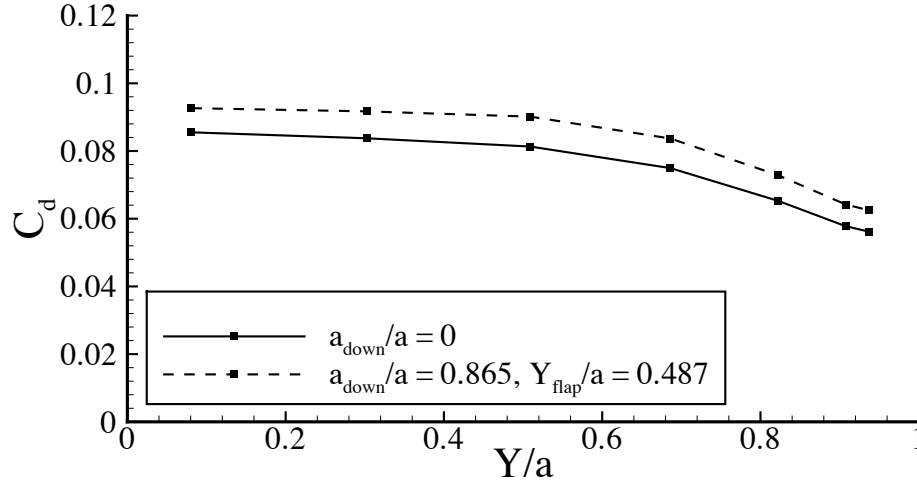


Fig. 3.5. Spanwise drag distributions for the neutral and full span down cases. The uncertainty in C_d is smaller than the symbol size.

was greatest at the tip and decreased towards the root. We found also that superposing the increments measured in these two cases produced the same increment as in the full span down case to within 0.45% of the full span down distribution.

Figure 3.6b shows similar results, this time dividing the wing roughly into thirds. Again, the effect was concentrated at the spanwise location of the down MiTEs, and the superposition of these three increments nearly exactly produced the full span down increment.

This apparent quasi-linearity in the flap effectiveness has been noted by other researchers (Solovitz and Eaton 2004b; Myose et al. 1998; van Dam and Yen 1999). The important point to note regarding these large a_{down}/a cases is that the increment in lift coefficient caused by the MiTEs was a function of both the amount of span that was actuated as well as the location of the actuated span.

In Fig. 3.7, we show the influence upon the spanwise loading distribution for three cases where only four flaps were in the down position ($a_{down}/a = 0.13$). These were the locations most likely to be used for vortex control applications. We only considered values of Y_{flap}/a near the tip, and pressure data were not taken at the two spanwise stations closest to the root. We saw the same basic trend that we noted in the previous cases. The $Y_{flap}/a = 0.654$ case caused the largest root increment (amongst these three cases), while the $Y_{flap}/a = 0.854$ case caused the largest increment near the tip.

Table 3.2 shows the change in total lift for each configuration as a percentage of the

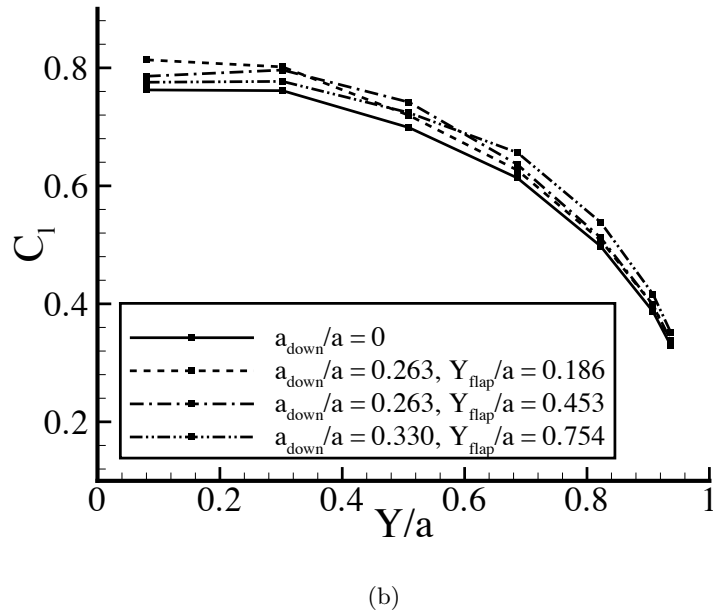
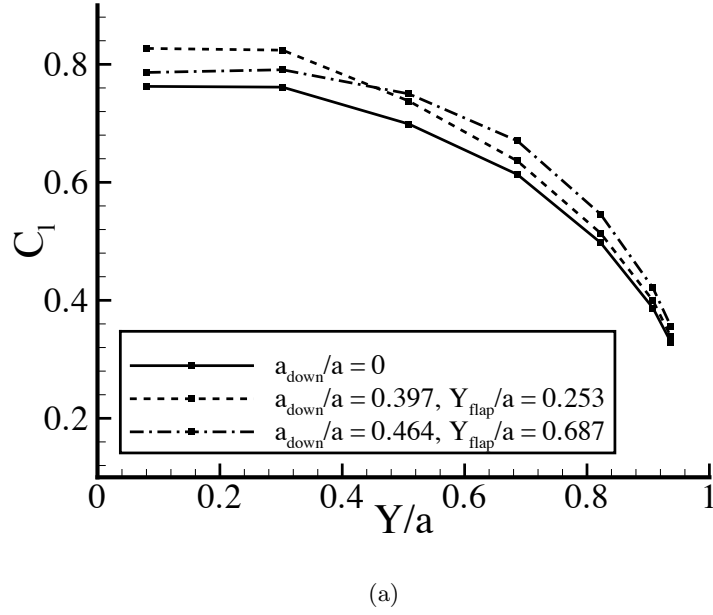


Fig. 3.6. Spanwise loading distributions for the neutral case and cases that divide the wing in two halves (a), and into three thirds (b). The uncertainty in C_l is less than or equal to the symbol size.

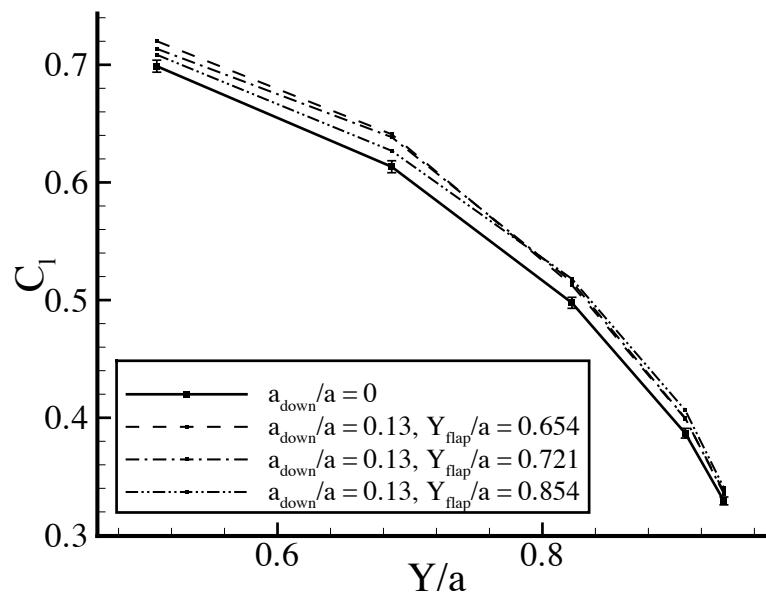


Fig. 3.7. Spanwise loading distribution near the tip for cases that nearly conserve lift. The uncertainty bars shown on the neutral case apply to all cases at each spanwise location.

Table 3.2. Increment in lift compared to the neutral case.

a_{down}/a	Y_{flap}/a	$\Delta C_L/C_L$
0.865	0.487	+12.30%
0.397	0.253	+6.12%
0.464	0.687	+6.32%
0.263	0.186	+3.96%
0.263	0.453	+4.34%
0.330	0.754	+4.09%
0.13	0.654	+3.62%
0.13	0.721	+3.35%
0.13	0.854	+2.71%

neutral case total lift. Note that only locations where data were available were integrated. This may slightly overestimate the lift increments for $a_{down}/a = 0.13$ cases. Although the effect upon the total lift was not negligible, it was quite small. More importantly, the maximum difference in lift between the small a_{down}/a configurations was only 0.91%. Thus, an active flow control scheme that involved cycling between these static configurations would conserve the total lift on the wing rather well.

3.2 Near Wake Flow Structure

3.2.1 Mean Flow Field Modification

Having determined the influence that the MiTEs had on the wing characteristics, we proceeded to examine their effect on the trailing vortex rollup process. For presenting wake data, we used the coordinate system shown in Fig. 3.8. The origin of this tunnel coordinate system was at the root trailing edge of the wing when the wing was at a 0° angle of attack. X was the streamwise direction, Y was the spanwise direction, and Z was the lift direction. The $Z = 0$ plane ran directly down the middle of the tunnel.

We began with an investigation of the flow field immediately downstream of the wing at $X/c = 0.20$. Five-hole probe experiments were performed at low resolution (12.5 mm

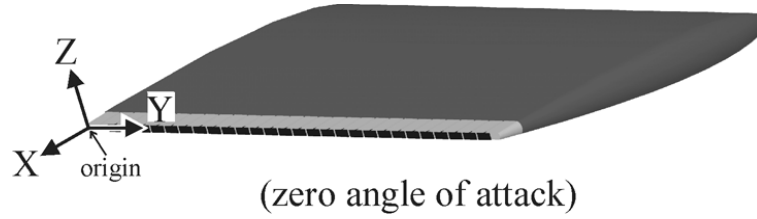


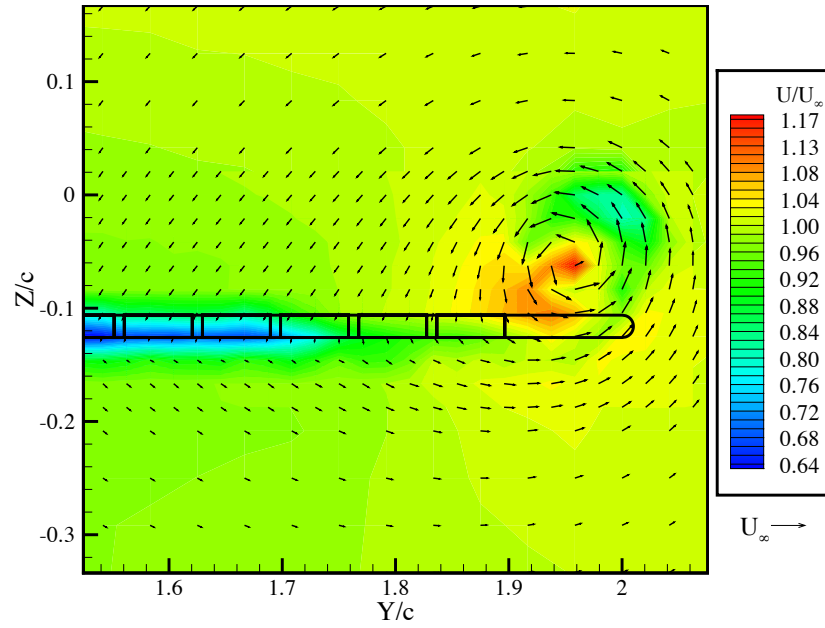
Fig. 3.8. The tunnel coordinate system used to present wake data.

spacing) over a large domain, then runs at twice the resolution (6.25 mm spacing) were performed in smaller regions within this large domain. In the figures that follow, we show both the low and high resolution data with the high resolution data overlaid. Also, an outline of the trailing edge geometry projected into the measurement plane is given to illustrate the location of the wing and positions of the MiTEs.

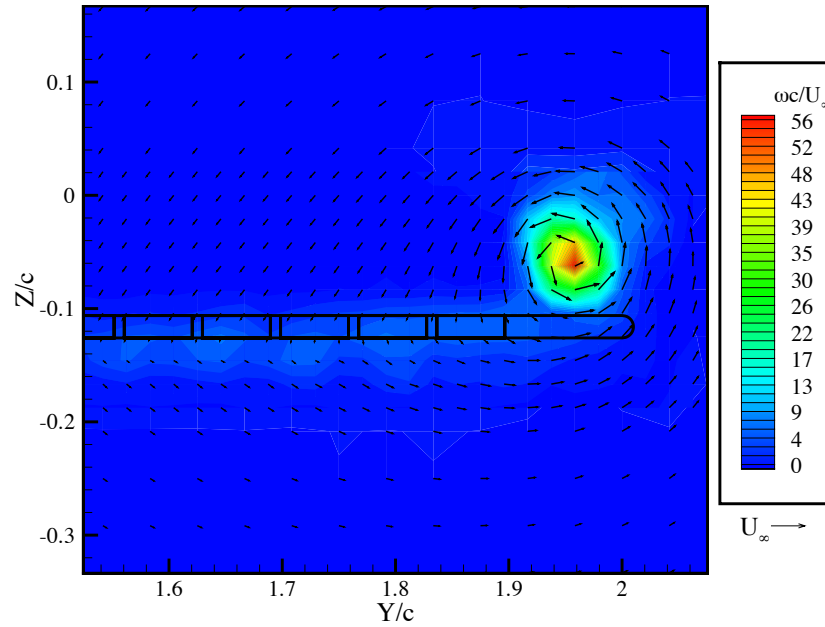
Figure 3.9 shows the velocity and vorticity fields for the neutral case. The flow is going outboard on the pressure side and inboard on the suction side causing the trailing vortex to form just above and inboard of the tip trailing edge. The tip vortex was in the early stages of the rollup process as expected and did not display the circumferential symmetry we would expect after rollup. We also noted a 17% excess in streamwise velocity above the freestream near the center of the vortex. An excess velocity was seen also in the work of Chow (1997). We noted a region of velocity deficit due to the drag on the wing inboard of $Y/c = 1.72$ and in line with the trailing edge.

We compared this case to the full span down case which is shown in Fig. 3.10. The flaps produced several notable features. First, there was intensification of tangential and streamwise velocity components. This was a result of the additional circulation created by the MiTEs shown earlier in the loading distributions. Also, we found that each flap created a small patch of velocity deficit. The velocity deficit was accompanied by an increase in downwash and streamwise vorticity. Each patch occurred immediately behind a flap, then was displaced by the strong tangential (V, W) components of the mean flow as it traveled downstream. Once we arrived at the measurement plane, the patches were no longer located immediately behind their corresponding flaps.

To confirm this, we considered another MiTE configuration, one with only the four flaps closest to the tip in the down position ($a_{down}/a = 0.13$, $Y_{flap}/a = 0.788$). This is shown in Fig. 3.11. Again, we saw velocity deficit patches due to the down flaps. The two flaps closest to the tip were in the neutral position, and as a result, two of the patches that were

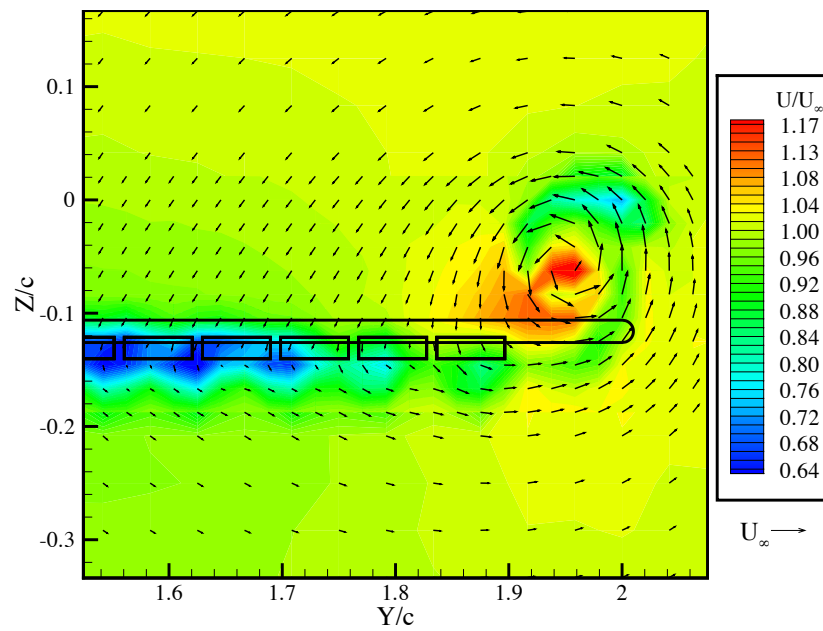


(a) Velocity Field

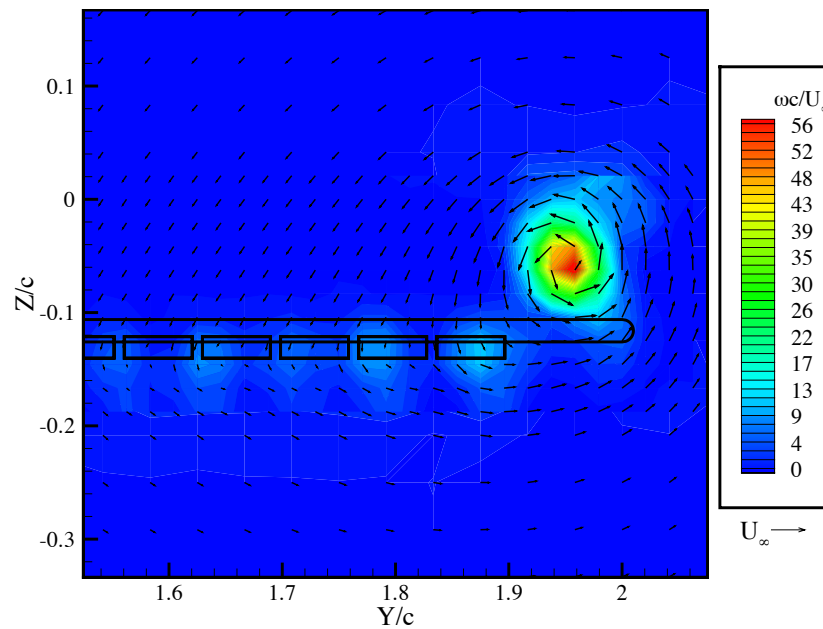


(b) Vorticity Field

Fig. 3.9. Contours of streamwise velocity and vorticity with tangential velocity vectors superimposed for the neutral case at $X/c = 0.20$.



(a) Velocity field



(b) Vorticity field

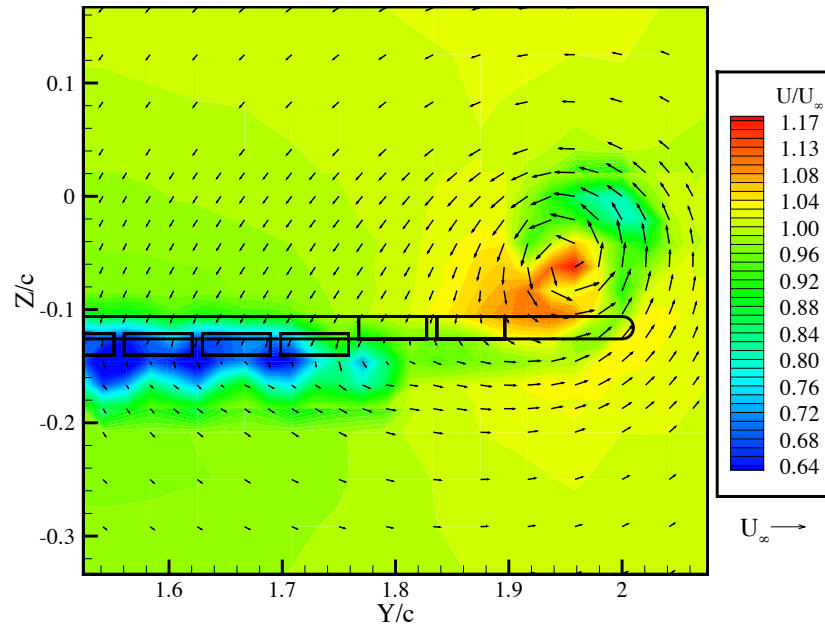
Fig. 3.10. Contours of streamwise velocity and vorticity with tangential velocity vectors superimposed for the full span down case at $X/c = 0.20$.

present for the full span down case are missing in this case. We can, thus, confirm the origin of each patch. In Fig. 3.12 we examine the flow for the same case but further downstream at $X/c = 0.83$. As the vortex continued to rollup, the patches diffused into one another as they were continually advected by the strong tangential velocities.

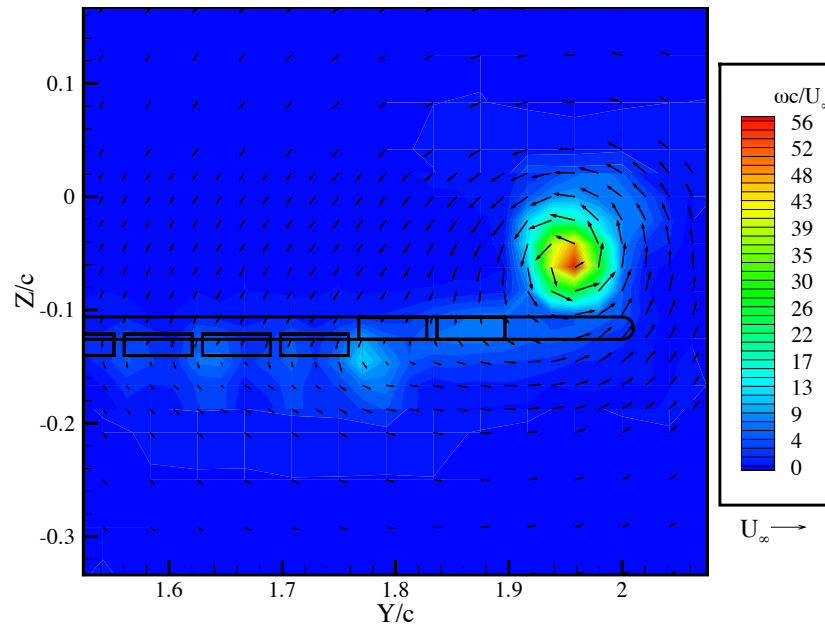
The most important aspect of the mean flow modification with regard to developing a wake alleviation strategy is demonstrated in Fig. 3.13a. We took the velocity field for the $a_{down}/a = 0.13$, $Y_{flap}/a = 0.788$ case examined above, and subtracted from it the velocity field of the neutral case, thus, highlighting the change in the flow field caused by the flaps. A close examination of the center location of the tip vortex in this plot demonstrated that at 0.2 chord lengths behind the wing, the flaps had done very little to displace the vortex in the lift or spanwise direction. Had the position of the vortex changed significantly, there would be a very clear doublet vector pattern in the velocity difference field near the vortex location. This demonstrated that the flaps did not significantly change the origin of the vortex. Thus, we confirmed that unlike many other active flow control techniques, the changes to the flow caused by the MiTEs were not due to modification of any unstable aspects of the flow such as streamwise or spanwise separation. Rather, the MiTEs made changes to the vorticity distribution immediately behind the wing. We examined the velocity difference field further downstream at $X/c = 0.83$ in Fig. 3.13b. There, we saw a clear doublet pattern indicating that at this streamwise station, the vortex has been displaced. The MiTE effects were being felt by the vortex more and more as it continued to roll up.

3.2.2 Secondary Structures

In other research on partial-span Gurney flaps, it has been hypothesized that because of the additional lift that these flaps create, they also create discrete secondary vortices at their tips. To our knowledge, no previous work has shown measurements of these structures. In Fig. 3.13a, we observe a circulating flow about the outboard edge of the down flaps. The rotationality of this vortex is the same as that of the primary tip vortex, which is expected. At $X/c = 0.83$ (Fig. 3.13b), we could clearly see that this structure had advected down and outboard with the tangential flow. Thus, we had observed what seems to be a co-rotating secondary vortex originating at the outboard edge of a set of down MiTEs. The inboard edge of the down flaps likely also creates a vortex which is counter-rotating with respect to the primary tip vortex, but since the measurement domain did not extend this far inboard, we could not observe it with this MiTE configuration.

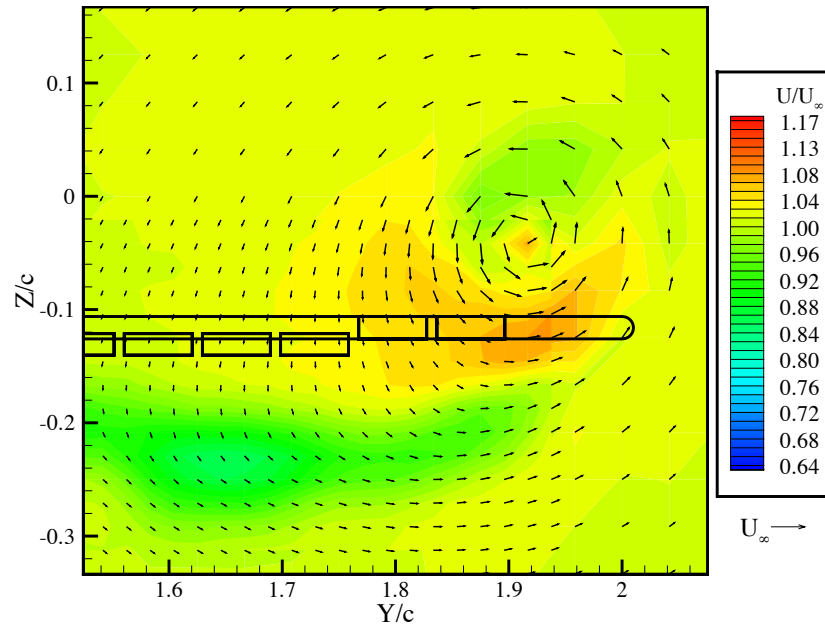


(a) Velocity field

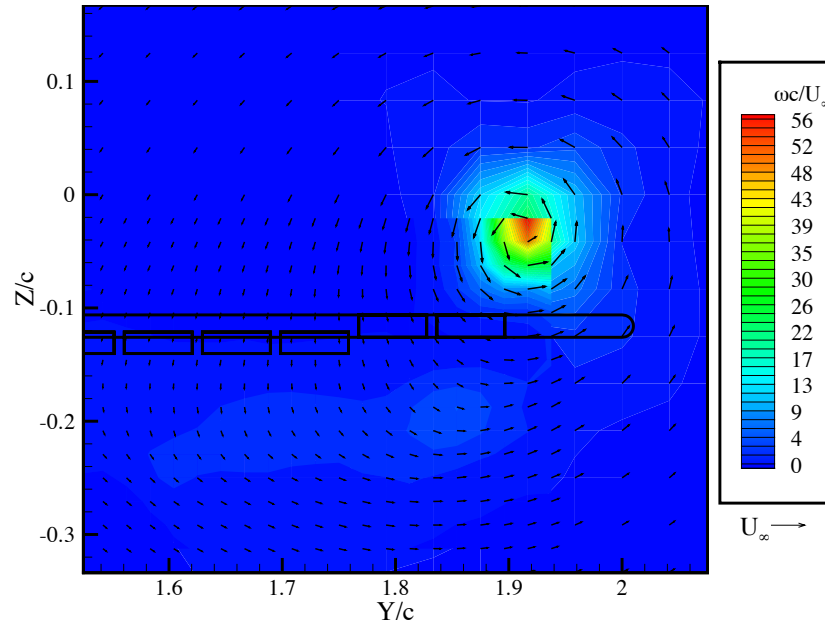


(b) Vorticity field

Fig. 3.11. Contours of streamwise velocity and vorticity with tangential velocity vectors superimposed for $a_{down}/a = 0.13$, $Y_{flap}/a = 0.788$ at $X/c = 0.20$.

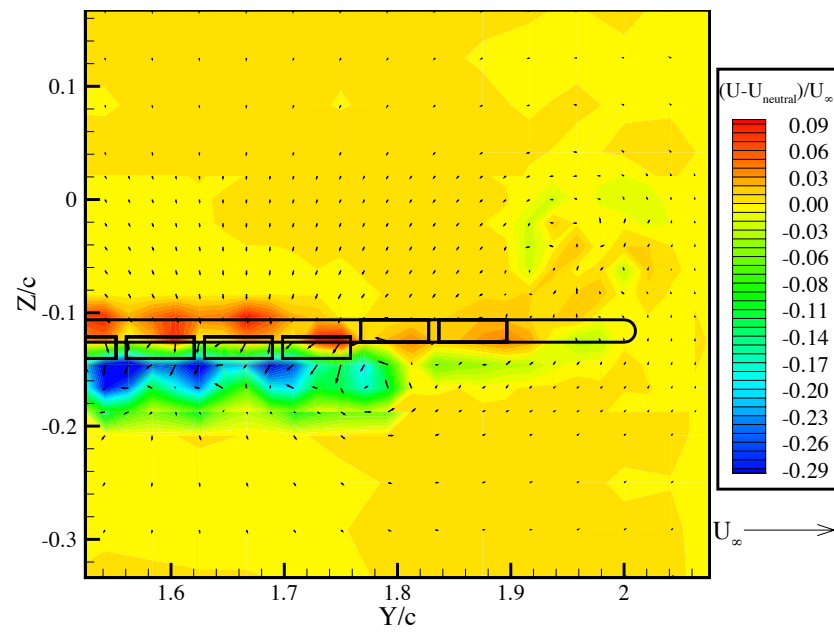
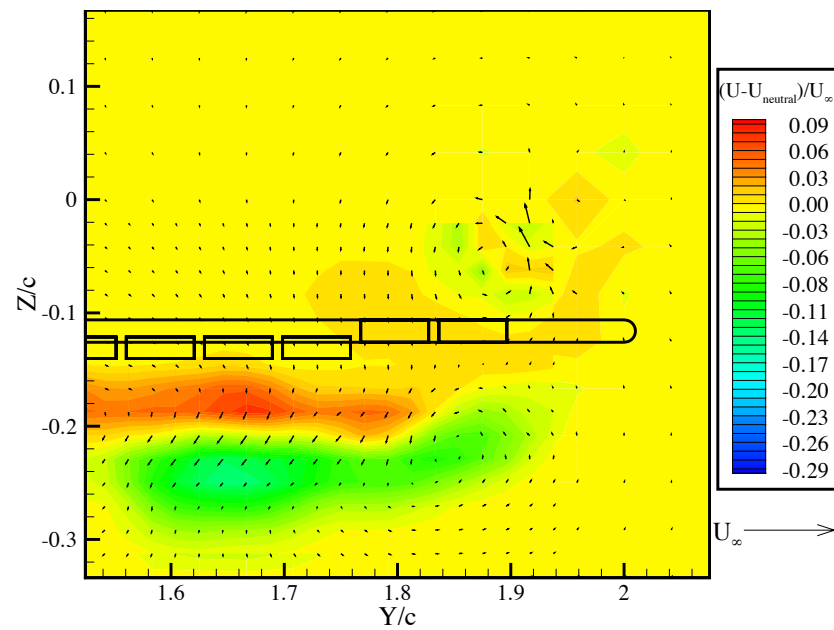


(a) Velocity field



(b) Vorticity field

Fig. 3.12. Contours of streamwise velocity and vorticity with tangential velocity vectors superimposed for $a_{down}/a = 0.13$, $Y_{flap}/a = 0.788$ at $X/c = 0.83$.

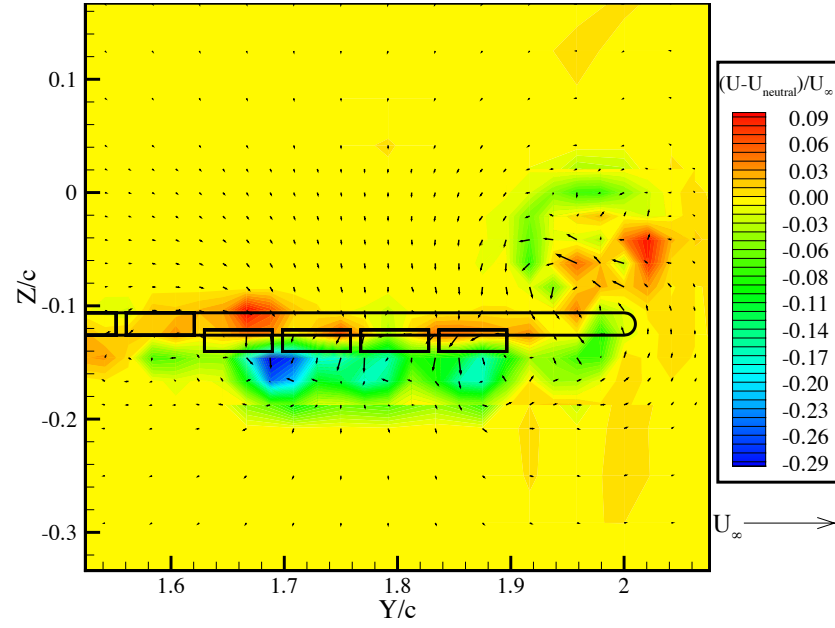
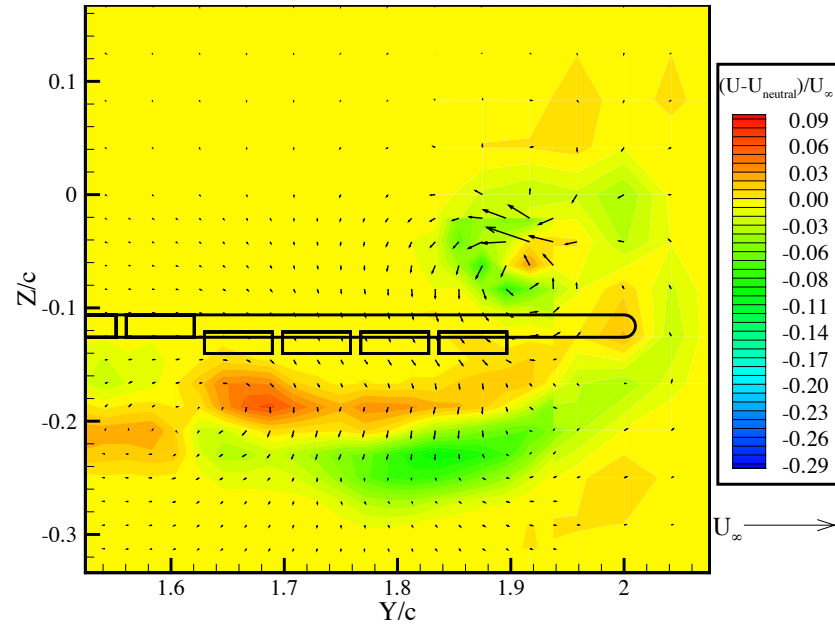
(a) $X/c = 0.20$ (b) $X/c = 0.83$ Fig. 3.13. The velocity difference field for $a_{\text{down}}/a = 0.13$, $Y_{\text{flap}}/a = 0.788$.

To observe a counter-rotating secondary vortex, we considered another MiTE configuration where the four flaps closest to the tip were in the down position ($a_{down}/a = 0.13$, $Y_{flap}/a = 0.854$). There, the inboard edge of the down MiTEs was well inside the measurement domain. This case is shown in Fig. 3.14. At $X/c = 0.20$, near the inboard edge of the down MiTEs, the counter-rotating secondary vortex is difficult to observe, however, at $X/c = 0.83$, the structure has moved downward and has become much clearer. Thus, we have confirmed the existence of both co-rotating and counter-rotating secondary vortices associated with partial-span Gurney flaps, or in our case, static MiTEs.

3.3 Intermediate Wake Steady-State Measurements

In the intermediate wake, the vortex has almost completely rolled up. Five-hole probe and static PIV measurements were made there in order to assess the steady-state wake effects associated with MiTE actuation. The high resolution achieved by the PIV measurements allowed us to accurately locate the center of the vortex. The five-hole probe measurements, on the other hand, were taken with coarser resolution in order to efficiently examine a much larger domain. Figure 3.15 shows one instantaneous velocity and vorticity field from a typical PIV data set, and Fig. 3.16 shows the velocity and vorticity field of 500 ensemble averaged PIV image pairs. Both were for the neutral case at $X/c = 4.9$. For visual clarity, every other vector in both directions was removed. The fingering that was apparent in the mean velocity field was the result of some slight integer peak-locking which the sub-pixel accuracy equalization technique did not remove.

To establish a baseline, we first examined the PIV results for the full span down case ($a_{down}/a = 0.865$, $Y_{flap}/a = 0.487$) and compared them to the neutral case. Figure 3.17 shows the streamwise evolution of the mean tangential velocity magnitude field for the neutral and full span down cases measured using PIV. Each field shown is the ensemble averaged result from 500 image pairs. For the full span down case at all three streamwise positions (Fig. 3.17b,d,f), peak tangential velocities in the vortex were increased by roughly 3-4%. Also, in both cases we noted a slight circumferential asymmetry in the velocity field, but this was merely because the vortex was still moving slightly in the YZ plane. This resulted in a larger velocity magnitude at certain angular locations about the vortex center. We noted also that the MiTEs clearly shifted the vortex center location at all streamwise positions.

(a) $X/c = 0.20$ (b) $X/c = 0.83$ Fig. 3.14. The velocity difference fields for $a_{\text{down}}/a = 0.13$, $Y_{\text{flap}}/a = 0.854$.

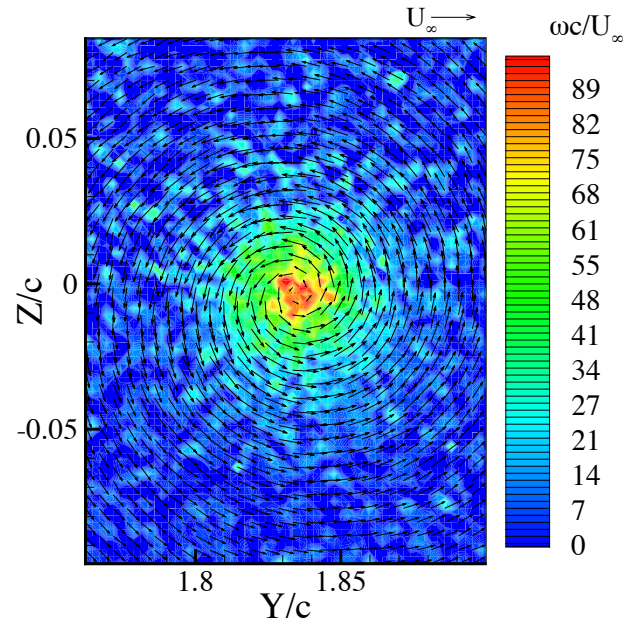


Fig. 3.15. Instantaneous velocity and vorticity fields for the neutral case at $X/c = 4.9$. Every other vector is removed for visual clarity.

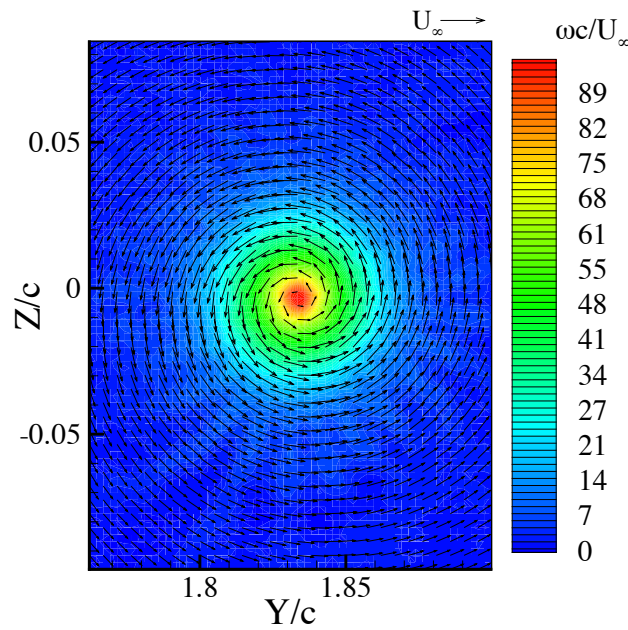


Fig. 3.16. Ensemble averaged velocity and vorticity fields for the neutral case at $X/c = 4.9$. Every other vector is removed for visual clarity.

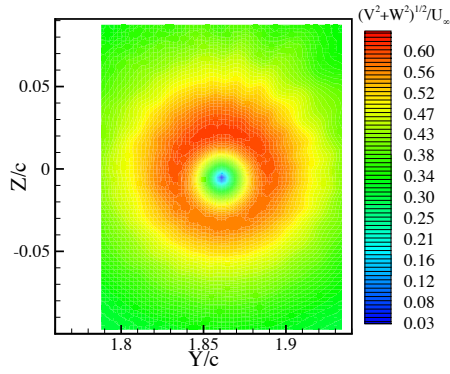
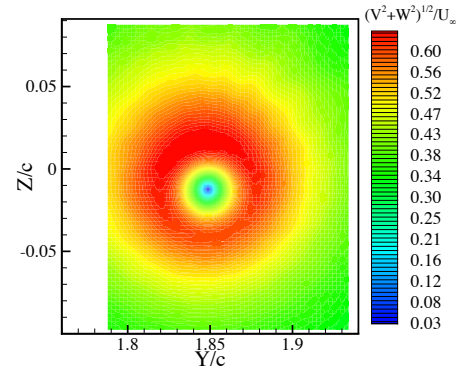
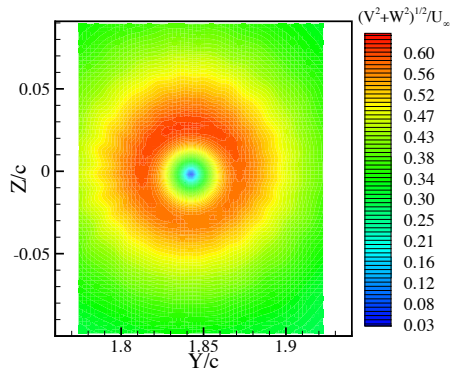
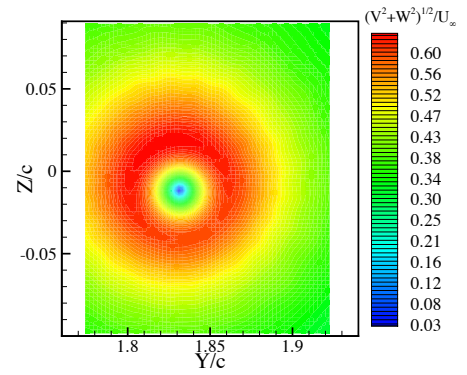
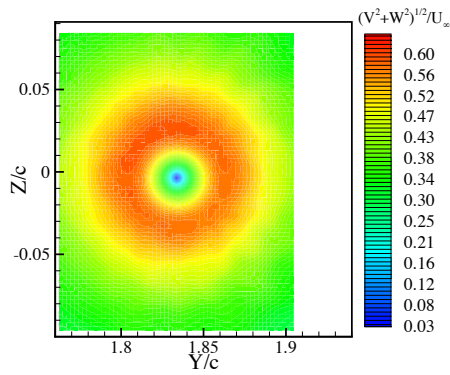
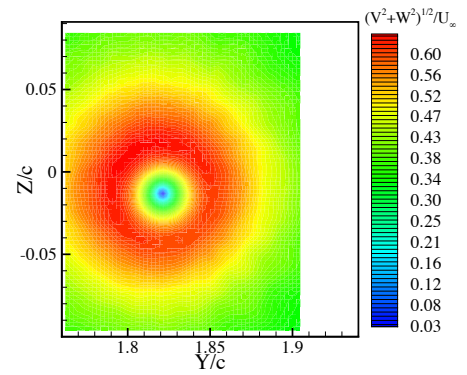
(a) Neutral, $X/c = 2.8$ (b) Full span down, $X/c = 2.8$ (c) Neutral, $X/c = 3.8$ (d) Full span down, $X/c = 3.8$ (e) Neutral, $X/c = 4.9$ (f) Full span down, $X/c = 4.9$

Fig. 3.17. Nondimensional velocity contours for the neutral and full span down cases.

To examine these two cases more carefully, Fig. 3.18 gives the spanwise velocity and vorticity profiles across the center of the vortex. Here, we employed a center averaging technique in order to remove the effects of vortex wandering. For each instantaneous velocity field, the vortex center was located by finding the point of lowest tangential velocity magnitude. Then, all of the vector fields were aligned along their individual centers, and ensemble averaged. The $(\Delta Y, \Delta Z)$ origin of this vortex centered coordinate system follows the center of the neutral case vortex. The results in Fig. 3.18 are plotted in this coordinate system, however, one slight change is made. The vortex for the full span down case, in reality, is not centered at the same location as the neutral case vortex. In order to make it easier to compare the velocity and vorticity profiles, we have moved the center of the vortex in the full span down case to coincide with the neutral case vortex.

We see in Fig. 3.18 that in addition to the increment in peak velocities, the peak vorticities were also increased here by roughly 11% with respect to the neutral case. For this case, we saw in the previous section that the MiTEs increment the spanwise loading distribution across the entire span, including near the root. According to lifting line theory, the amount of circulation that is left in the wake of a wing is equal to the circulation at the root. Thus, it was not surprising that we saw this increment in vorticity. Note also that as we moved downstream, the vorticity peaks for both cases were falling as the vorticity in the core diffused radially.

We then considered the same two cases measured over a much larger domain using a five-hole probe. Figure 3.19 compares the velocity profiles for the full span down and neutral cases (as with the PIV). Since these data are also presented in our vortex centered coordinate system, interpolation was used to line up the data points on a common origin. This interpolation led to large errors in regions of high velocity gradients, thus, data points near the core were omitted. Clearly, intensification in tangential velocity occurred over this larger domain just as it did in the PIV results. This further demonstrated that MiTEs, when in the full span down configuration, increased the circulation about the wing. This also showed that the effect of the MiTEs could be felt in both the highly rotational region of the vortex (as in the PIV), as well as in the region further from the center, where vorticity levels were much lower.

For the large a_{down}/a cases, aside from the increment in the vorticity profile and tangential velocity, several characteristics of the vortex were essentially unchanged. Firstly, although not shown explicitly here, the five-hole probe measurements demonstrated that

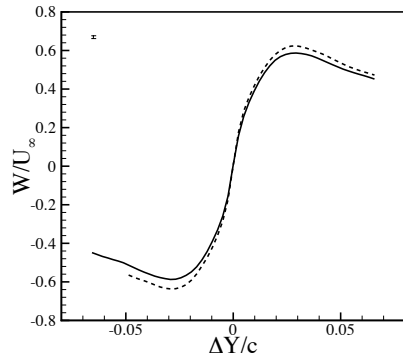
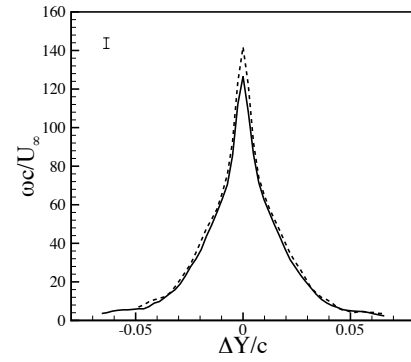
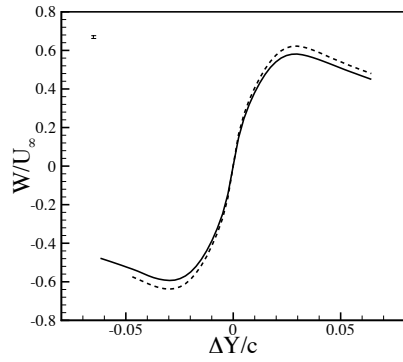
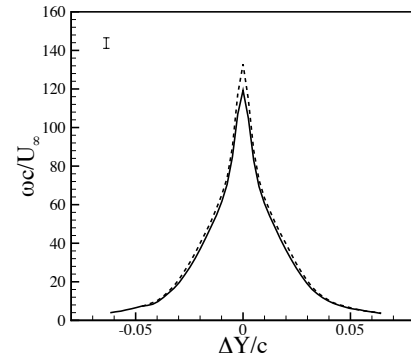
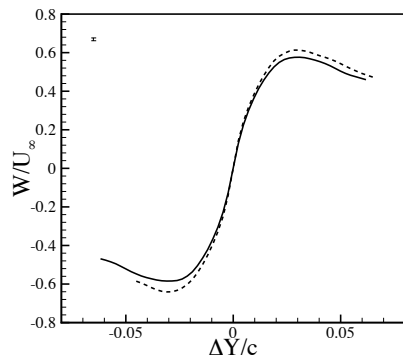
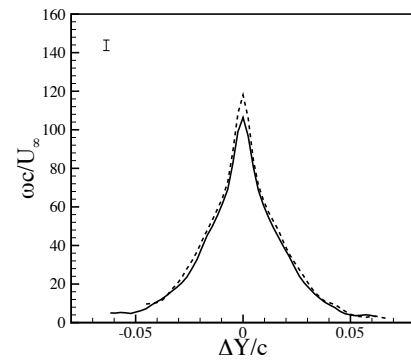
(a) $X/c = 2.8$ (b) $X/c = 2.8$ (c) $X/c = 3.8$ (d) $X/c = 3.8$ (e) $X/c = 4.9$ (f) $X/c = 4.9$

Fig. 3.18. Nondimensional velocity and vorticity profiles plotted in vortex centered coordinate system using center averaging technique for the neutral case (solid line) and the full span down case (dotted line). The uncertainty is indicated by the bar shown in the top left corner of each plot.

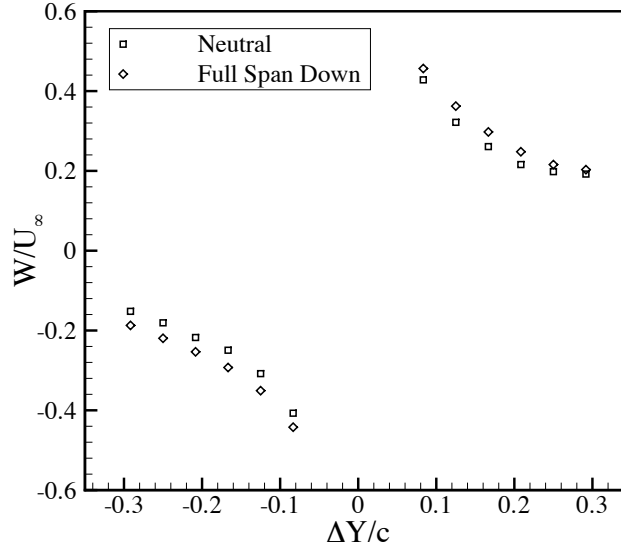


Fig. 3.19. Nondimensional velocity profiles from five-hole probe measurements plotted in vortex centered coordinate system for neutral and full span down cases. The uncertainty is smaller than the symbol size.

the streamwise velocity in the vortex was essentially uniform to within roughly $\pm 4\%$ for all cases. Secondly, from the PIV, we saw that the core was no more and no less diffuse for either configuration, i.e., the vortex was equally coherent in both cases. Finally, the standard deviation of the instantaneous vortex center location from one image pair to another was comparable, i.e., the amount of vortex wandering never measurably changed.

Moving on to other flap configurations, in Figs. 3.20 and 3.21 we show the tangential velocity magnitude contours for three small actuation ratio configurations where $a_{down}/a = 0.13$. Comparing these contours with those of the neutral case, it was qualitatively clear that the tangential velocities in the vortex core were largely unaffected by the MiTEs (apart from shifting the center location). In Fig. 3.22, we show the velocity profiles from the neutral case and the same three small actuation ratio configurations at $X/c = 4.9$ over a much larger domain (from five-hole probe measurements). Although there were some observable differences between the velocity profiles, the changes were quite small. This was not surprising given the small changes in the spanwise loading distribution shown in the previous section.

Thus, for all a_{down}/a and Y_{flap}/a values examined, there was no change in how diffuse or concentrated the vortex was, or how much it wandered. Large a_{down}/a cases served only

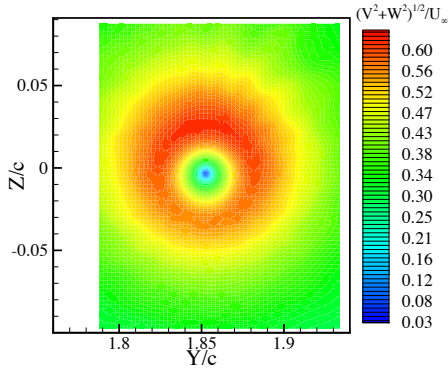
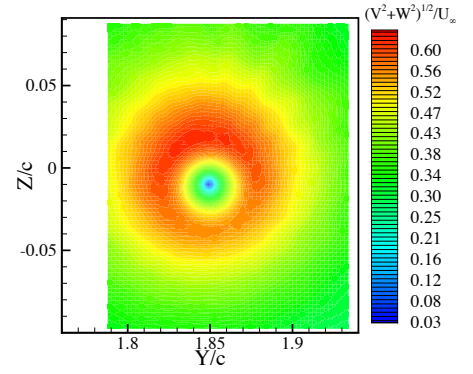
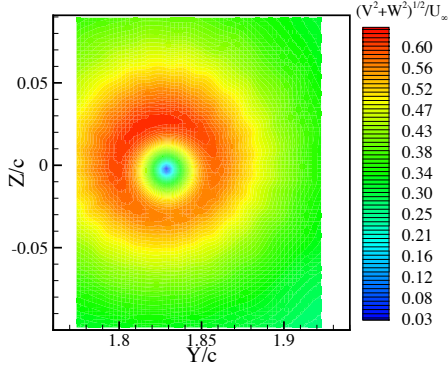
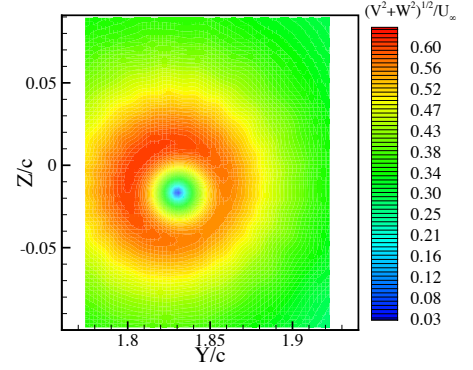
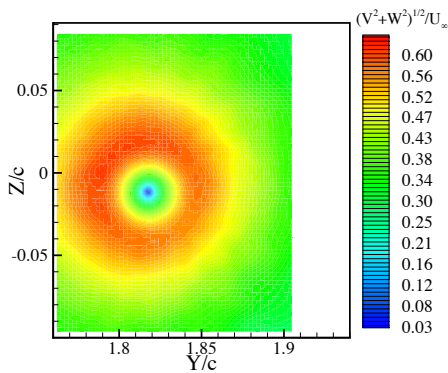
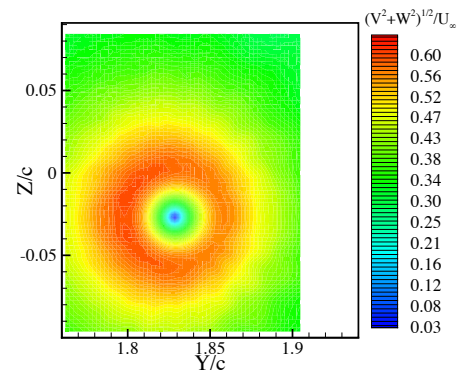
(a) $Y_{flap}/a = 0.654$, $X/c = 2.8$ (b) $Y_{flap}/a = 0.721$, $X/c = 2.8$ (c) $Y_{flap}/a = 0.654$, $X/c = 3.8$ (d) $Y_{flap}/a = 0.721$, $X/c = 3.8$ (e) $Y_{flap}/a = 0.654$, $X/c = 4.9$ (f) $Y_{flap}/a = 0.721$, $X/c = 4.9$

Fig. 3.20. Nondimensional velocity contours for small actuation ratio cases where $Y_{flap}/a = 0.654$ and 0.721 .

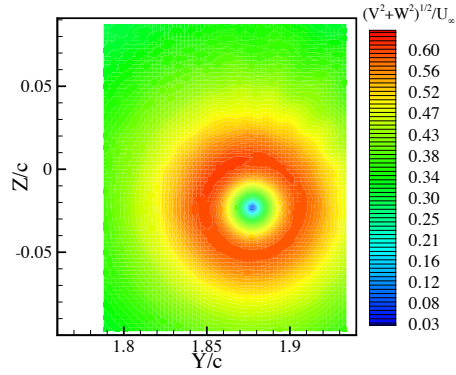
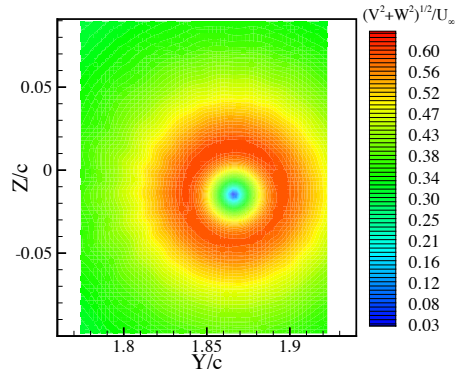
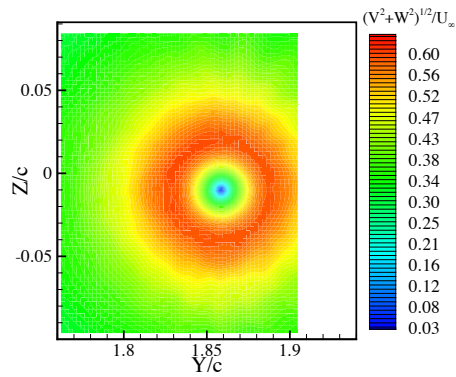
(a) $Y_{flap}/a = 0.854$, $X/c = 2.8$ (b) $Y_{flap}/a = 0.854$, $X/c = 3.8$ (c) $Y_{flap}/a = 0.854$, $X/c = 4.9$

Fig. 3.21. Nondimensional velocity contours for a small actuation ratio case where $Y_{flap}/a = 0.854$.

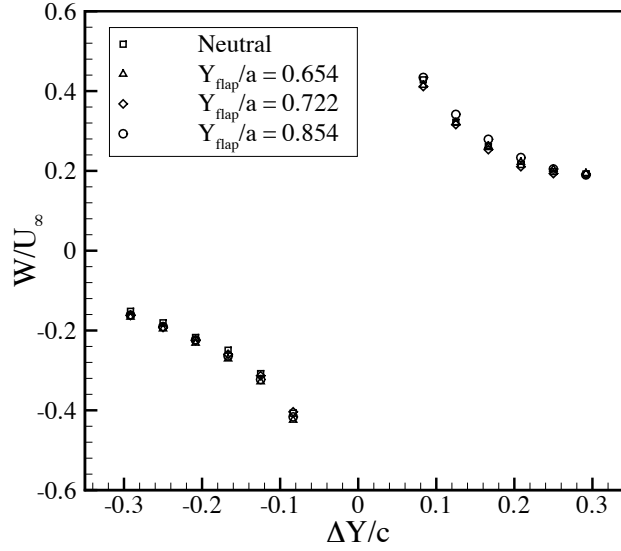
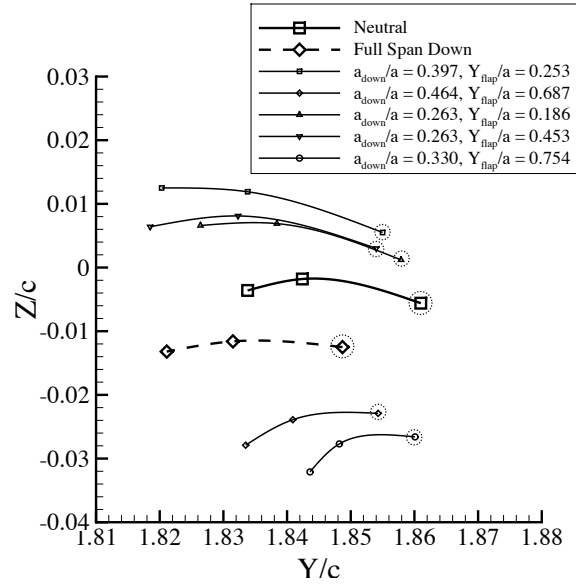


Fig. 3.22. Nondimensional velocity profiles from five-hole probe measurements plotted in vortex centered coordinate system for the neutral case and three cases where $a_{down}/a = 0.13$. The uncertainty is smaller than the symbol size.

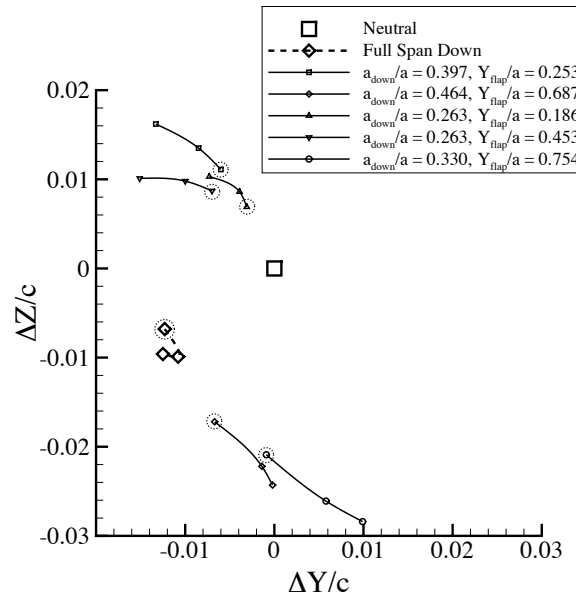
to intensify the tangential velocity and vorticity while the general shape of the profiles was essentially preserved. As mentioned before, however, for large and small actuation ratio cases, the mean location of the vortex center did change significantly, and this is central to any active wake alleviation scheme.

We began by examining the large a_{down}/a cases. The mean vortex center locations for the five large a_{down}/a cases are shown in Fig. 3.23. Results for all three streamwise locations are given on the same sets of axes, and the same data are plotted in both of the previously discussed coordinate systems. Fig. 3.23a shows the vortex center location in physical space. For all cases, the vortex was generally moving in the inboard direction although the flap configuration clearly had an effect on the trajectory. Lower values of Y_{flap}/a caused the vortex to head upward, and higher values of Y_{flap}/a caused the vortex to head downward. In Fig. 3.23b, we present the same results in the $(\Delta Y, \Delta Z)$ coordinate system. Here, we saw clearly that most of the authority we had over the vortex location was in the lift direction with respect to the neutral case vortex. The maximum lift direction displacement at $X/c = 4.9$ was downward $0.028c$, and the maximum spanwise displacement was inboard $0.015c$.

The mean vortex center locations for seven configurations with $a_{down}/a = 0.13$ are



(a) Uncentered coordinate system



(b) Centered coordinate system

Fig. 3.23. Mean vortex center locations measured by PIV for large a_{down}/a . The vortex location at $X/c = 2.8$ for each configuration is denoted by a dashed circle around the symbol. The uncertainty in both directions is indicated by the symbol size of the neutral case.

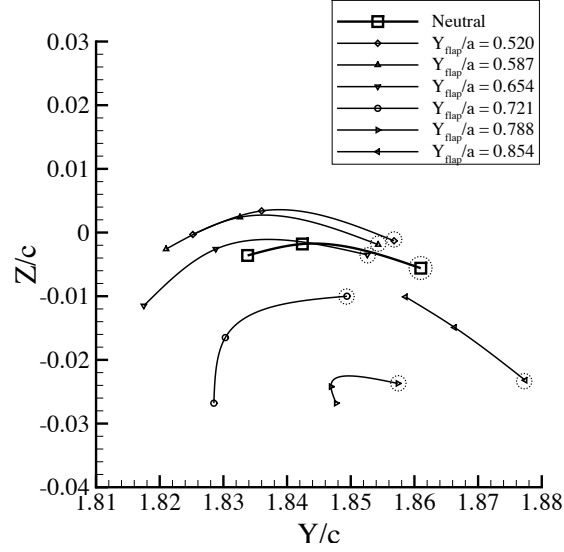
given in Fig. 3.24 in the same coordinate systems as the large a_{down}/a cases. The only difference among these configurations was that Y_{flap}/a was varied from 0.119 to 0.854. Fig. 3.24a shows that the vortex center trajectory was generally inboard for the neutral case and cases where Y_{flap}/a was less than 0.654. For the three cases where Y_{flap}/a was higher (MiTEs closer to the tip being actuated), we saw that the path of the vortex was more severely altered. In Fig. 3.24b, there is a clear pattern in the path of the vortex due to the MiTEs with respect to the neutral case vortex. As we proceeded further in the streamwise direction, we saw a counter-clockwise rotation and a radially expanding displacement. This demonstrated that the displacement of the vortex with respect to the neutral case position was growing as we proceeded further in the streamwise direction, and the distance between vortex centers for neighboring MiTE configurations was growing as well.

In terms of deflecting the vortex from its neutral case path, it was clear that the small a_{down}/a MiTE configurations had close to the same authority as the large a_{down}/a configurations. Large a_{down}/a cases produced deflections primarily in the lift direction while some small a_{down}/a cases produced large deflections in the spanwise direction. For small a_{down}/a , configurations with high Y_{flap}/a values produced large deflections, thus, they had more control authority over the vortex center position. The reason for this was likely because of the reduced spanwise influence associated with smaller a_{down}/a cases, as well as the ability to affect the loading distribution locally where its slope was most severe (near the tip). This allowed the MiTEs to have more of an impact on the center of vorticity at the wing. The maximum spanwise displacement possible between two $a_{down}/a = 0.13$ cases was $0.041c$ at $X/c = 4.9$. This was achieved by the $Y_{flap}/a = 0.654$ and $Y_{flap}/a = 0.854$ cases, for which the difference in total lift experienced by the wing was only 0.91%. Therefore, by oscillating MiTEs between these two configurations, a relatively large displacement of the vortex center could be produced with very small lift variations.

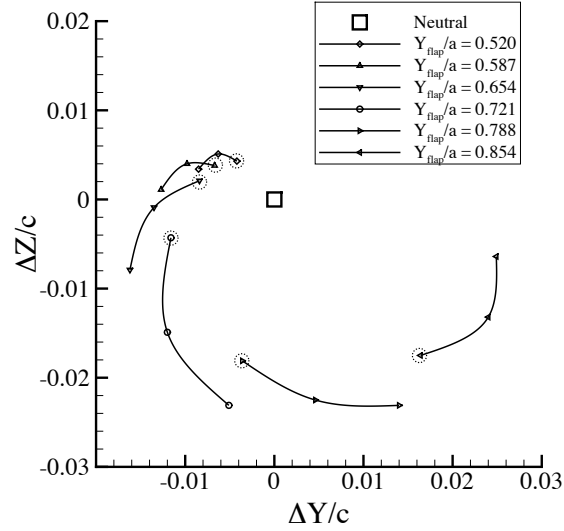
3.4 Intermediate Wake Dynamic Response

3.4.1 Active Scheme Design

All of the active wake alleviation schemes we examined consisted of cycling between two static configurations (1 and 2). In selecting which MiTE configurations to use, we began with the steady-state vortex center locations shown in Fig. 3.24. Aside from the neutral case, each configuration had four contiguous flaps in the down position ($a_{down}/a = 0.13$).



(a) Uncentered coordinate system



(b) Centered coordinate system

Fig. 3.24. Mean vortex center locations measured by PIV for cases where $a_{down}/a = 0.13$. The vortex location at $X/c = 2.8$ for each configuration is denoted by a dotted circle around the symbol. The uncertainty in both directions is indicated by the symbol size of the neutral case.

Table 3.3. Flap configurations for the three active schemes.

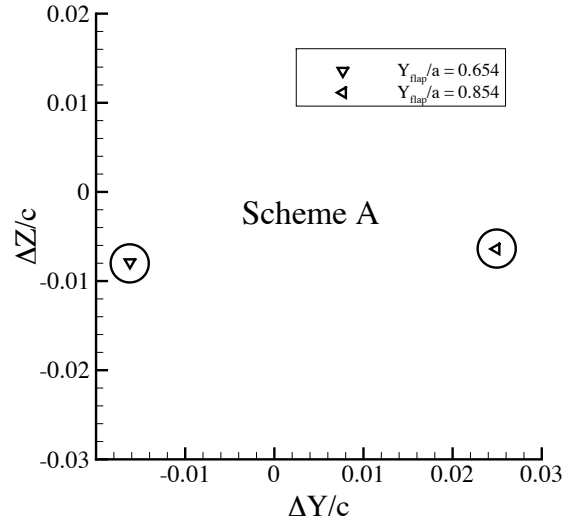
Scheme	Configuration 1	Configuration 2
simple	neutral	$Y_{flap}/a = 0.854$
A	$Y_{flap}/a = 0.654$	$Y_{flap}/a = 0.854$
B	$Y_{flap}/a = 0.721$	$Y_{flap}/a = 0.854$

We began by examining one simple actuation scheme for which configuration 1 was the neutral case and configuration 2 had the four flaps closest to the tip in the down position ($a_{down}/a = 0.13$, $Y_{flap}/a = 0.854$). This was primarily to establish a baseline. Next, since the goal was to excite vortex instability, the best active scheme would likely be one that maximized the spanwise displacement experienced by the vortex. It also may have been desirable, however, to choose a scheme in which the vortex moves in the spanwise and lift directions to resemble the most unstable eigenmode reported by Crow (1970). Thus, we examined the following active schemes: scheme A had configuration 1 as $Y_{flap}/a = 0.654$ and configuration 2 as $Y_{flap}/a = 0.854$, and scheme B had configuration 1 as $Y_{flap}/a = 0.721$ and configuration 2 as $Y_{flap}/a = 0.854$. This was summarized in Table 3.3. Transient data for schemes A and B were examined only at the furthest streamwise location ($X/c = 4.9$) since these data were used to initialize the computations. The steady-state vortex center locations for these schemes are illustrated in Fig. 3.25.

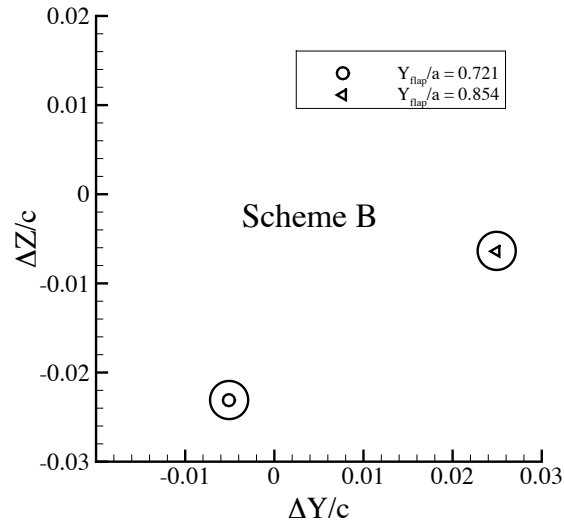
3.4.2 Vortex Transient Response

For all schemes, we used the same criterion to determine that the vortex had either begun to move or stopped moving. The earliest (in time) point to fall outside of the uncertainty ($\pm 0.001c$) with respect to all of the prior or following points was taken to indicate that the vortex had begun or ceased to move, respectively. Thus, a displacement of $0.002c$ was considered significant. We adhered strictly to this criterion in order to fairly assess vortex response times of the three schemes. Time was nondimensionalized by the flow timescale, $t_{flow} = c/U_\infty$.

The transient response of the vortex to a simple MiTE actuation scheme was studied first in order to establish a baseline and determine what aspects of the mechanical actuation



(a) Scheme A



(b) Scheme B

Fig. 3.25. Mean vortex center locations for the two active wake alleviation schemes examined.

carried over to the trailing vortex, and how they were modified in the process. For this simple scheme, configuration 1 had all MiTEs in the neutral position, and configuration 2 had the four MiTEs closest to the tip ($Y_{flap}/a = 0.854$) in the down position.

The response of the vortex for this scheme going from configuration 1 to 2 is shown in Figs. 3.26a and c, where we plot the center location of the vortex as a function of t^* at each streamwise location. Essentially every point along the transient path of the vortex lay between the two steady-state locations. Thus, there was no significant overshoot in the motion of the vortex. The nondimensional time, t^* , necessary for the vortex to move from its initial steady-state location to the next was between 3.5 and 4.2 for this scheme. These times were comparable to the longer timescales found in the mechanical response of the flaps. This suggested that the overall response of the vortex going from one steady-state location to another tended to be quasi-steady.

We turned then to the shorter timescales that were clearly present in both the mechanical and vortex responses due to the under-damping of the flap mechanism. In the earliest part of the flap mechanical response (Fig. 2.9), after receiving a signal at $t^* = 0.0$, the flap moved rapidly from the neutral position to the fully actuated position by $t^* = 1.0$. For a truly quasi-steady vortex response, we would have expected that after some time of flight, the vortex would track with the flap and move the entire distance from its initial to its final steady-state location in the same amount of time. What we see, however, is that $1.0t_{flow}$ after the vortex has started moving (at $t^* = 4.8$ for $X/c = 3.8$ in Fig. 3.26a, for example), the vortex has only moved roughly half way to the final position. There was a slight leveling off in the spanwise motion of the vortex at that time that was probably in response to the bounce in the flap motion, however, the uncertainty in the measurement prevented a definitive conclusion on this. It is clear that the vortex response to the shorter timescales of the mechanical response was not entirely quasi-steady. There was a lag time associated with the vortex response when the actuation time was less than or equal to t_{flow} .

The vortex response for this actuation scheme performed in reverse, i.e., going from configuration 2 to 1, is shown in Figs. 3.26b and d. There were some slight differences in the mechanical response (longer actuation time, different response curve) which caused some slight changes in the vortex response, but all of the observations made on the previous scheme were apparent in this one as well.

These results were consistent with previous work done on the dynamic flow response to actuators of this type. Solovitz and Eaton (2004a) studied the flow structure created by

MiTEs immediately behind the trailing edge of an airfoil in the XZ plane. They found that for relatively slow actuation times ($\Delta t^* > 1$), the dynamic flow response at the trailing edge immediately behind the MiTEs tended to be nearly quasi-steady. This was because several spanwise oriented vortices were shed at the trailing edge in the time necessary for the flap to move from one location to another. For faster actuation times ($\Delta t^* < 1$), it was found that the vortex shedding could become phase-locked with the motion of the flap, and a significant overshoot in MiTE effectiveness was observed. For the trailing vortex, when $\Delta t^* \approx 1$ we observed a response that was not quasi-steady, however, there was no overshoot. This suggested that the mechanism responsible for transient behavior in the trailing vortex was not the same as that of the immediate flap wake.

Figure 3.27 shows the vortex response at $X/c = 4.9$ for MiTE actuation schemes A and B which were described in the previous section. These schemes were more complex than the simple scheme discussed previously in that now we had a set of four flaps moving from the neutral to the down position while simultaneously, another four flaps were moving from the down to the neutral position. We began by examining scheme A, where the vortex motion was predominantly in the spanwise direction. The nondimensional time required for the vortex to get from configuration 1 to 2 was roughly 4.2, and to get from configuration 2 to 1 was roughly 4.5. Thus, even though the vortex needed to traverse almost twice as much distance as it did for the simple scheme, the response time was only slightly greater. Considering scheme B, we found that the time necessary for the vortex to get from configuration 1 to 2 was roughly 4.2, and from configuration 2 to 1 was roughly 4.8. Again, these times were only slightly longer than the response times for the simple scheme. This further suggested that the overall motion of the vortex from one steady-state location to the next tended to be quasi-steady given the mechanical response of these MiTEs. The shorter timescales in the mechanical response affected the path of the vortex, but not the overall response time.

Both the response time of the vortex to MiTE actuation as well as the path that the vortex took were critical to determining whether or not exciting vortex instability would be possible. The response time of the vortex put a finite limit on the shortest perturbation wavelength possible. The fundamental mode wavelength could be arbitrarily increased by going from configuration 1 to 2, then waiting a long time before going back to configuration 1. It could not be decreased indefinitely due to the finite response time. The path of the vortex governed the shape of the perturbation waveform. The path was never a perfect

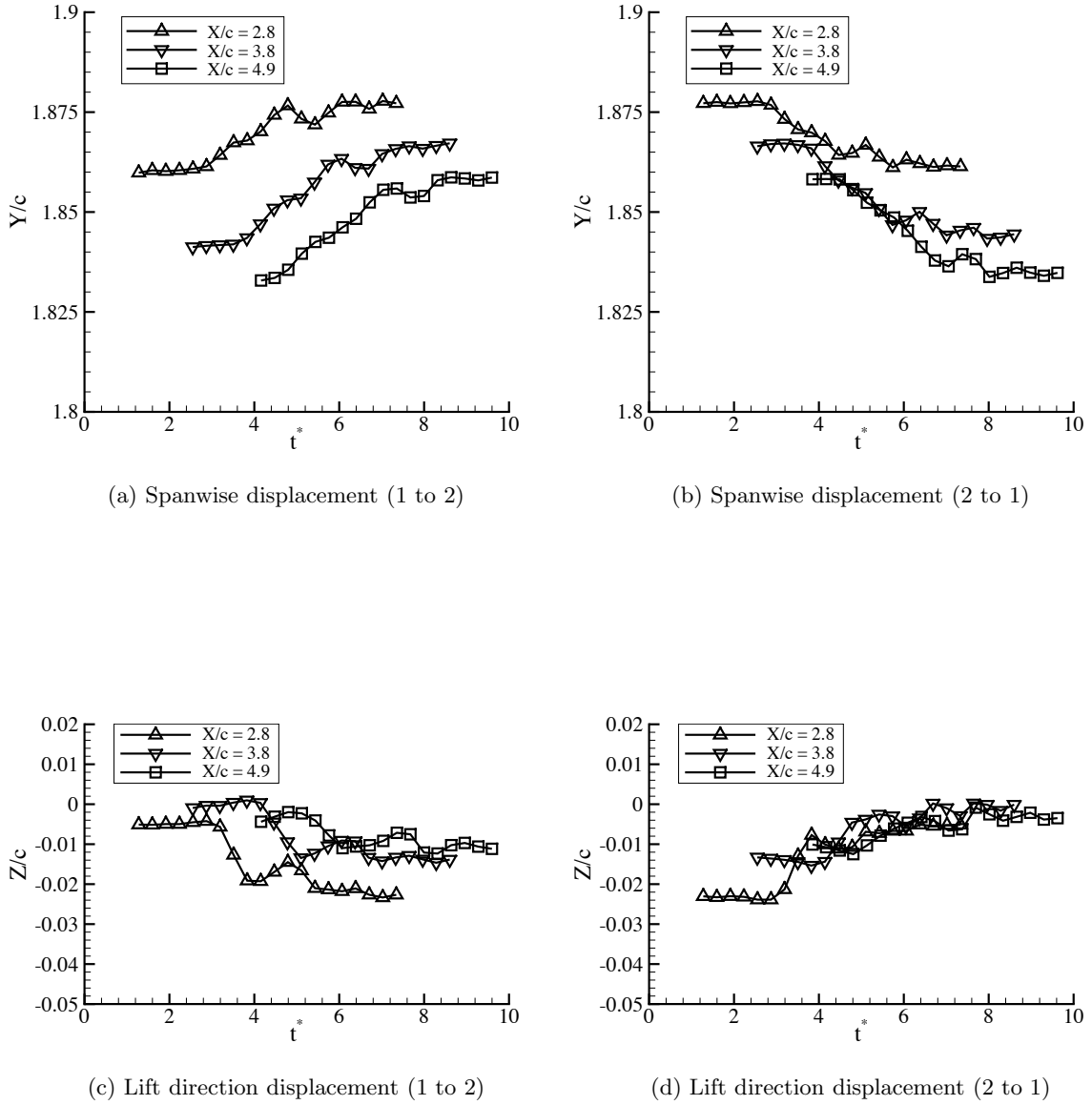


Fig. 3.26. Transient response of the vortex center location for the simple MiTE actuation scheme where configuration 1 is the neutral case and configuration 2 is $(Y/a)_{flap} = 0.854$, $a_{down}/a = 0.13$. The uncertainty is smaller than the symbol size.

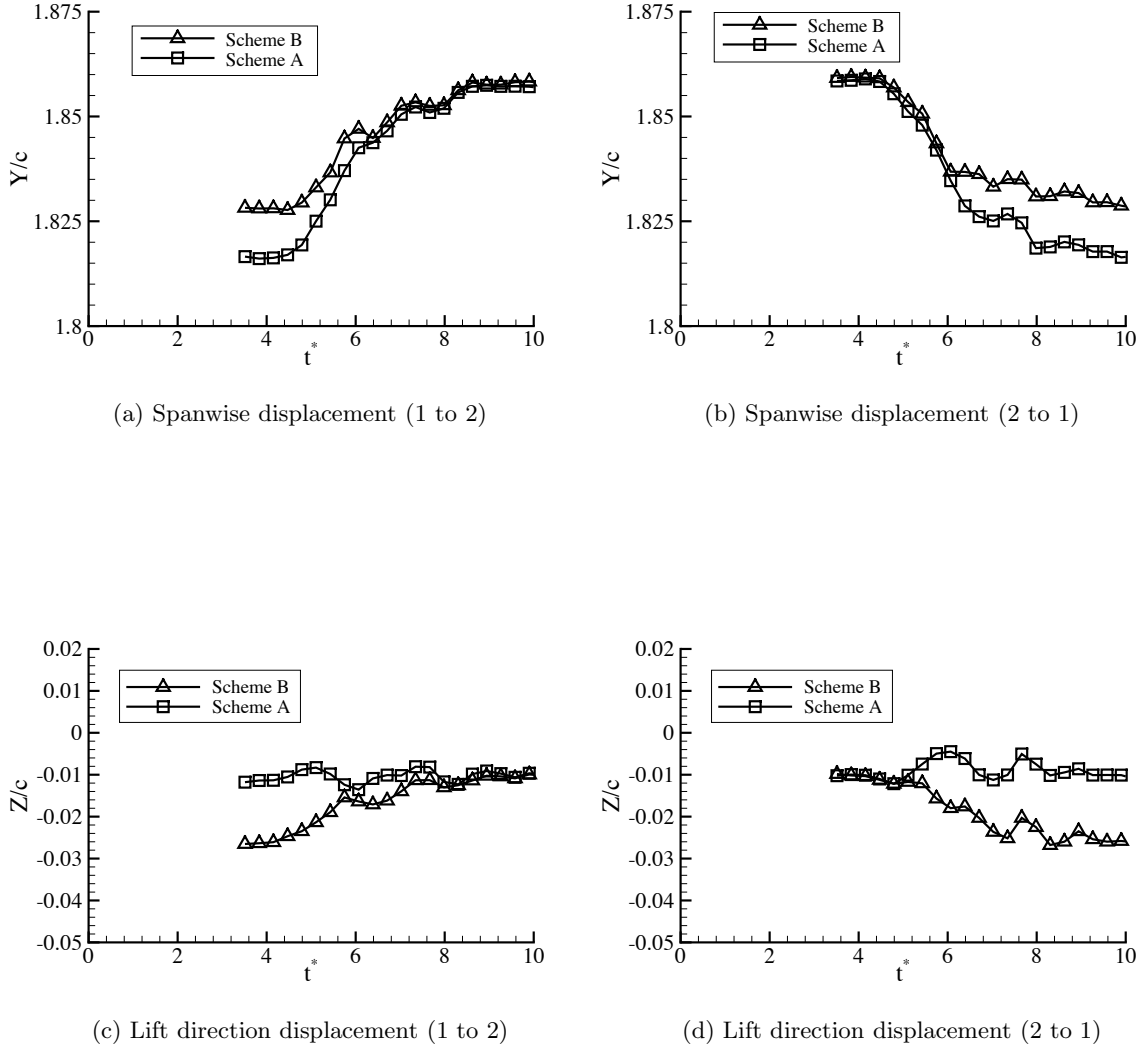


Fig. 3.27. Transient response of the vortex center location to MiTE actuation schemes A and B.

sinusoid, i.e., it contained wavelengths other than the predetermined fundamental mode. The measured vortex paths provided us with initial conditions for computations of the far wake evolution.

Chapter 4

Computational Results

4.1 Computational Approach

Data collected in the intermediate wake were used to form a set of complete initial conditions for a computation of the far wake evolution. Rennich (1997) showed that instability amplification rates could be predicted fairly accurately (errors $< 10\%$) if the wake data were taken far enough downstream such that the vorticity was essentially rolled up. Crouch et al. (2001) provided further confirmation of this. The data we had taken in the intermediate wake satisfied this criterion.

Up to this point, we have presented results in a reference frame that moves with the wing. Now, we consider a stationary reference frame where the flow is initially quiescent until the wing or aircraft moves through it at velocity U_∞ . Applying Taylor's hypothesis, changes in the vortex center location with respect to time in the frame of the moving wing became changes with respect to streamwise distance in the stationary frame. We assumed that the time taken by the aircraft to traverse the computational domain was much smaller than the time that would be required for any instability of the vortices to grow. Thus, the flow could be treated as periodic in the streamwise direction.

4.1.1 Vortex Filament Technique

The vortex filament technique has been used extensively to model vorticity dominated flows (Leonard (1980),(1985)). It was well suited for this application because the computed flow was governed mostly by vorticity concentrated along the locations of the trailing vortices. The lack of an Eulerian grid provided relatively fast computations which allowed us to analyze many cases and explore large parameter ranges. This technique afforded very good predictions of initial growth rates, and fair predictions at intermediate times. However, the method becomes less accurate as two vortices closely approach one another or the curvature of an individual vortex becomes too high. Rennich (1997) compared vortex filament calculations to Navier-Stokes computations for pure Crow instability. The results showed that the

filament technique tended to underpredict growth rates of the fundamental perturbation at the most unstable wavelength. Thus, we may assume that this technique is conservative for the purpose of identifying control strategies that produce rapid perturbation growth. We used the same code as Rennich and Lele, and all computations were terminated whenever a filament came within two cut-off distances of itself or another filament. These far wake vortex filament computations could not replace high accuracy Navier-Stokes computations, well designed far wake experiments, or actual flight testing. We used this technique only to provide us with a reasonably likely scenario of how the far wake may evolve given the clearly stated assumptions.

The code we used was developed at Stanford and was described in detail by Rennich (1997). This was an inviscid incompressible code wherein each vortex was represented by one smooth, continuous filament. Each filament was defined by a set of nodes in three dimensions that were connected by cubic spline elements. Induced velocity at each node was computed by performing the Biot-Savart integral along all filaments in the domain. The code used 5th order accurate Gaussian quadrature for integration and fourth order Runge-Kutta time advancement. A periodic boundary condition in the streamwise direction was enforced using ghost filaments. The cut-off technique was used to remove the singularity in the Biot-Savart law and to model the vorticity distribution of the vortex. This approach was discussed in detail by Crow (1970) and Widnall (1975).

The cut-off distance, d_{cut} , was chosen using the relation

$$\ln \frac{d_{cut}}{b'} = -\ln 2 + \frac{1}{2} - A + C \quad (4.1)$$

where A and C are corrections to account for tangential and streamwise velocities respectively, and are given by the relations

$$A = \lim_{r \rightarrow \infty} \left(\frac{4\pi^2}{\Gamma^2} \int_0^r r^* V_\theta^2 dr^* - \ln \frac{r}{b'} \right), \quad (4.2)$$

$$C = \lim_{r \rightarrow \infty} \left(\frac{4\pi^2}{\Gamma^2} \int_0^r 2r^* U^2 dr^* \right), \quad (4.3)$$

where r is the radial distance from the vortex center, r^* is a dummy variable for integration, V_θ is the tangential velocity, Γ is the total circulation in the vortex, and b' is the lateral vortex spacing distance given by the loading distribution used to create the vortex. The velocity field was measured over a large domain in the experiment using a five-hole probe. Limits going to infinity made it impossible to evaluate A and C exactly from the five-hole

probe measurements due to the finite measurement domain. They could be reasonably approximated by maximizing the r value at which the integrals in Eqs. (4.2) and (4.3) were evaluated. Figure 4.1 shows a plot of d_{cut} as a function of the radial extent of the integration domain. The curve shown is an ensemble average compiled using five-hole probe profiles from all of the MiTE configurations used in the active schemes. Changes in this curve due to changing MiTE configurations were small (± 0.002 in d_{cut}/b'). Clearly, d_{cut} had not completely converged, but as we will see below, the final results were relatively insensitive to d_{cut} .

The primary output from the computations is an estimate of the time it takes for the vortices to link up. All computations were terminated whenever a filament came within two cut-off distances of itself or another filament. The time at which this occurred was designated T_{link} . Vortex linking is a highly viscous process that could not be modeled properly with a computation of this sort. Thus, the relationship between T_{link} as we defined it and the actual vortex linking time was not known, however, the parameter T_{link} provided us with a rough estimate of linking time and was a good parameter for fair comparison between the various cases examined. We examined the sensitivity of T_{link} to variations in d_{cut} and λ , where λ is the streamwise perturbation wavelength. Results from the parametric study are shown in Fig. 4.2. Initial perturbation shapes used here were sinusoidal, and the vortex configuration was identical to that of our model case which will be discussed later. There was clearly a weak dependence of T_{link} upon d_{cut} . Furthermore, slight modifications in λ could eliminate any difference. Thus, we took the value of d_{cut} to be the largest measured value from Fig. 4.1, $d_{cut}/b' = 0.0332$. This nondimensional value was used for all computations.

The strength of the vortex was taken from a measurement of C_{l_0} , the section lift coefficient at the spanwise station closest to the root ($Y/a = 0.081$). Vortex circulation, Γ , was related to C_{l_0} by $\Gamma = (1/2)C_{l_0}U_\infty c$, which comes from lifting line theory. The effect upon C_{l_0} of the flap configurations examined was very small, thus Γ was left constant along the filament. Several trial cases were run that demonstrated that varying Γ along the filament (while accounting for the resulting spanwise vortices) tended to reduce T_{link} , thus, leaving Γ constant was more conservative.

Time and filament refinement studies using sinusoidal perturbation shapes were performed in order to insure that sufficiently fine time step and nodal spacing were used. All cases in this work were run using $(\Delta t \Gamma)/(2\pi b'^2) < 0.04$ and $(\Delta x)/(b') < 0.2$ where Δt

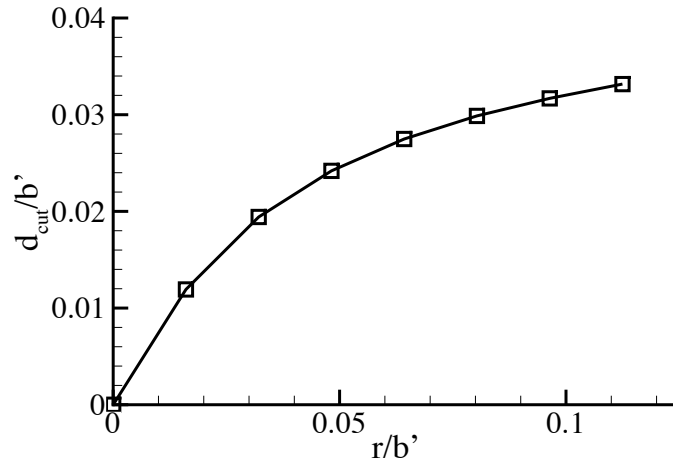


Fig. 4.1. Relationship between cut-off length and chosen domain size.

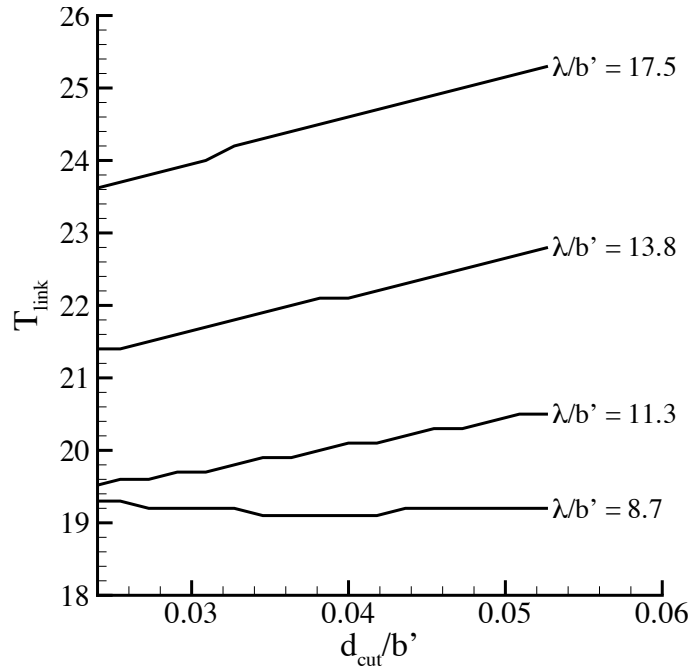


Fig. 4.2. Parametric study on the influence of d_{cut}/b' and λ/b' upon T_{link}

was the dimensional time step, and Δx was the dimensional initial nodal spacing in the X direction. Further refinements in both time steps and nodal spacing indicated changes in T_{link} of less than 2%.

4.1.2 Generation of Initial Conditions

The most critical information required for performing these computations was the initial shape of the filaments. We used the dynamic PIV results to determine this, and the exact procedure is described as follows. First, we changed our reference frame as described earlier. From the dynamic PIV, the transient motion of the vortex center as a function of time at $X/c = 4.9$ was converted into a spatially varying path using Taylor's hypothesis with the convection velocity taken as U_∞ . Thus,

$$(X)_{computations} = (U_\infty t)_{experiments}. \quad (4.4)$$

From here on, we refer to $X_{computations}$ as simply X , aware that we are now in the stationary reference frame. For all actuation schemes considered, the MiTEs' motion was relatively fast, so the streamwise distance required for the vortex to move from (1 to 2) or (2 to 1) was always smaller than half of the wavelength of the instability we attempted to excite. Thus, the periodic shape of the filament consisted of going from configuration 1 to 2 along the corresponding experimentally determined path, waiting a set time, then moving from 2 to 1 along another experimentally determined path, waiting a set time, and repeating the process. Using Eq. (4.4), we converted each t^* data point from the dynamic PIV measurements to a node at (X, Y, Z) for (1 to 2) and (2 to 1). In order to construct just one full period of a filament, connector nodes were added before (1 to 2), in between (1 to 2) and (2 to 1), and after (2 to 1) generating the desired wavelength. The spacing for these connector nodes was chosen to be as close as possible to the spacing of the data nodes. Finally, the nodal (Y, Z) positions were calculated by linear interpolation from the start and end points of the data nodes while maintaining periodicity of the filament. The X origin was arbitrary. Each vortex was represented by one filament. Initial conditions were generated for two filaments such that they were symmetric with respect to the XZ plane at $Y = 0$.

Filament computations were run for several vortex configurations. The first case examined was at the model scale, where all parameters were taken exactly from the experiment. Then, we nondimensionalized the experimental parameters, and used them to derive three

Table 4.1. Computational parameters for the model scale case.

	b' (m)	Γ (m ² /s)	λ/b' (m)
Model Scale Case	1.100	2.19	9.36

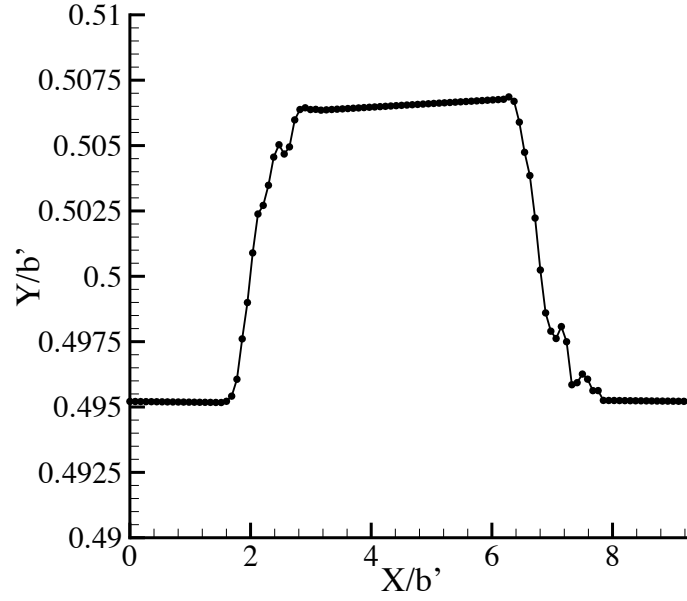
other cases whose total lift, span, and chord were close to those of a large commercial aircraft. These full scale cases were calculated to examine how perturbations created by the MiTEs might be used to excite other instabilities known to exist in wakes with multiple vortex pairs in a more realistic configuration.

4.2 Model Scale Case

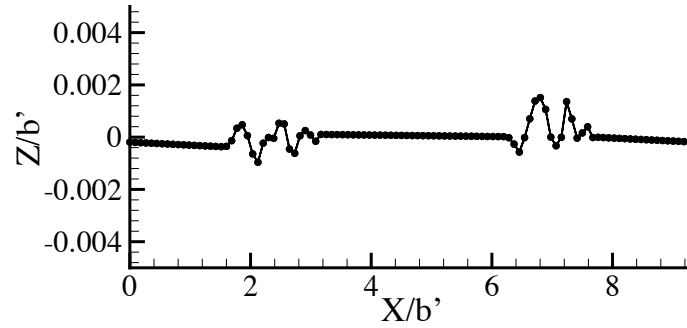
All of the computational parameters for the first simulation were taken directly from the experiment and are given in Table 4.1. Figure 4.3 illustrates the initial filament shape created by scheme A, for which the perturbation was mostly in the spanwise direction. Since the perturbation amplitude was small, the Y -axis scale is greatly exaggerated. The streamwise wavelength, λ , that we choose for this computation was $9.36b'$ which was close to the most unstable wavelength for Crow instability on these filaments. Figure 4.4 shows a perspective view of several wavelengths of the filaments at four points in time, and Fig. 4.5 shows snapshots in the XY and XZ planes for one wavelength at the same four time points. The most obvious trend was that the vortices moved down by mutual induction at a nearly constant velocity. The growth of the Crow instability in the spanwise direction was apparent after 6.0 s. Beyond $t = 12$ s, the perturbation amplitude grew rapidly until the vortices approached one another too closely. At $T_{link} = 18.0$ s, the computation was terminated.

Despite the presence of shorter wavelengths in the initial filament shape, the evolution of long wavelength Crow instability was essentially unaffected. Computations run with the same parameters but a pure sinusoidal perturbation rather than the measured shape were nearly identical. This confirmed the expected lack of receptivity of Crow instability to relatively short wavelengths.

The same computation was run using the initial condition given by scheme B, where the perturbation shape was closer to the most unstable Crow eigenmode, but the amplitude



(a) Spanwise initial condition



(b) Lift direction initial condition

Fig. 4.3. Initial condition generated from transient response data for scheme A.

was slightly smaller. It was found that T_{link} was slightly shorter for scheme B, but the difference was small, and the overall results were very similar, thus, we only present scheme A.

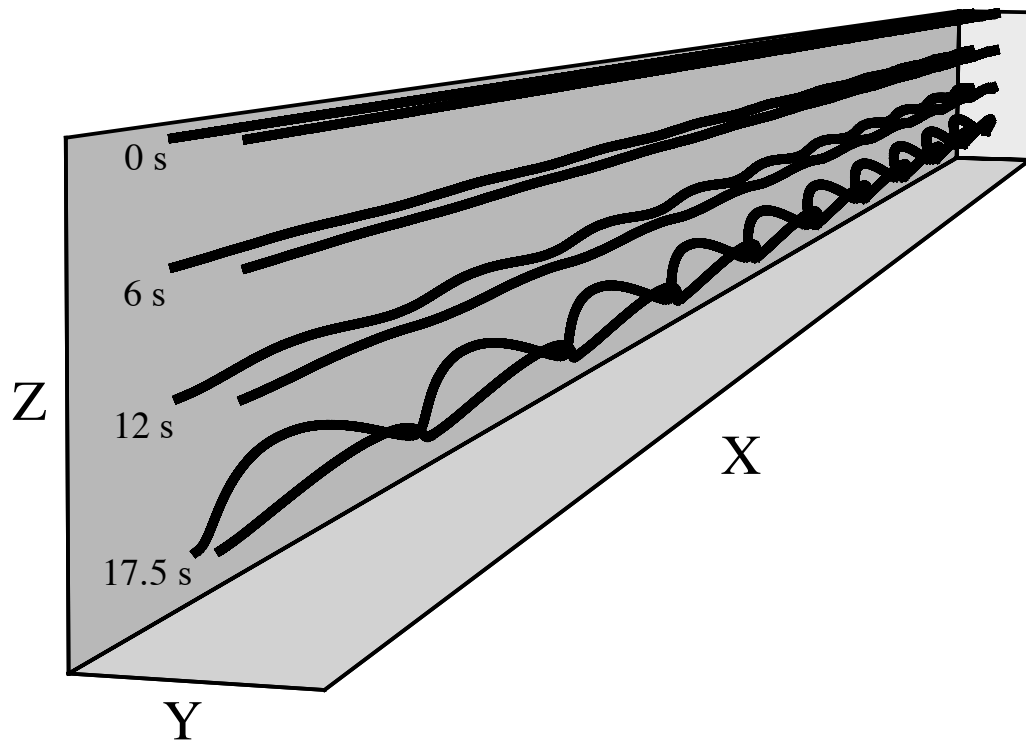
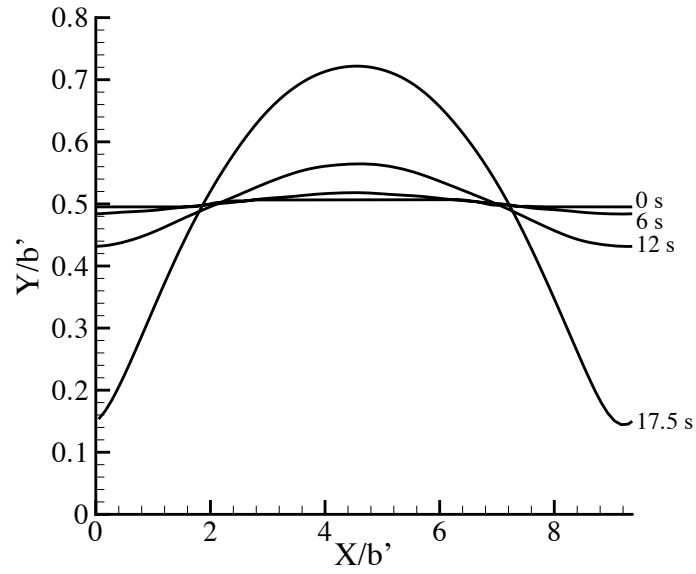
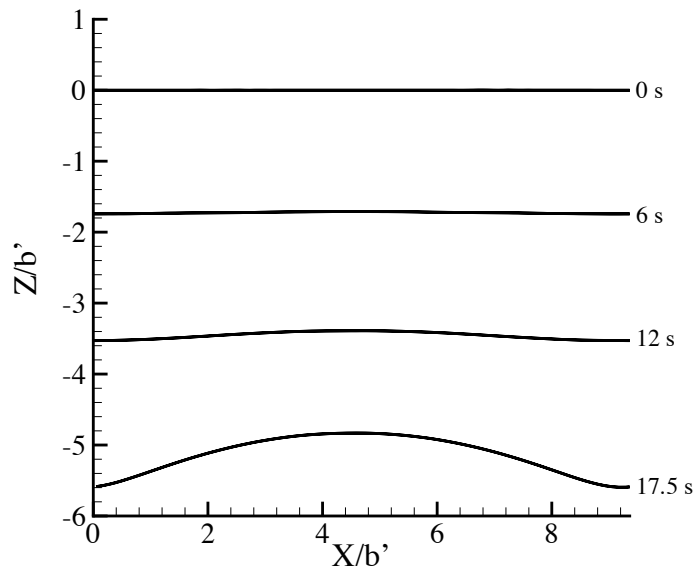


Fig. 4.4. A perspective view of the filaments for the model scale case at four points in time.



(a) Spanwise evolution



(b) Lift direction evolution

Fig. 4.5. Snapshots in time of the filaments for the model scale case in the XY and XZ planes.

4.3 Full Scale Cases

4.3.1 Three Representative Vortex Configurations

The model scale results were encouraging in that they demonstrated that Crow instability could be easily excited using the perturbations created by the MiTEs. The vortex configuration of the experimental model, however, was very different from that of a commercial aircraft during take-off or landing. Also, it has been well established that Crow instability tends to exhibit rather slow growth rates when compared to other inviscid instability mechanisms involving more vortices (Crouch et al. 2001; Rennich 1997; Crouch 1997; Spalart 1998; Rossow 1999). Thus, we examined whether or not vortex perturbations created by MiTEs could excite other instabilities on wakes that more closely resemble that of large commercial aircraft. We used our experimental parameters to derive three full scale vortex configurations.

As discussed earlier, both take-off and landing configurations are of greatest concern regarding wake vortex hazard. For constructing full scale configurations, we used reasonable values for a large commercial airliner at take-off. Take-off was chosen over landing because the vortex strengths during landing tend to be higher than during take-off in spite of the reduced weight of the aircraft because of the much lower speed. Higher vortex strengths typically result in shorter linking times, thus, using the take-off configuration was more conservative.

The measured nondimensional loading distribution was applied to a hypothetical aircraft with a mean aerodynamic chord of 9 m, a wing span of 66 m, a total lift of 430 tons, and a velocity of 82 m/s. The perturbation amplitudes in the Y and Z directions were scaled with the vortex separation. In order to convert the time-varying response of the vortex to a streamwise spatial variation, we invoked the same assumptions used previously, and in addition, we assumed that the MiTEs on our hypothetical full scale configurations were dynamically equivalent to the MiTEs used in experiments, i.e.,

$$\left(\frac{\Delta t U_\infty}{c}\right)_{\text{experiment}} = \left(\frac{\Delta t U_\infty}{c}\right)_{\text{fullscale}}. \quad (4.5)$$

Note that the c for the full scale configuration is the mean aerodynamic chord mentioned above. Thus, the actuation time required for the full scale configuration was about 0.4 s.

For fair comparison of our results to results with alternative loading distributions, we introduced a nondimensional time variable based on an elliptic loading distribution with

Table 4.2. Computational parameters for the full scale cases.

	b'_{12} (m)	b'_{34} (m)	Γ_{12} (m ² /s)	Γ_{34} (m ² /s)	λ/b'_{12}
1P	58.68	N/A	696.0	N/A	9.36
2PCR-long	58.68	18.20	627.8	219.7	6.45
2PCR-short	58.68	18.20	627.8	219.7	2.81
2PCTR	58.68	15.26	841.0	-557.6	9.36

the same total lift as our three hypothetical cases, $\tau = (\Gamma_{ell}/(2\pi b'_{ell}))t$.

Three hypothetical full scale vortex configurations were examined: the one pair configuration (1P), the two pair co-rotating configuration (2PCR), and the two pair counter-rotating configuration (2PCTR). For each case, we derived a different loading distribution and vortex configuration. The wing span, total lift, and velocity for each case were the same and were held at the values mentioned above. The first case involved a simple scaling of our experimental loading distribution. The other two involved superposing two scalings of our loading distribution with different individual spans and lifts but producing the same total lift. The cut-off length, d_{cut} , was scaled with the lateral vortex separation for each vortex pair. These three vortex configurations are shown schematically in Fig. 4.6, and the loading distributions that would produce them are shown in Fig. 4.7. The 2PCR case was motivated by the work of Crouch et al. (2001), wherein long and short wavelength instabilities that evolved faster than pure Crow instability were shown to exist. The 2PCTR case used a special loading distribution based on the work of Rennich and Lele (1999), wherein an accelerated long wavelength instability was shown to exist. The computational parameters for each are given in Table 4.2. For all hypothetical loading distributions, we perturbed only the outboard vortices, thus implying that MiTEs were placed only near the wing tips. We limited our study to symmetric perturbations only. Again, schemes A and B proved to be very similar with slightly faster growth rates for scheme B, thus, we only present results from scheme A.

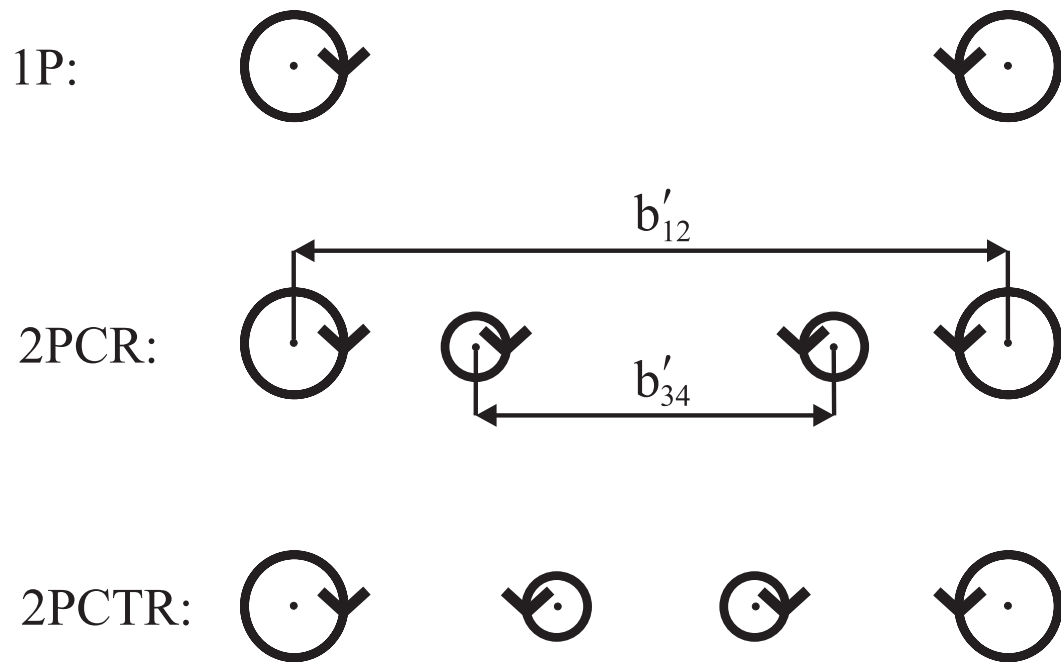


Fig. 4.6. Diagram of the three vortex configurations examined.

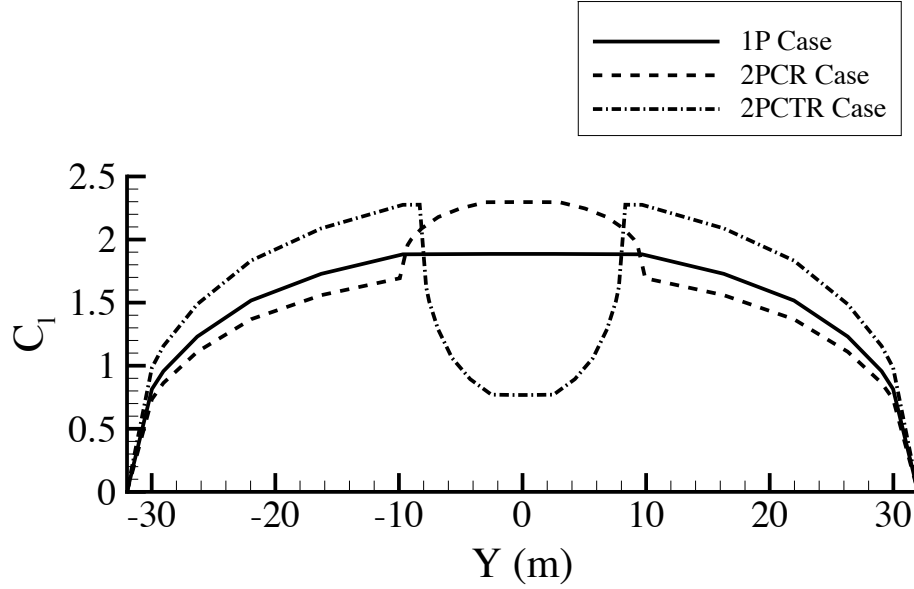


Fig. 4.7. The spanwise loading distributions required to generate the vortex configurations examined.

4.3.2 One Pair Case

For the 1P case, the evolution of Crow instability followed the predicted exponential growth rate and was quite similar to that of the model scale case. Close approach of the two vortices occurred at $\tau = 6.92$. This gave a baseline for comparison with other full scale cases.

4.3.3 Two Pair Co-Rotating Case

For the 2PCR configuration, each inboard vortex (3 and 4) rotated in the same direction as its outboard counterpart (1 and 2), thus, the inboard vortices rotated about the outboard ones as the entire configuration descended regardless of which (if any) instability was growing. The spanwise spacing ratio, circulation ratio, and wavelength (b'_{34}/b'_{12} , Γ_{34}/Γ_{12} , and λ) were set close to the same values used by Crouch et al. (2001) and are given in Table 4.2 (2PCR-long). Several snapshots in time of the evolution of this configuration are shown in three dimensions in Fig. 4.8 and in the XY plane in Fig. 4.9. As the weaker inboard vortices rotated about the stronger outboard vortices, the long wavelength instability grew at the rate predicted by Crouch's analysis until close approach of the two outboard vortices

at $\tau = 4.07$. Here, the growth rate was indicated by the peak to peak displacement of the outboard vortices projected in the YZ plane. Unfortunately, the MiTE perturbations did not lead to much transient growth, nonetheless, they successfully excited this instability. Compared to pure Crow instability, we observed a significantly shorter time to close approach. Another important feature of this case was that as this long wavelength instability grew, the filaments also displayed a shorter wavelength perturbation which is apparent in Fig. 4.9e. This was brought on by the shorter wavelengths present in the initial filament shapes (due to the fast overall response of the MiTEs), but in this case, they did not affect the evolution of the long wavelength instability.

The relatively fast motion of the MiTEs (given our assumption of dynamic equivalence) allowed us to explore short wavelength instability (2PCR-short). Setting λ to the short wavelength symmetric mode described by Crouch (1997), we observed a higher initial amplification rate as expected. Several XY snapshots in time are shown in Fig. 4.11. Again, the weaker vortices rotated about the stronger vortices as the short wavelength instability grew. With this instability, however, at $\tau = 2.84$, close approach of the weaker inboard vortices occurred rather than the outboard ones, and it is unknown how the outboard vortices would evolve from there on.

4.3.4 Two Pair Counter-Rotating Case

Finally, we attempted to excite the accelerated instability mechanism described by Rennich and Lele (1999). The spanwise spacing and circulation ratios, b'_{34}/b'_{12} and Γ_{34}/Γ_{12} , were chosen according to the relation given by Rennich and Lele such that the entire system would translate downward rigidly and the vortices would not rotate around one another. The wavelength, however, was set close to the most unstable pure Crow mode for the outboard filaments, $\lambda = 9.36b'_{12}$, not the total effective span. Using the outboard vortex spacing proved to be more practical than using the total effective span because it allowed for much shorter wavelengths, and thus, fewer nodes. Some auxiliary computations showed that the amplification rate was roughly the same for either wavelength.

Figure 4.12 illustrates the accelerated instability mechanism of Rennich and Lele (1999), and is described as follows. The instability initially involved a long wavelength perturbation displacing the inboard pair in both the spanwise and lift directions. As the inboard pair was deformed, a long wavelength perturbation on the outboard pair became apparent. The perturbation on the outboard pair grew rapidly and caused linking to occur.

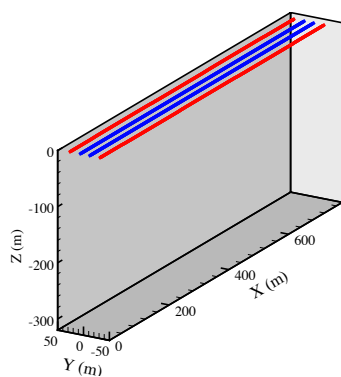
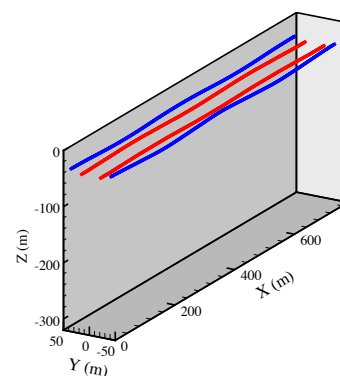
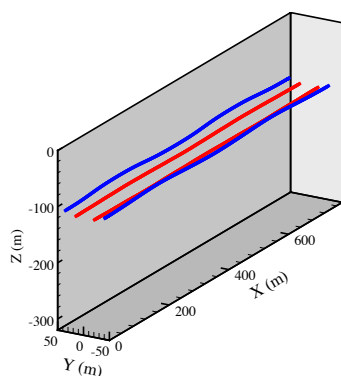
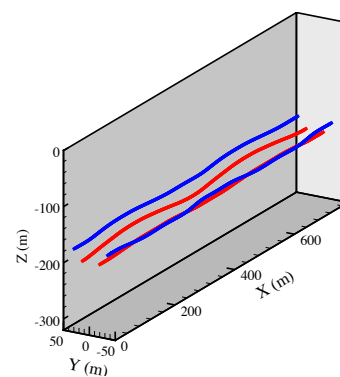
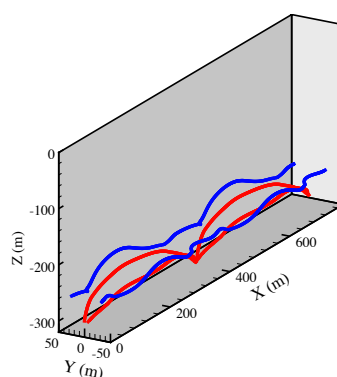
(a) $\tau = 0.0$ (b) $\tau = 0.58$ (c) $\tau = 1.74$ (d) $\tau = 2.91$ (e) $\tau = 4.07$

Fig. 4.8. Snapshots of the filaments for the 2PCR-long case. The strong, outboard vortex pair (vortices 1 and 2) is shown in red.

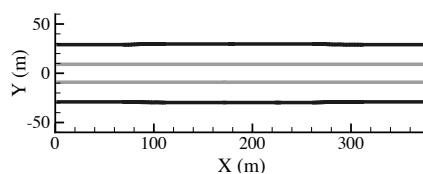
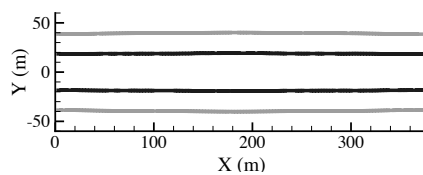
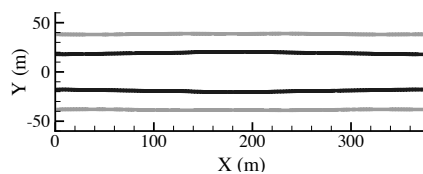
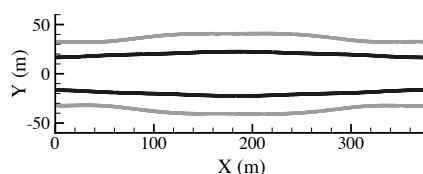
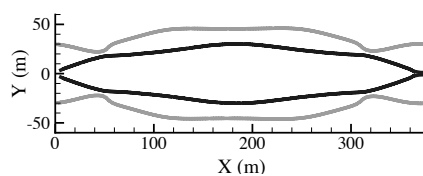
(a) $\tau = 0.0$ (b) $\tau = 0.58$ (c) $\tau = 1.74$ (d) $\tau = 2.91$ (e) $\tau = 4.07$

Fig. 4.9. Snapshots of the filaments for the 2PCR-long case in the XY plane. The strong, outboard vortex pair (vortices 1 and 2) is shown in black.

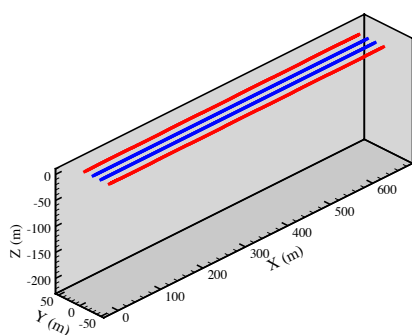
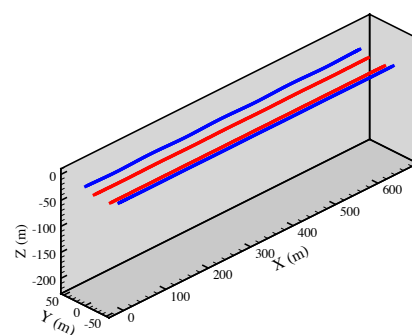
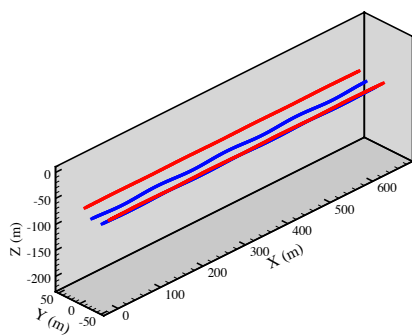
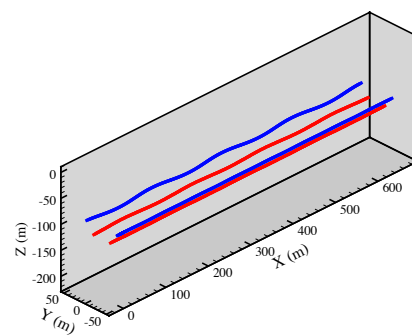
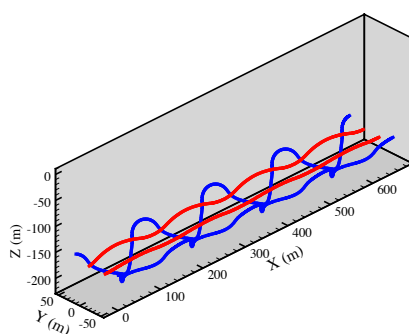
(a) $\tau = 0.0$ (b) $\tau = 0.61$ (c) $\tau = 1.22$ (d) $\tau = 1.82$ (e) $\tau = 2.82$

Fig. 4.10. Snapshots of the filaments for the 2PCR-short case. The strong, outboard vortex pair (vortices 1 and 2) is shown in red.

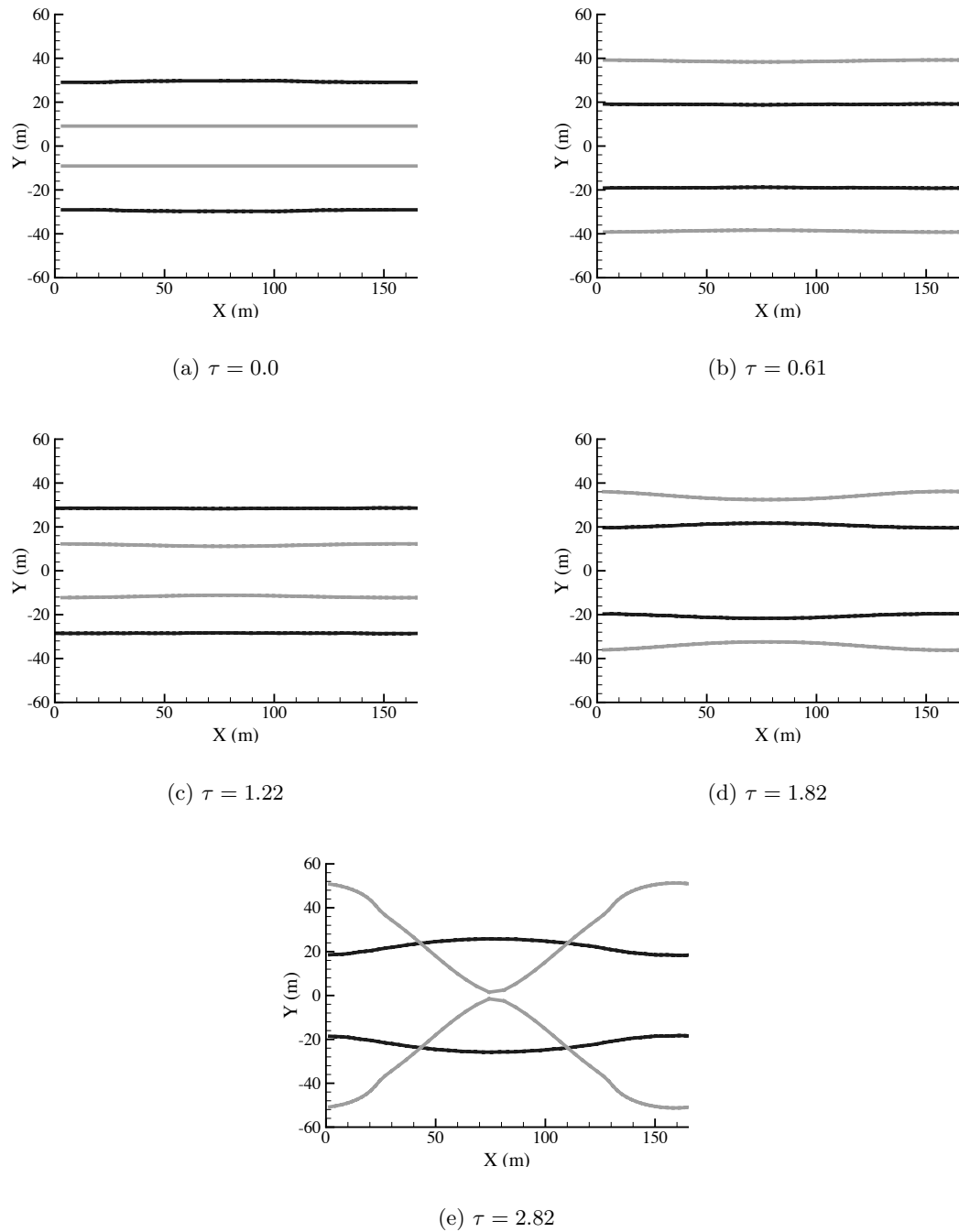


Fig. 4.11. Snapshots of the filaments for the 2PCR-short case in the XY plane. The strong, outboard vortex pair (vortices 1 and 2) is shown in black.

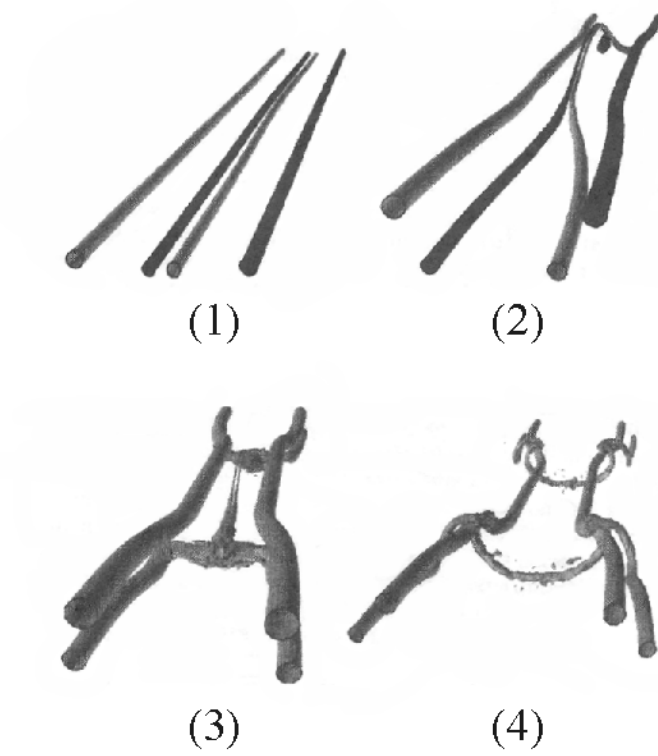


Fig. 4.12. The time evolution (1-4) of the accelerated instability mechanism of Rennich and Lele. Figure reproduced from Rennich and Lele (1999).

When the vortices were initially perturbed using the MiTE perturbation, we saw different behavior. Short wavelengths present in the initial condition of the outboard vortices (again, due to the fast overall response of the MiTEs) tended to impart short wavelength perturbations to the inboard vortices after a small amount of time. As a result, a pure Crow instability grew on the inboard pair and caused them to link before the outboard pair perturbation had grown by very much. This event corresponded to the faster growing instability mode discussed by Fabre et al. (2002) and Fabre and Jacquin (2000). Two XY snapshots shown in Fig. 4.14 illustrate this. To analyze this case more carefully, we examined the time evolution power spectrum of spanwise vortex center location with respect to streamwise wavelength on the inboard vortices, $G_{YY34}(\lambda, \tau)$. This spectrum quantified the magnitude of perturbations in the spanwise direction that were contained in different streamwise wavelengths of the inboard vortices. We considered two wavelengths: λ_1 corresponded to the long wavelength perturbation that would eventually lead to linking of the outboard pair, and λ_2 corresponded to the pure Crow instability growing on the inboard pair ($\lambda_1 \approx 9.36b'_{12}$, $\lambda_2 \approx 12.07b'_{34}$). The time evolution of the spectrum evaluated at these two wavelengths is shown in Fig. 4.15. Initially, the long wavelength dominated, but by $\tau = 0.35$, the short wavelength perturbation had become greater. This led to close approach of the inboard pair at $\tau = 0.45$ when the computation was terminated.

This receptivity to the shorter wavelengths present in the perturbation highlighted the importance in this case of the shape of the perturbation used, i.e., pure sinusoidal perturbations would not have caused this. It is likely that this inboard linking could have been avoided by slowing the motion of the MiTEs, but no experimental data on slower moving MiTEs was available. Attempts were also made to avoid this by modifying the circulation and span ratios of the vortex configuration in order to slow the growth of the instability on the inboard pair. It was found that lengthening the separation between the inboard pair, b'_{34} , was somewhat helpful, and this was why the configuration used in this work (given by the values in Table 4.2) differed from the configuration chosen by Rennich and Lele. No modification to this configuration was found that would prevent the premature inboard linking, however, a rigorous parametric study was not conducted as it was beyond the scope of this work.

Figure 4.16 summarizes the evolution of each instability mechanism that we have attempted to excite. Here, we plot the nondimensional displacement measure, δ_{Δ}/b' , of one outboard vortex as a function of τ . This displacement measure was simply the maximum

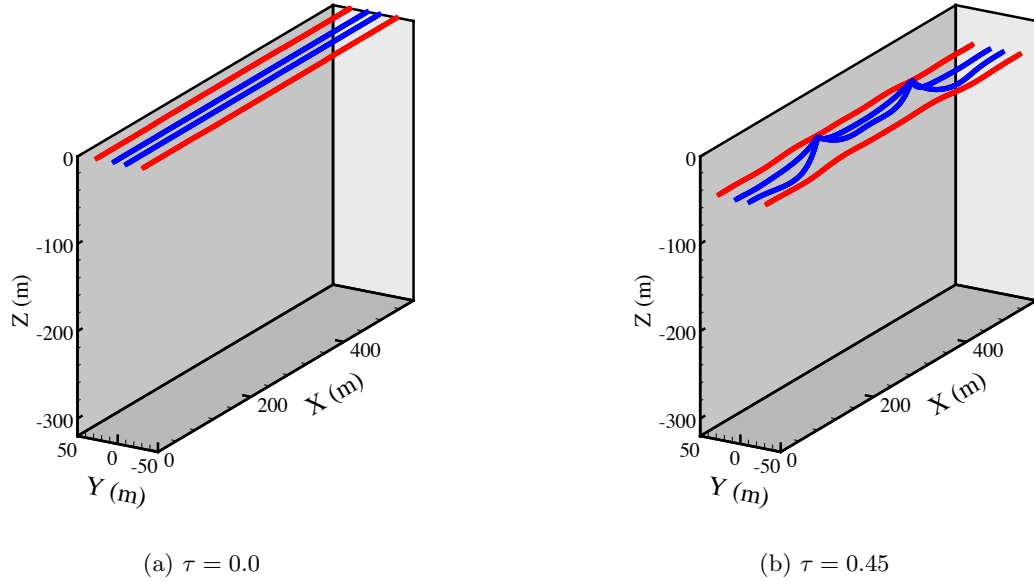


Fig. 4.13. Snapshots of the filaments for the 2PCTR case. The strong, outboard vortex pair (vortices 1 and 2) is shown in red.

peak-to-peak displacement of the vortex center projected on the YZ plane, a good measure of how perturbed a vortex has become. As indicated in the figure, the 1P and 2PCR-long cases were terminated upon close approach of the stronger, outboard vortices, while the 2PCR-short and the 2PCTR cases were terminated upon close approach of the inboard vortices. Since the parameter τ was based on an elliptic loading distribution of the same total lift as our three cases, we could compare these results to that of actual aircraft. For a Boeing 747-400 in calm atmospheric conditions, vortices can persist beyond $\tau = 5.4$ (Crouch et al. 2001). The 2PCR-long case clearly showed improvement over this. For the 2PCR-short and 2PCTR cases, if we assume that after the inboard pair linking occurs, the outboard pair would proceed to evolve at the slow pure Crow rate, again, there would be improvement. It is possible that after the inboard pairs link up, the instability on the outboard vortices would grow faster than pure Crow because whatever remains of the inboard vortices would continue to affect them.

Ultimately, it was clear that the perturbations created by MiTEs could be used to excite a variety of vortex instabilities. The Crow instability and the long and short wavelength instabilities of Crouch were excited flawlessly. The instability of Rennich and Lele presented

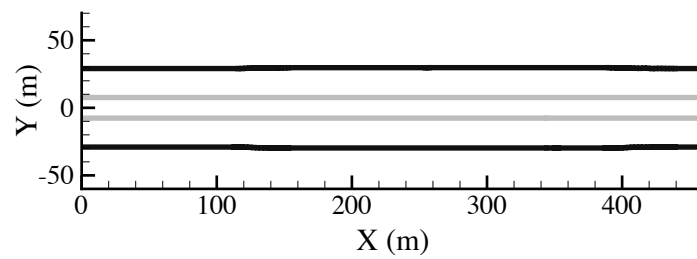
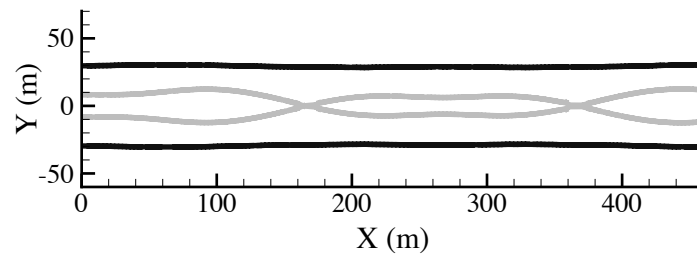
(a) $\tau = 0.0$ (b) $\tau = 0.45$

Fig. 4.14. Snapshots of the filaments for the 2PCTR case in the XY plane. The strong, outboard vortex pair (vortices 1 and 2) is shown in black.

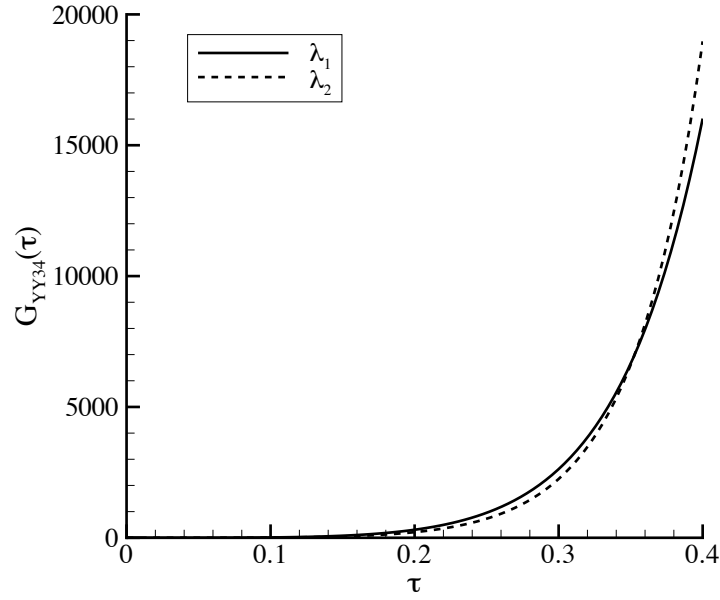


Fig. 4.15. The time evolution of the spanwise power spectrum at two wavelengths ($\lambda_1 \approx 9.36b_{12}$, $\lambda_2 \approx 12.07b_{34}$) for the 2PCTR case.

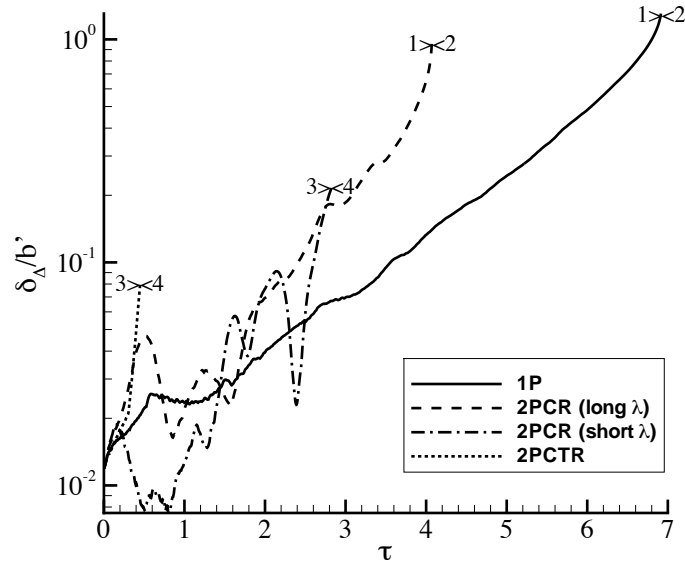


Fig. 4.16. The time evolution of the nondimensional displacement measure of one outboard vortex for all cases.

difficulties, however, it could clearly be excited if some modifications could be made to the MiTE response.

Chapter 5

Novel Wake Alleviation Device

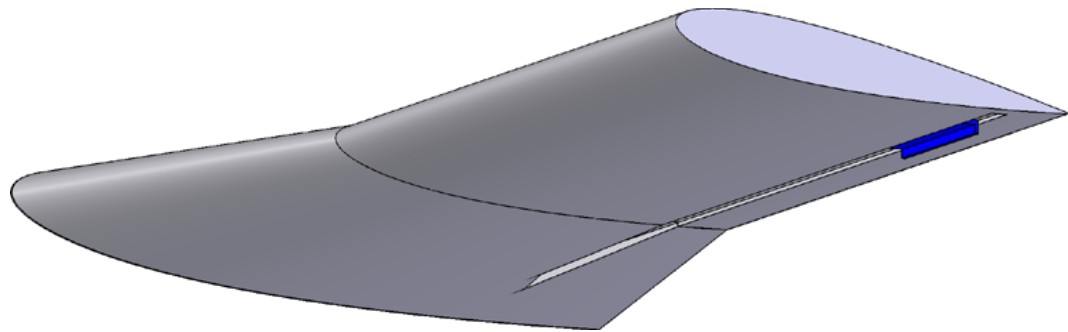
5.1 Spanwise Actuating Gurney Flap

The experiments and computations presented in Chapters 3 and 4 have demonstrated the feasibility of using the partial-span Gurney flap concept to perturb vortices in a way that would excite vortex instabilities and conserve lift. This study was conducted using a wing and a MiTE geometry that were chosen for research purposes and proof-of-concept, not for a practical aircraft. The components were fairly easy to design and fabricate, and they allowed us to examine a wide parameter range. However, particular characteristics of the wing and MiTEs, such as the blunt trailing edge, would not be desirable on an actual aircraft.

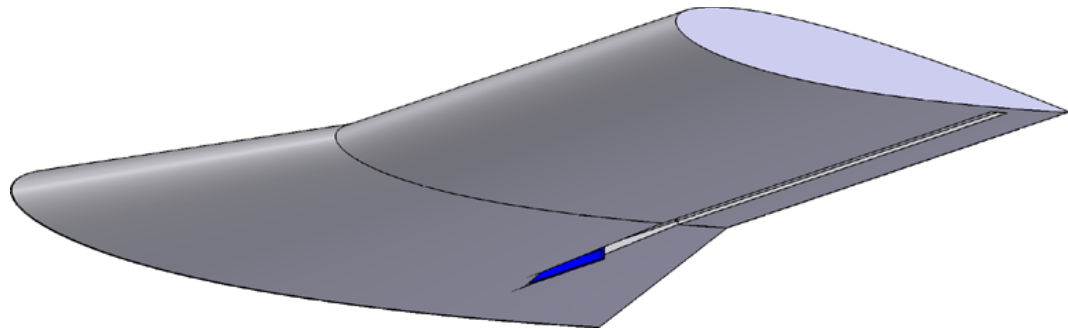
From the experiments, we established that in order to significantly perturb the vortex, only 13% of the span needed to be actuated at any given time. The actuated span was applied only near the tip of the wing where the loading distribution varied the most. This was a rather limited task that would not require a full array of MiTEs along the entire wing. We could, in fact, accomplish this using a much simpler device: the spanwise actuating Gurney flap.

We invented this device specifically for wake alleviation, and it is unique in that the control surface moves in the spanwise direction. Until now, there has not been a legitimate reason to use this degree of freedom. The basic design concept is shown schematically in Fig. 5.1. In order to achieve an actuation scheme very similar to the most effective MiTE schemes, one solid Gurney flap of small actuation ratio is mounted in a slot oriented in the spanwise direction on the pressure side of the wing. In order to maintain a sharp trailing edge, the slot is located upstream of the trailing edge. The flap can move inboard and outboard in the slot along the wing as required. When needed (i.e., during take-off and landing) the flap would be periodically oscillated near the tip at the appropriate frequency. When not in use, it would be stowed in the thicker portion of the wing near the root.

We expected the behavior of a trailing vortex in response to this device to be similar to what we had observed in the MiTE data. The effectiveness of the spanwise actuating



(a) Active configuration



(b) Stowed configuration

Fig. 5.1. Conceptual design of the spanwise actuating Gurney flap shown in two configurations.

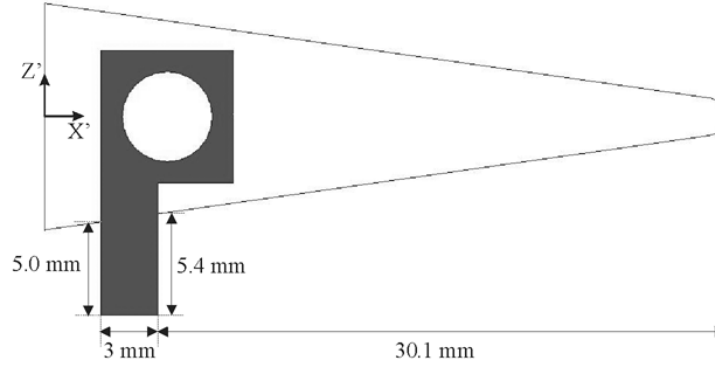


Fig. 5.2. A two-dimensional view of the assembled actuator in the XZ plane.

Gurney flap for wake alleviation was evaluated in the same way as the effectiveness of the MiTEs. We began by constructing a prototype making use of the NACA 0012 wing which had already been fabricated. Then we performed experiments to determine only the two most important parameters: the vortex strength and the vortex center locations for various flap positions. The design, fabrication, and testing of the prototype are described in the following sections.

5.1.1 Detailed Prototype Design and Fabrication

The prototype spanwise actuating Gurney flap was designed to fit onto the existing NACA 0012 wing in place of the array of MiTEs. To allow for a sharp trailing edge, the flap location was just forward enough to allow room for the mechanism. It was placed roughly 32 mm, or $10.2\%c$, upstream of the trailing edge. A schematic of the actuator in the XZ plane is shown in Fig. 5.2. With this new trailing edge, the chord length of the wing was 313 mm. The flap protruded roughly 5.2 mm ($1.7\%c$) into the flow.

The actuator assembly was comprised of five major components: flap, leadscrew, housing, cover plate, and tip cap. An exploded Solidworks rendering of the assembly illustrating each of these components is shown in Fig. 5.3.

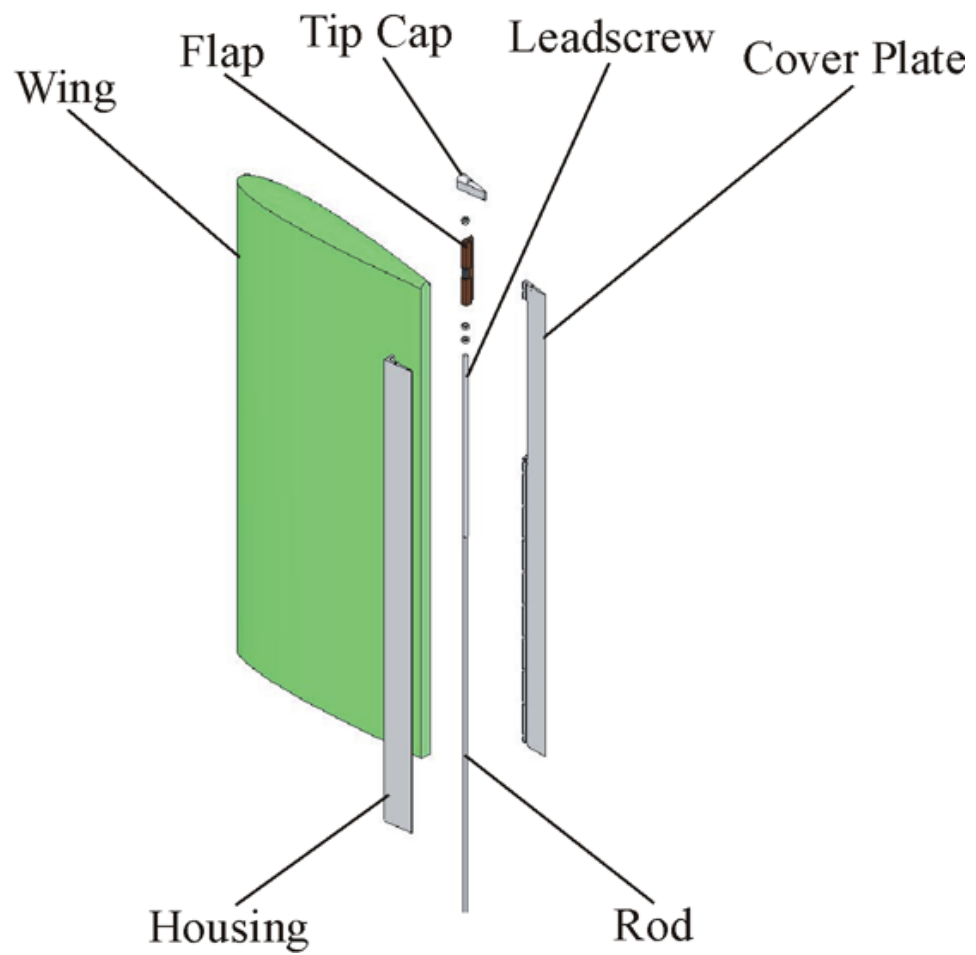


Fig. 5.3. An exploded Solidworks rendering of the wing and spanwise actuating Gurney flap.

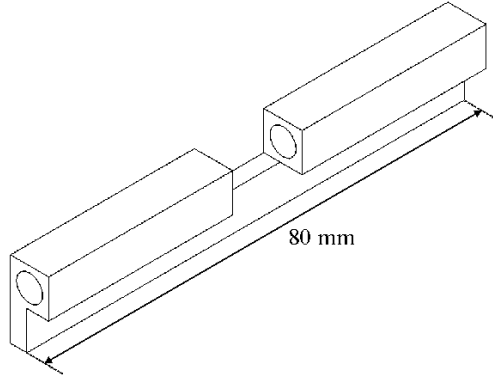


Fig. 5.4. A schematic of the solid flap with hole for the leadscrew and gap for nut.

A schematic of the flap is shown in Fig. 5.4. It was machined from a block of PTFE-Filled Delrin which was chosen to minimize friction and provide high resistance to wearing. It was 80 mm long in the spanwise direction, thus the actuation ratio (a_{down}/a) was a constant 0.13. In order to actuate the flap, a gap was machined in the body of the flap and a nut was embedded there.

We used a 3/16" multiple-start steel leadscrew of high pitch angle to move the flap in the spanwise direction 0.37" per revolution. The leadscrew was mated to a smooth steel rod which extended inboard through the root of the wing and then outside the tunnel. Only static tests were conducted, so the flap location was controlled by manually turning the rod. Tick marks at 12.4 mm increments were put on the outside of the cover plate to indicate the location of the flap.

The flap and leadscrew were contained by the housing, cover plate, and tip cap. An exploded view of just these three components is shown in Fig. 5.5. After the MiTEs were removed from the wing, the housing could be connected directly to the trailing edge using small bolts spaced evenly about the span of the wing. The bolts screwed into threaded inserts embedded in the wing. A slot 204 mm long in the spanwise direction was machined through the cover plate to allow the flap to protrude on the pressure side of the wing and actuate. To secure the flap and leadscrew, the cover plate connected to the housing with small bolts distributed across the span. Finally, the tip cap screwed into the housing and cover plate at the tip of the wing. All holes were recessed and filled in with clay to maintain a smooth surface.

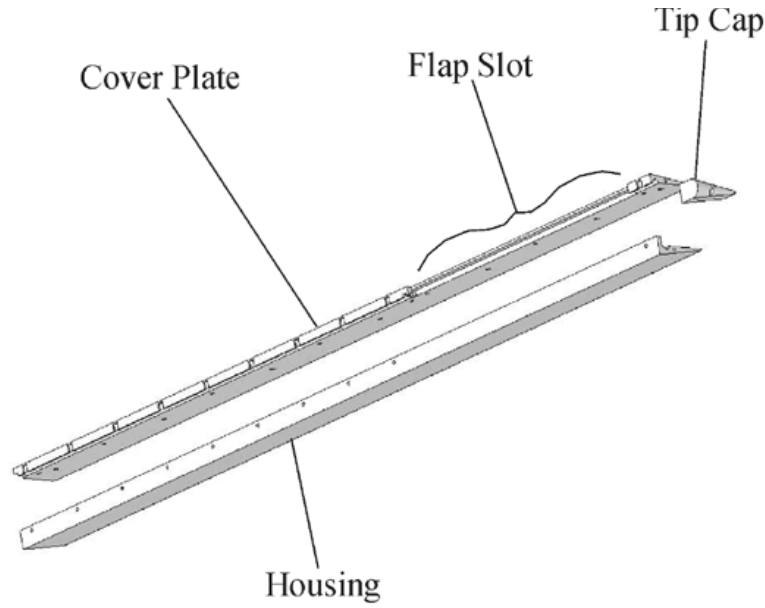


Fig. 5.5. An exploded view of the housing, cover plate, and tip cap.

Figure 5.6 shows a picture of the wing and spanwise actuating Gurney flap after final assembly mounted in the wind tunnel.

5.1.2 Wing Aerodynamic Effects

Measurements of the root section lift coefficient were performed to determine how much the spanwise actuating Gurney flap affected the strength of the trailing vortex. Pressure profiles at $Y/a = 0.081$ were measured for the minimum and maximum Y_{flap}/a values. The profile for $Y_{flap}/a = 0.654$ (the minimum value) is shown in Fig. 5.7. Between the minimum and maximum values ($Y_{flap}/a = 0.654$ and 0.854), the section lift coefficient varied from 0.749 to 0.740, which implied a nondimensional vortex strength, $\Gamma/(Uc)$ between 0.374 and 0.370. Thus, the change in C_{l_0} due to moving the flap across its entire range was indistinguishable from the uncertainty in the measurement.

5.1.3 Intermediate Wake Results

Static PIV experiments were conducted in the intermediate wake at $X/c = 4.66$ in exactly the same fashion as the PIV experiments on the MiTEs. We varied Y_{flap}/a across



Fig. 5.6. The wing and spanwise actuating Gurney flap assembled and mounted in the wind tunnel.

its entire range from 0.654 to 0.854 in increments of 0.020. The mean vortex center location from 500 PIV samples at each flap position is shown in Fig. 5.8. We saw the same trends here that we saw in the MiTE experiments. In general, the highest values of Y_{flap}/a moved the vortex outboard, the lowest values moved the vortex inboard, and at values in between, the vortex was displaced in the downward direction. The most notable difference between these experiments and the MiTE experiments was that the maximum spanwise displacement of the vortex was about one third of what we saw with the MiTEs. The primary reason for this was likely that the flap was located upstream of the trailing edge since that was the main difference between the two experiments. It is also likely that with a larger flap, greater spanwise displacement could be achieved.

These results demonstrated that the spanwise actuating Gurney flap could affect the trailing vortex in a manner very similar to the MiTEs. Thus, this novel aerodynamic actuator could be used as a practical and easily implementable device for active wake alleviation.

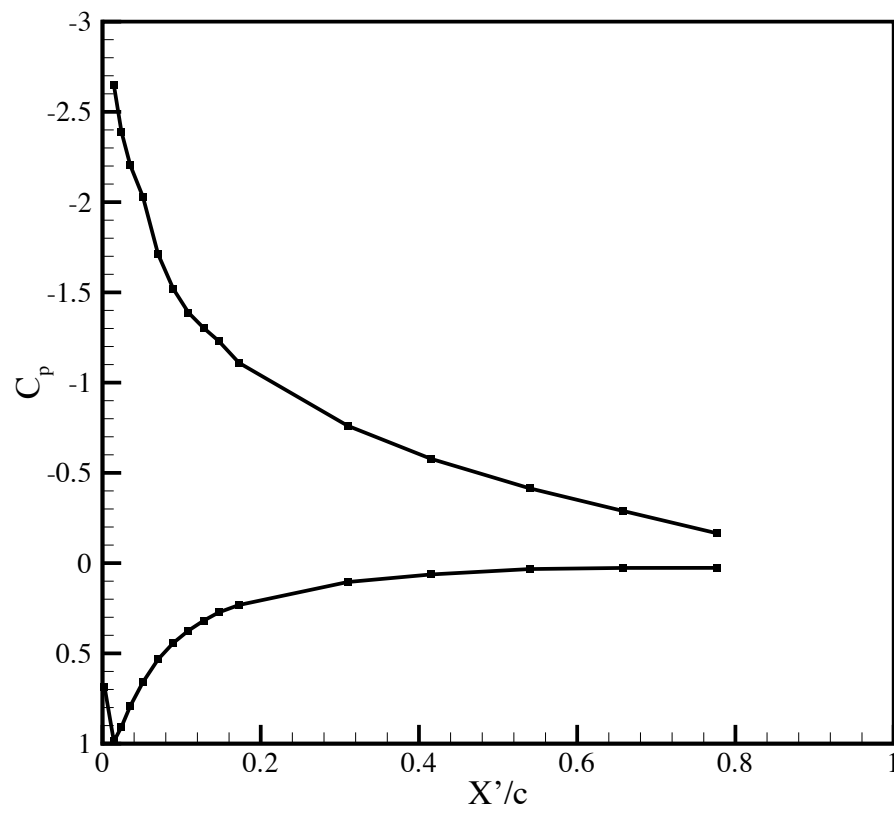


Fig. 5.7. The root streamwise pressure profile for the wing equipped with spanwise actuating Gurney flap set to $Y_{flap}/a = 0.654$.

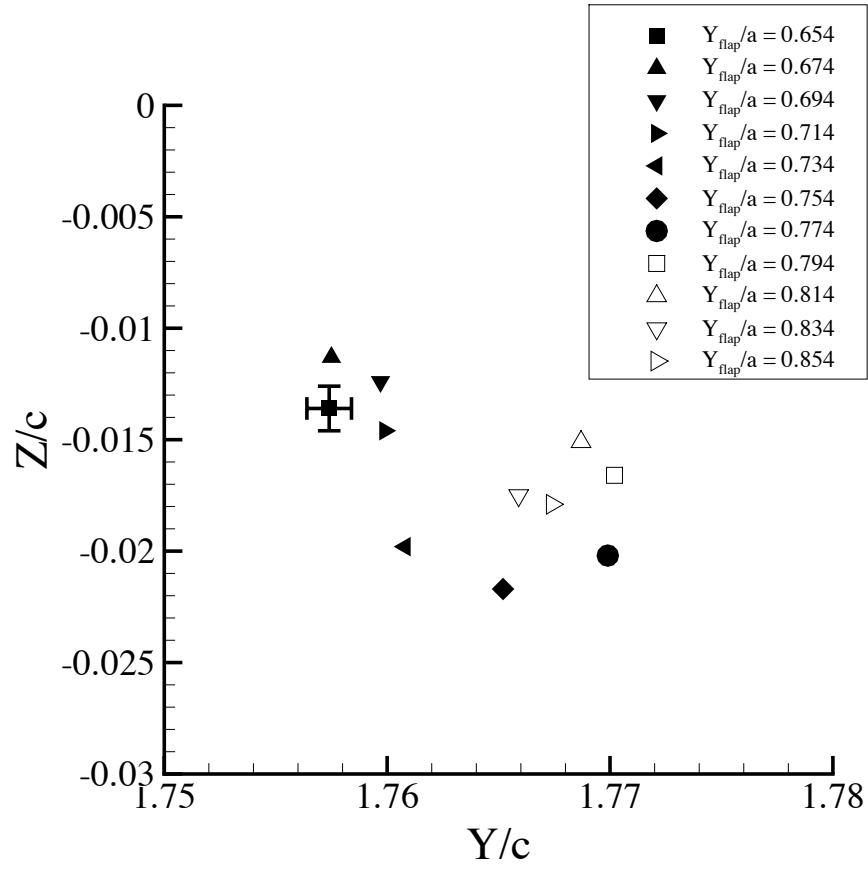


Fig. 5.8. Mean vortex center locations for different Y_{flap}/a values at $X/c = 4.66$. The uncertainty in both directions for all points is shown on one point.

Chapter 6

Conclusions and Recommendations

6.1 Summary of Conclusions

6.1.1 Alteration of Lift Distribution

To assess the potential effectiveness of MiTEs for wake vortex alleviation, we needed to first determine what forces the wing would experience due to various MiTE configurations. Thus, we examined the capability of the MiTEs to alter the wing lift distribution. First, we studied the full span down configuration. We verified that our new MiTE design displayed similar effects upon the section lift coefficient that had been noted by other researchers. For the full span down configuration, the total lift could be incremented by 12.3% compared to the neutral case. The most important characteristic of the full span down case was how the lift increment was distributed across the span of the wing. Rather than causing a constant increment, the increment was large near the root where the section lift coefficient was high, and small near the tip where the section lift coefficient was low. The percentage increase in section lift coefficient at any point along the span was roughly constant (within 1%). Thus, for a three-dimensional wing, MiTE effectiveness along the span depended upon the nominal loading distribution. This result has implications in determining how various partial-span MiTE configurations would affect the total lift.

Second, we examined partial-span configurations where large amounts of the span were actuated down. These configurations demonstrated the quasi-linear behavior of partial-span Gurney flaps which had been previously shown on two-dimensional airfoils by other researchers. For these large actuation ratios, the increment in section lift coefficient at one spanwise location depended on the amount of span actuated down, not just the location of the actuated span. Also, the spanwise increments in loading distribution due to several different partial-span configurations involving distinct sets of MiTEs could be superposed to produce the same spanwise increment that would occur if those MiTE configurations were combined.

Finally, we examined small actuation ratio configurations. These quickly became the

best candidates for use in active wake alleviation schemes as it was very easy to devise schemes that nearly conserved lift and affected the loading distribution near the tip, where most of the vorticity was shed. It was found that MiTE configurations with only 13% of the span actuated down could still effect significant changes in the loading distribution of the wing near the tip. The maximum difference in total lift between these configurations was less than 1%.

6.1.2 Near Wake Effects

We conducted a survey of the near wake, where the vortex was still rolling up, in order to study the mechanism responsible for vortex control. Many active flow control techniques involve using control inputs at some “tickle point” on the given geometry in order to cause maximum flow response with minimal input. Such techniques rely upon manipulating unstable aspects of the flow such as streamwise or spanwise separation. The near wake study we performed proved that this was not the case for MiTEs. First, in considering several small actuation ratio cases, it was shown that the MiTEs did not alter the origin of the vortex, i.e., immediately downstream of the wing, the vortex was hardly affected by the MiTEs. Second, we compared results from two positions in the near wake: one immediately behind the wing and one slightly further downstream. It was clear that the effect of the MiTEs on the location of the vortex grew as we proceeded downstream.

Since all devices that generate lift also generate vorticity, it had long been hypothesized that a partial span Gurney flap would shed its own trailing vortices at its inboard and outboard edges. To our knowledge, these secondary structures had never been measured. In our near wake surveys, we presented the first experimental evidence of these structures. It was shown that even though the increment in the loading distribution due to a small actuation ratio MiTE configuration was smooth, a very small counter-rotating vortex pair still occurred at the flap tips then was advected by the strong mean flow due to the primary trailing vortex.

6.1.3 Intermediate Wake Effects

In the intermediate wake, we examined the effects that the MiTEs had on the vortex at three downstream locations after it had essentially rolled up. First, we noted that as we proceeded further downstream (within the intermediate wake) the displacement of the

vortex due to the flaps grew slightly. This confirmed that the effect of the MiTEs upon the vortex was a lasting and reliable change.

Second, considering only the furthest streamwise location, we saw that small actuation ratio MiTE configurations allowed significant control authority over the spanwise and lift locations of the trailing vortex. Two schemes were identified that were likely to be good for wake alleviation: one with a peak-to-peak vortex spanwise displacement of $4.1\%c$ and no lift direction displacement, and another with a spanwise displacement of $3.0\%c$ and a lift direction displacement of $1.7\%c$. Both schemes conserved lift to within 1% of the total. We noted also that apart from the changes in the location of the vortex, it was not modified. The tangential and streamwise velocity distributions as well as the amount of vortex wandering were essentially unaffected by the MiTEs.

Finally, we examined the transient response of the vortex to MiTE actuation. These results were primarily for deriving an experimentally based set of initial conditions for computations of the far wake. They also demonstrated that the transient response of the trailing vortex to MiTE actuation was quasi-steady with respect to the longer input timescales, but not with respect to the shorter input timescales. The flow seemed to moderately smooth out short timescale fluctuations in the motion of the MiTEs. In previous work on the unsteady flow response due to MiTE actuation, it was found that for fast actuation times, there was an overshoot in the local downwash immediately behind the flap implying a transient overshoot of the lift increment caused by the MiTEs. No overshoot in the displacement of the vortex center was observed. This suggested that the transient flow mechanisms responsible for each phenomenon tended to be independent.

6.1.4 Far Wake Effects

The ultimate objective of this work was to determine whether or not the trailing vortex perturbations created by MiTEs could be used to excite vortex instability. Thus, we used the experimental results to derive a complete set of initial conditions for vortex filament computations of the far wake evolution using different vortex configurations.

The model scale and two full scale configurations were examined. The model scale results were encouraging in that they confirmed that Crow instability could be easily excited using MiTE perturbations. Next, full scale configurations involving systems of four vortices (two counter-rotating pairs) were considered. With the first configuration (2PCR), we demonstrated that while perturbing only the outboard vortex pair, both the long wavelength

and symmetric short wavelength instabilities of Crouch could be excited. Examining the second configuration (2PCTR), we highlighted an extremely important issue with regard to wake alleviation. For this configuration, it was shown that short timescales present in the motion of the vortex resulted in premature linking of the weaker inboard pair before the strong outboard pair had become very perturbed. Thus, short timescales could have an adverse effect on the evolution of certain instability modes.

Although these filament computations were no substitute for high accuracy Navier-Stokes computations, well-designed tow tank experiments, or flight tests, they suggested that MiTE-based perturbations could be used for exciting a variety of vortex instabilities. Thus, we concluded that MiTEs have serious potential as an aerodynamic solution to the wake vortex hazard.

6.1.5 Spanwise Actuating Gurney Flap

One of the most important results of this work was that in order to significantly perturb a trailing vortex in a manner that would lead to vortex instability without significant changes to the total lift, only 13% of the span needed to be actuated and only near the wing tip. This result naturally led to the invention of the spanwise actuating Gurney flap, a novel aerodynamic device designed specifically to create these types of vortex perturbations. This device had the advantages that it was simple to control, involved few moving parts, and could probably be added to existing aircraft. Thus, it constituted a more realistic, more easily implementable device for active wake alleviation.

Some intermediate wake experiments were performed on the same wing equipped with a spanwise actuating Gurney flap, and the results were encouraging. They demonstrated similar trends to the MiTEs in terms of which directions the vortex could be perturbed. The maximum spanwise vortex displacement was smaller than that of the MiTEs. However, it could likely be increased by simply increasing the height of the flap.

6.2 Recommendations

More research will be necessary to completely prove the capabilities and viability of MiTEs or spanwise actuating Gurney flaps for active wake alleviation as well as to determine the optimal way to implement them on actual aircraft. Issues that will need to be addressed are listed as follows. All of these issues apply both to MiTEs as well as spanwise actuating

Gurney flaps. We will refer to them collectively as GF-type devices.

- A three-dimensional shape optimization study to determine the best design for the GF-type device has yet to be performed and would be crucial for making the most effective actuators while minimizing any negative impact on wing aerodynamics. This study should determine the best size, location, and shape of the flap to maximize the effectiveness. Varying these parameters in the spanwise direction should also be considered. Such a study could result in design improvements allowing increased vortex displacement with perfect conservation of lift. The study should be performed on a multi-element wing more representative of an actual aircraft wing.
- GF-type devices would likely be deployed only during take-off and landing, when aircraft noise is a major concern. The sharp corners on most actuators might add to this problem. A study of the acoustics associated with these devices could lead to designs that minimize the noise.
- The computational results from this work demonstrated that we could simultaneously excite both long and short wavelength inviscid instabilities on multiple-pair vortex configurations using control inputs containing a variety of timescales. Such multi-wavelength strategies would likely result in more benign wakes within a shorter amount of time than exciting each wavelength separately. Research on using control inputs containing several unstable wavelengths could reveal optimal inputs that promote the most benign wakes.
- High accuracy experimental and computational investigations of the far wakes of aircraft with perturbations from GF-type devices embedded in them will be necessary to determine exactly how much spacing rules can be modified with no decrease in the level of safety. These studies will need to account for realistic airport conditions and variable atmospheric effects. Issues such as ground effect, wind, atmospheric turbulence, and thermal currents will need to be addressed. Such studies pose formidable challenges given current experimental and computational capabilities.

6.3 Closing Remarks

This work, in and of itself, does not constitute a complete solution to the wake vortex hazard. Rather, this work combines several new and old concepts to demonstrate that rapidly actuated segmented Gurney flaps have serious potential for providing an aerodynamic solution to the wake vortex hazard. Further research, as discussed above, will be necessary before these devices can be implemented on aircraft.

In recent years and at the time of this writing, much of the work being done in the wake vortex community has been aimed at detection and avoidance rather than wake alleviation. Although detection and avoidance techniques are a legitimate way of handling the problem, we believe that the wake alleviation strategies studied by ourselves and others in recent years are preferable solutions and should be pursued further. First, wake alleviation techniques attack the wake vortex hazard directly rather than attempt to avoid it if conditions allow. Thus, if an alleviation technique works properly, there would never be an instance when aircraft would have to wait for one another; worst case scenarios are mitigated. Second, although vortex detection techniques have made marked improvements since the first attempts, there are still difficulties in using them when there is poor visibility. This is when IFR conditions are in place, the most critical time for any technique to work well. Wake alleviation techniques are completely insensitive to visibility conditions. Finally, detection and avoidance techniques are typically ground-based. Thus, they are inherently limited in range, whereas wake alleviation techniques are not. For these reasons and others, we believe that wake alleviation remains the best hope for solving the wake vortex hazard problem.

Appendix A

Calibration of Five-Hole Probe

The five-hole probe was calibrated and applied using the same method outlined by Treaster and Yocum (1979). A two-dimensional calibration was necessary due to the high tangential velocities in the flow. We calibrated the probe at one Reynolds number close to running conditions.

A circular jet which had been previously constructed for calibrating similar probes was modified to facilitate this calibration. A schematic of the jet is shown in Fig. A.1. It had roughly a 6.4:1 area ratio contraction. The tip of the probe was placed roughly half of the jet diameter downstream of the exit. As shown in Fig. A.2, the pitch and yaw angles were defined such that changes in pitch corresponded to Y -component velocities and changes in yaw corresponded to Z -component velocities (in the tunnel coordinate system). The pressures before and after the contraction (p_{j1} and p_{j2}) were measured during calibration via pressure taps before and after the contraction. The pressures at each hole in the probe (p_1 , p_2 , p_3 , p_4 , and p_5) were also measured simultaneously. The locations of the holes on the probe are shown in Fig. A.2.

A picture of the calibration jet with the probe mounted in it is shown in Fig. A.3. The stem was supported by two aluminum plain bearings mounted on an aluminum block allowing the probe stem to rotate about its axis. Yaw angle, β , was varied using a brass dial secured to the probe stem with tick marks at 5° increments. The dial could lock into place at each increment using a stationary alignment pin on the bearing beneath the dial that fit into precisely placed holes along the bottom of the dial. The pitch angle was varied by altering the position of the aluminum block. Two alignment pins on the bottom of the block fit into precisely placed holes on an acrylic plate that was secured to the jet.

All measurements were referenced using p_{j1} as the high pressure. The six measured quantities were thus

$$\Delta p_i = p_{j1} - p_i, \quad i = 1, 2, 3, 4, 5, \quad (\text{A.1})$$

$$\Delta p_{j2} = p_{j1} - p_{j2}. \quad (\text{A.2})$$

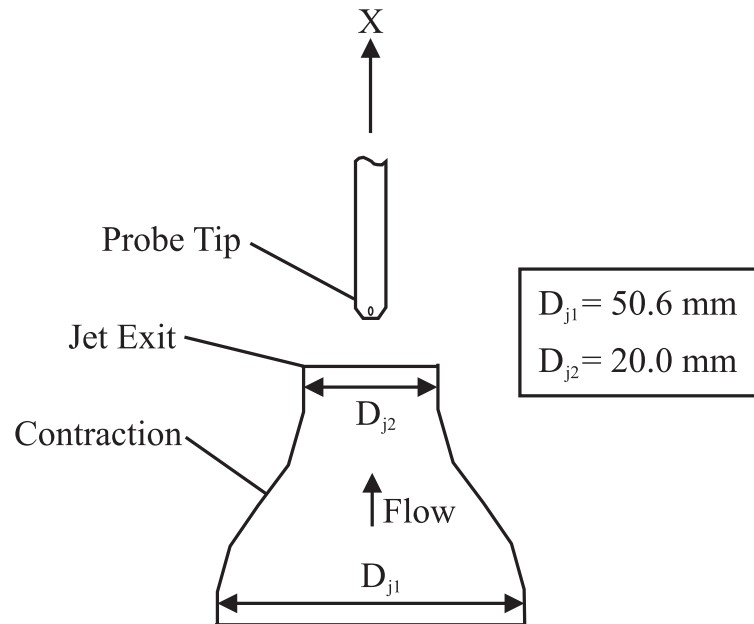


Fig. A.1. A schematic of the calibration jet used for five-hole probe calibration.

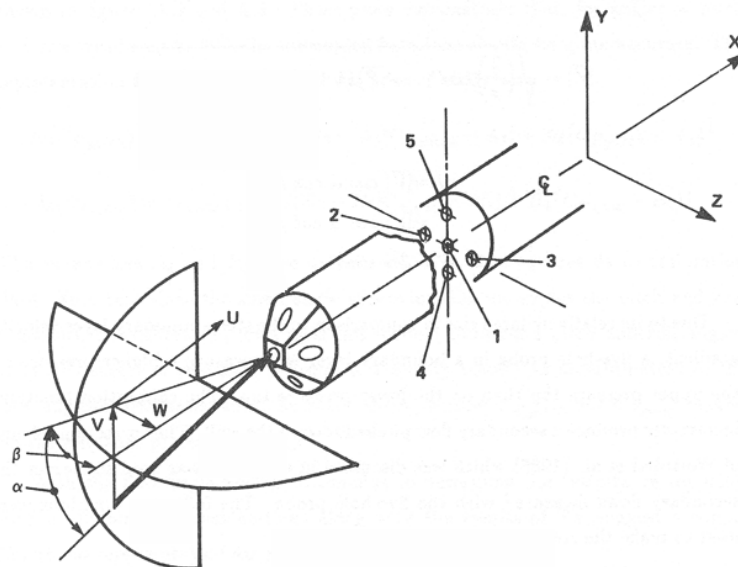


Fig. A.2. A schematic of the five-hole probe orientation and hole locations. Figure taken from Pauley (1988).

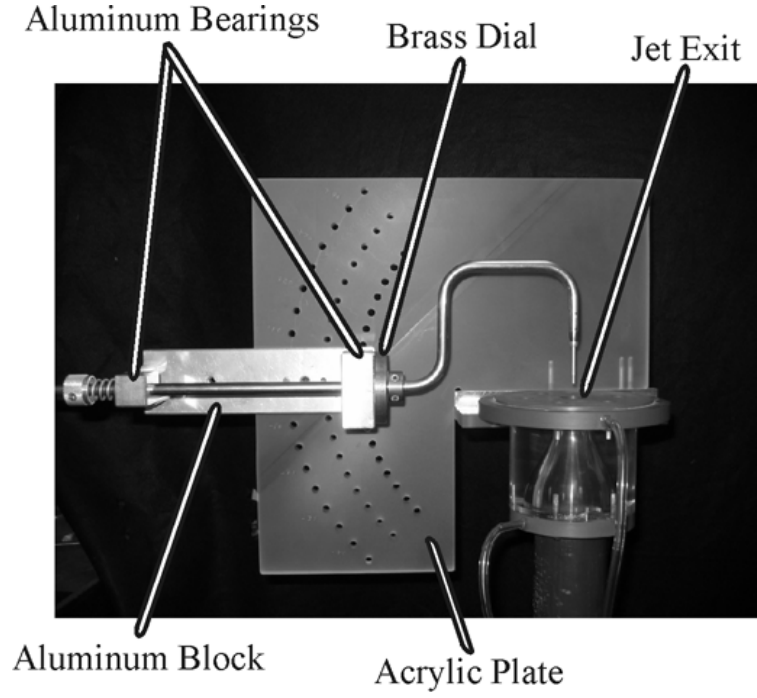


Fig. A.3. A picture of the five-hole probe mounted on the calibration jet.

The nondimensional pressure coefficients as defined by Treaster and Yocum can be calculated in terms of these measured quantities by

$$\begin{aligned}
 C_{p_{yaw}} &= \frac{\Delta p_3 - \Delta p_2}{\overline{\Delta p}} - \Delta p_1, \\
 C_{p_{pitch}} &= \frac{\Delta p_5 - \Delta p_4}{\overline{\Delta p}} - \Delta p_1, \\
 C_{p_{static}} &= \frac{\Delta p_{j2} - \overline{\Delta p}}{\overline{\Delta p}} - \Delta p_1, \\
 C_{p_{total}} &= \frac{\Delta p_{j2} - \Delta p_1 - \frac{\Delta p_{j2}}{1 - \left(\frac{A_{j2}}{A_{j1}}\right)}}{\overline{\Delta p}} - \Delta p_1, \\
 \overline{\Delta p} &= \frac{\Delta p_2 + \Delta p_3 + \Delta p_4 + \Delta p_5}{4}.
 \end{aligned} \tag{A.3}$$

Note that the equation for $C_{p_{total}}$ is complicated by the fact that p_{j2} is not the stagnation

pressure of the jet. Thus, additional terms appeared in this equation that did not appear in the same equation given by Treaster and Yocum.

We used 81 calibration points: α and β were varied independently between -40° and $+40^\circ$ in 10° increments. The calibration data are shown in Figs. A.5-A.8. The calibration was done several times to verify its repeatability. Differences were well within uncertainty. All data collection software was written in Labview, and all data processing software was written in Matlab.

The method used for translating pressure coefficients into velocities was very similar to the method described by Treaster and Yocum. We relied heavily upon cubic spline interpolation using the 'griddata' function built into Matlab. The basic process is outlined in Fig. A.4 and described as follows. Note that for the calibration data, it was possible to measure all four pressure coefficients because the dynamic pressure of the jet could be measured, but when taking data, we could only measure p_1 - p_5 , thus, there was no way to calculate $C_{p_{static}}$ or $C_{p_{total}}$. After collecting the data, the first step was to calculate $C_{p_{pitch}}$ and $C_{p_{yaw}}$. Then, using the calibration data of Figs. A.5 and A.6 and the 'griddata' function, we determined α and β . Next, using α and β with the calibration data of Figs. A.7 and A.8, we determined $C_{p_{static}}$ and $C_{p_{total}}$. Using these coefficients, we determined the dynamic pressure, and thus the velocity magnitude. Finally, having determined the pitch angle, yaw angle, and velocity magnitude, we calculated all three components of velocity using basic geometrical relations.

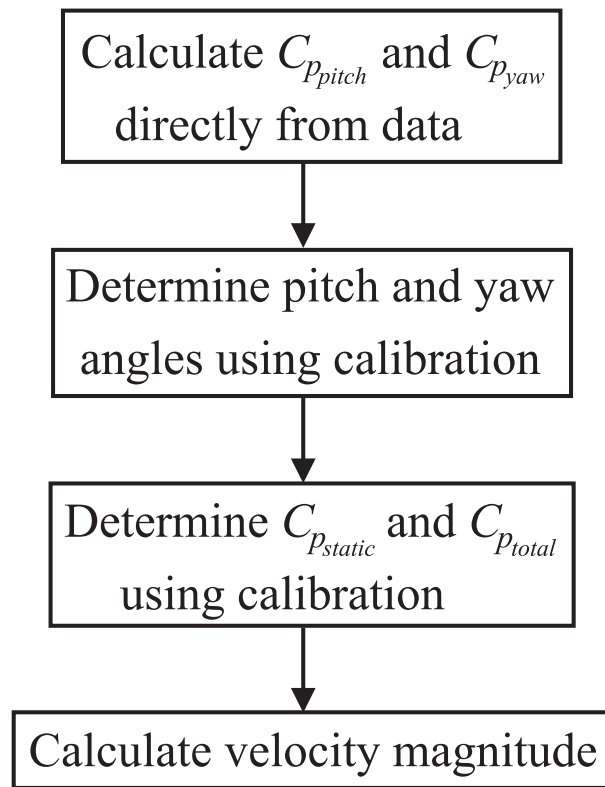


Fig. A.4. An outline of the method used to process raw five-hole probe data to derive velocity measurements.

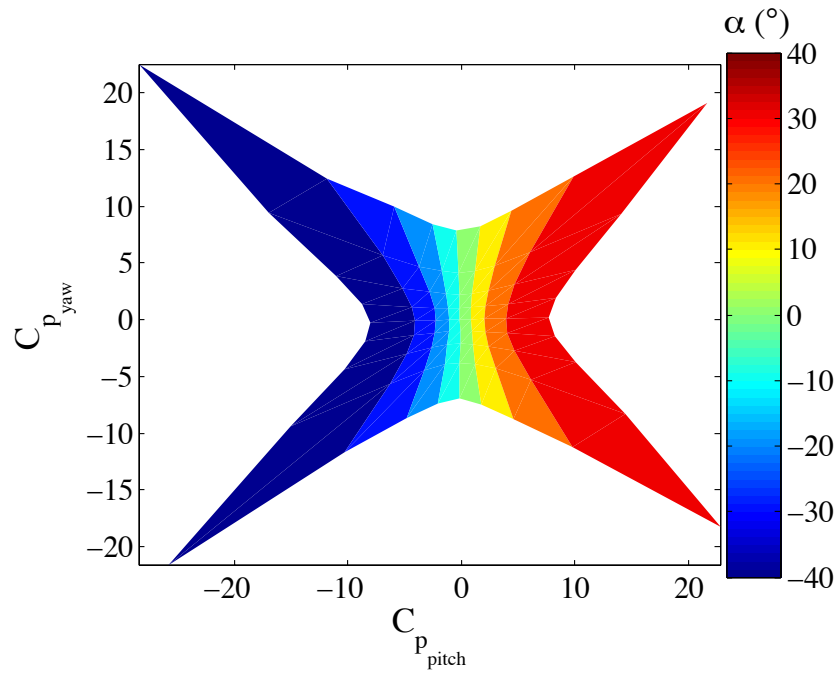


Fig. A.5. Calibration data for determining pitch angle.

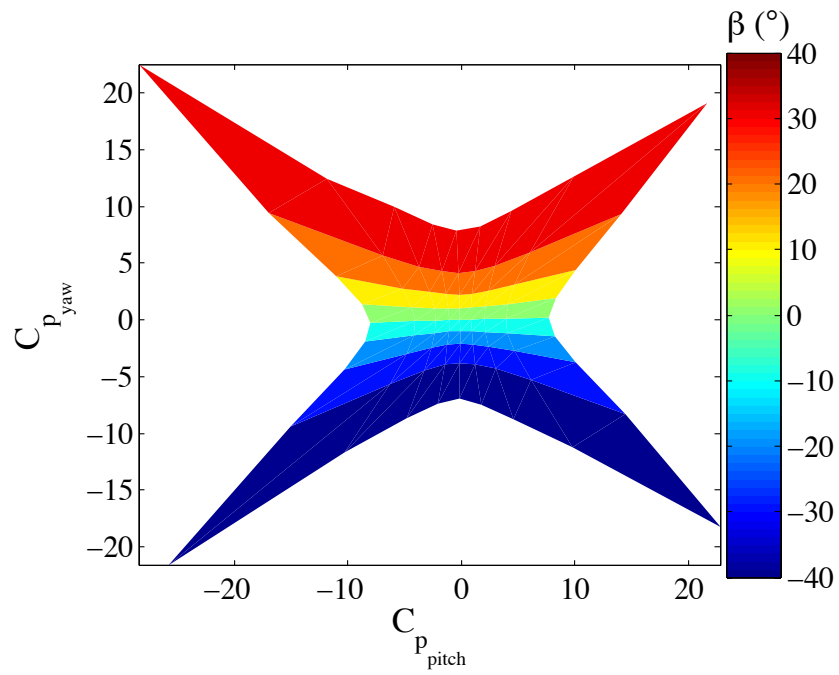


Fig. A.6. Calibration data for determining yaw angle.

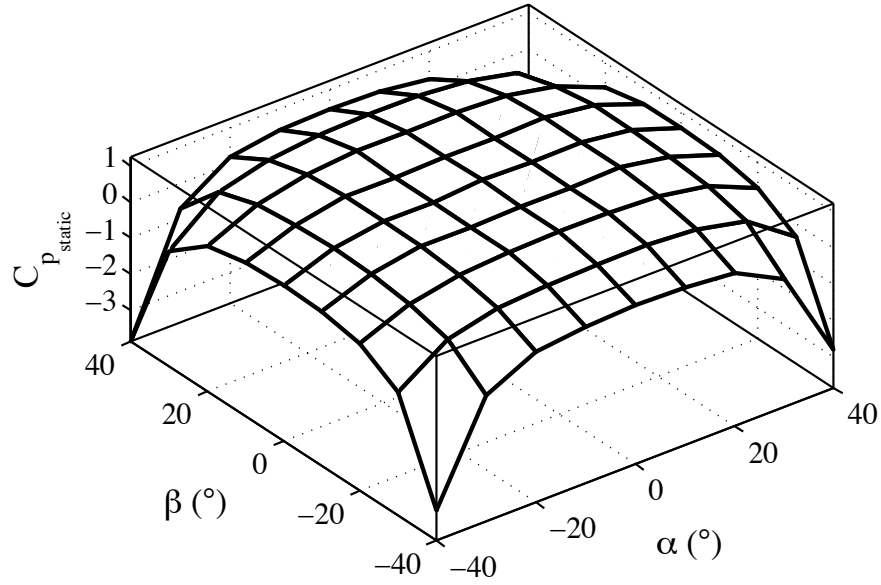


Fig. A.7. Calibration data for determining static pressure coefficient.

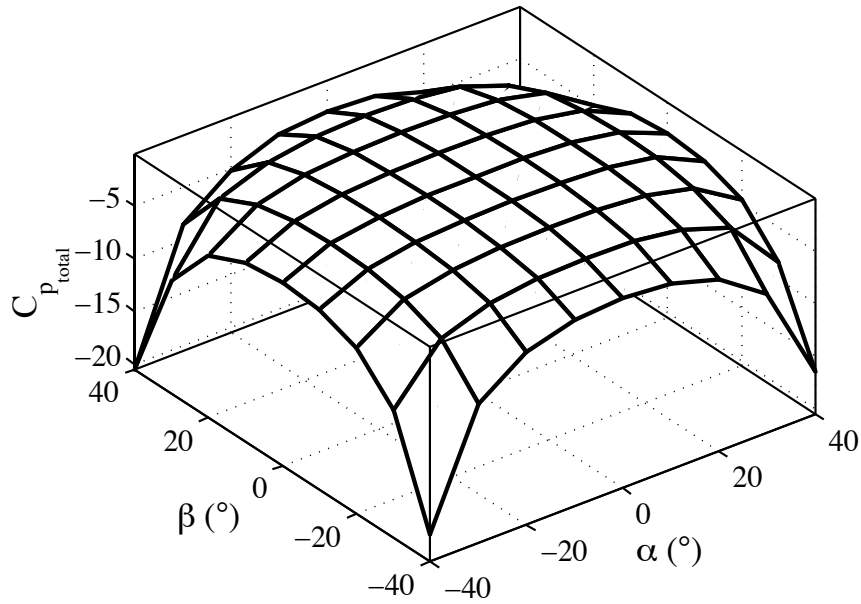


Fig. A.8. Calibration data for determining total pressure coefficient.

Appendix B

Camera Upstream Effect

We conducted a brief study to verify that the presence of the camera box in the tunnel would not have a significant effect on the flow at the PIV measurement plane. A two-dimensional potential flow simulation was performed.

Flow through the wind tunnel test section with only the camera inside was considered. Since the tunnel was longer in the Y -direction than it was in the Z -direction, the blockage due to the camera was greater in the XZ plane than it was in the XY plane. Thus, to be conservative, we performed a two-dimensional simulation of the flow in the XZ plane. We modeled the flow from the entrance of the wind tunnel to just behind the front surface of the camera box. The geometry is shown in Fig. B.1.

For potential flow, we were simply solving Laplace's equation,

$$\nabla^2 \phi = 0, \tag{B.1}$$

where ϕ was the velocity potential function. The boundary conditions were assigned as follows. The side walls of the tunnel and the camera box were considered impermeable boundaries. At the inlet we had uniform flow moving at the freestream velocity, and at the flow exit, the velocity potential function was set to an arbitrary constant.

The simulation was performed using the PDE toolbox in Matlab. This allowed for fast grid generation, solution, and post-processing. In Fig. B.2, we show contours of streamwise velocity. Qualitatively, it was clear that the region upstream of the camera that was affected by the camera was small. In Figs. B.3 and B.4 we show the velocity profiles at the measurement location. Clearly, the flow is essentially uniform. Deviations from freestream conditions were less than 0.1% of the freestream velocity.

To confirm the results of this analysis, we also performed five-hole probe measurements in the intermediate wake both with and without the camera box in the tunnel. This was done with the wing in the tunnel. The results were within uncertainty to one another, confirming that the camera box had no measurable effect on the PIV results.

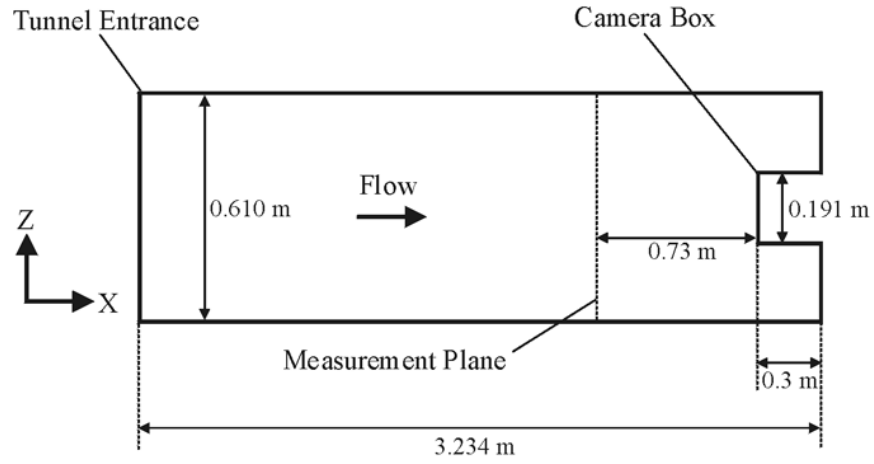
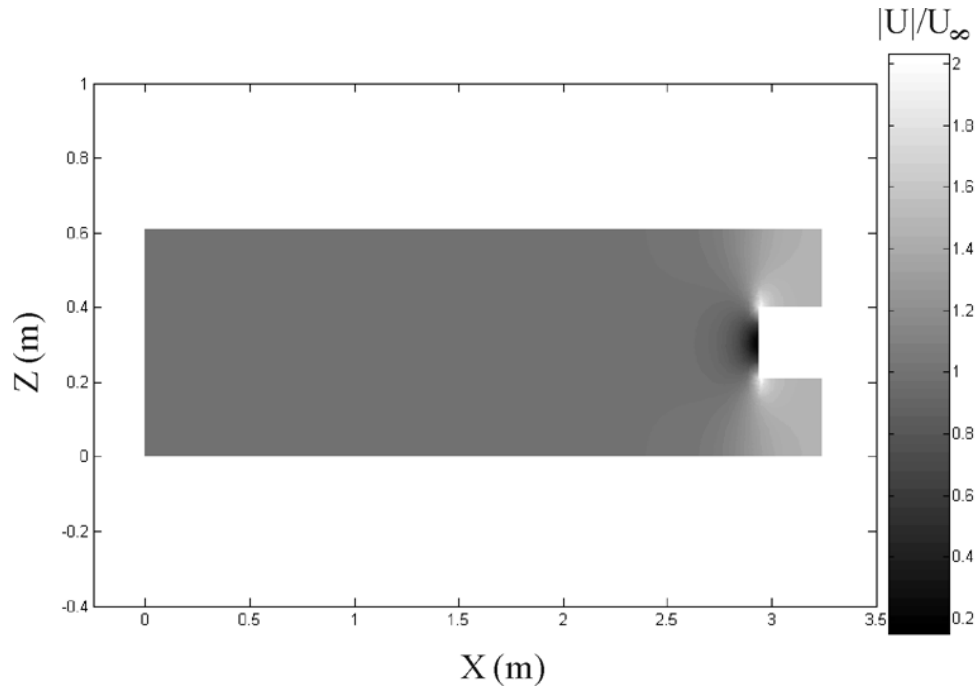


Fig. B.1. A schematic representation of the modeled geometry.

Fig. B.2. Contours of velocity magnitude in the XZ plane.

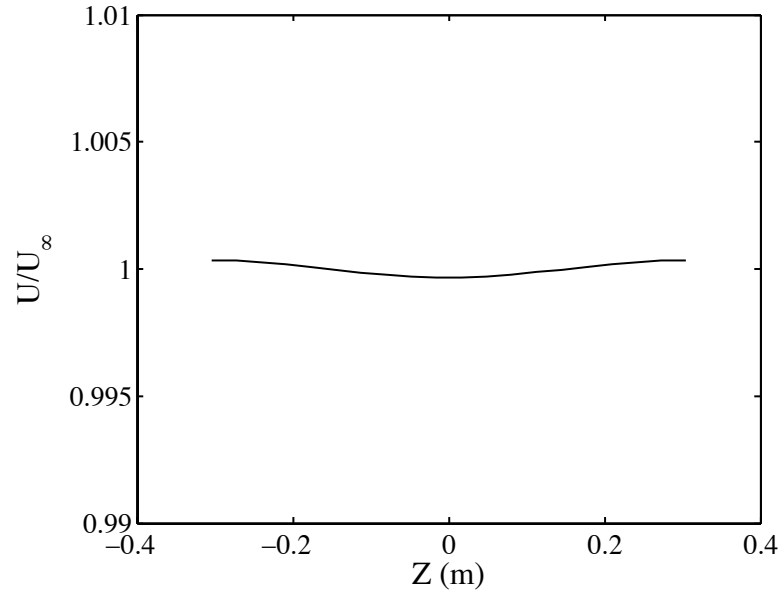


Fig. B.3. Streamwise velocity profile at the measurement plane.

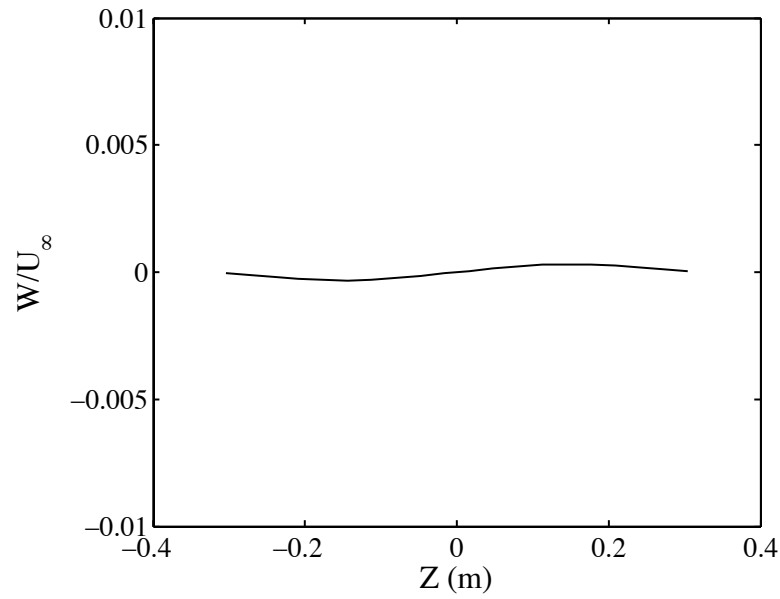


Fig. B.4. Lift direction velocity profile at the measurement plane.

References

- Barber, M. R. and J. J. Tymczyszyn (1980). Wake Vortex Attenuation Flight Tests: A Status Report. NASA CP-2170.
- Bearman, P., A. Heyes, C. Lear, and D. Smith (2006). Natural and Forced Evolution of a Counter Rotating Vortex Pair. *Experiments in Fluids* 40(1), 98–105.
- Bilanin, A. J. and S. E. Widnall (1973). Aircraft Wake Dissipation by Sinusoidal Instability and Vortex Breakdown. AIAA Paper 73–107.
- Boluriaan, S. and P. J. Morris (2001). Numerical Simulation of Wake Vortex Detection Using a Radio Acoustic Sounding System. *AIAA Journal* 39(6), 1097–1105.
- Boluriaan, S. and P. J. Morris (2002). Two-Dimensional Simulations of Wake Vortex Detection Using Radio Acoustic Sounding Systems. *AIAA Journal* 40(11), 2247–2256.
- Chambers, J. R. (2003). Concept to Reality: Contributions of the Langley Research Center to U.S. Civil Aircraft of the 1990s. NASA SP-2003-4529.
- Chevalier, H. (1973). Flight Test Studies of the Formation and Dissipation of Trailing Vortices. *Journal of Aircraft* 10(1), 14–18.
- Chow, J. (1997). *Turbulence Measurements in the Near Field of a Wingtip Vortex*. Ph. D. thesis, Stanford University.
- Compton, D. A. (1995). *Near-Wall Measurements of a Three-Dimensional Turbulent Boundary Layer*. Ph. D. thesis, Stanford University.
- Corsiglia, V. R. and R. E. Dunham Jr. (1976). Aircraft Wake-Vortex Minimization by Use of Flaps. In *Wake Vortex Minimization* SP-409.
- Croom, D. R. (1977). Evaluation of Flight Spoilers for Vortex Alleviation. *Journal of Aircraft* 14(8), 823–825.
- Crouch, J. D. (1997). Instability and Transient Growth for Two Trailing-Vortex Pairs. *Journal of Fluid Mechanics* 350, 311–330.
- Crouch, J. D., G. D. Miller, and P. R. Spalart (2001). Active-Control System for Breakup of Airplane Trailing Vortices. *AIAA Journal* 39(12), 2374–2381.

- Crow, S. C. (1970). Stability Theory for a Pair of Trailing Vortices. *AIAA Journal* 8(12), 2172–2179.
- Crow, S. C. and E. R. Bate Jr. (1976). Lifespan of Trailing Vortices in a Turbulent Atmosphere. *Journal of Aircraft* 13(7), 476–482.
- Durstun, D. A., S. M. Walker, D. M. Driver, and S. C. Smith (2005). Wake-Vortex Alleviation Flowfield Studies. *Journal of Aircraft* 42(4), 894–907.
- Fabre, D. and L. Jacquin (2000). Stability of a Four-Vortex Aircraft Wake Model. *Physics of Fluids* 12(10), 2438–2443.
- Fabre, D. and L. Jacquin (2004). Short-Wave Cooperative Instabilities in Representative Aircraft Vortices. *Physics of Fluids* 16(5), 1366–1378.
- Fabre, D., L. Jacquin, and A. Loof (2002). Optimal Perturbations in a Four-Vortex Aircraft Wake in Counter-Rotating Configuration. *Journal of Fluid Mechanics* 451, 319–328.
- Figliola, R. S. and D. E. Beasley (1995). *Theory and Design for Mechanical Measurements*. John Wiley & Sons, Inc.
- Gerz, T., F. Holzäpfel, and D. Darracq (2002). Commercial Aircraft Wake Vortices. *Progress in Aerospace Sciences* 38, 181–208.
- Giguère, P., J. Lemay, and G. Dumas (1995). Gurney Flap Effects and Scaling for Low Speed Airfoils. AIAA Paper 95-1881-CP.
- Graham, W. R., S.-W. Park, and T. B. Nickels (2003). Trailing Vortices from a Wing with a Notched Lift Distribution. *AIAA Journal* 41(9), 1835–1838.
- Greenblatt, D., L. G. Pack-Melton, C.-S. Yao, and J. Harris (2005). Active Control of a Wing Tip Vortex. AIAA Paper 2005-4851.
- Han, D. (2001). *Study of Turbulent Nonpremixed Jet Flames Using Simultaneous Measurements of Velocity and CH Distribution*. Ph. D. thesis, Stanford University.
- Hannon, S. M. and J. A. Thomson (1994). Aircraft Wake Vortex Detection and Measurement with Pulsed Solid-State Coherent Laser Radar. *Journal of Modern Optics* 41(11), 2175–2196.
- Harris, M., R. I. Young, F. Köpp, A. Dolfi, and J.-P. Cariou (2002). Wake Vortex Detection and Monitoring. *Aerospace Science and Technology* 6, 325–331.

- Haverkamp, S., G. Neuwerth, and D. Jacob (2003). Studies on the Influence of Outboard Flaps on the Vortex Wake of a Rectangular Wing. *Aerospace Science and Technology* 7, 331–339.
- Haverkamp, S., G. Neuwerth, and D. Jacob (2005). Active and Passive Wake Mitigation Using Control Surfaces. *Aerospace Science and Technology* 9, 5–18.
- Heyes, A. L. and D. A. R. Smith (2004). Spatial Perturbations of a Wing-tip Vortex Using Pulsed Span-wise Jets. *Experiments in Fluids* 37(1), 120–127.
- Heyes, A. L. and D. A. R. Smith (2005). Modification of a Wing Tip Vortex by Vortex Generators. *Aerospace Science and Technology* 9, 469–475.
- Hinton, D. A. (1996). An Aircraft Vortex Spacing System (AVOSS) for Dynamical Wake Vortex Spacing Criteria. In *The Characterisation and Modification of Wakes from Lifting Vehicles in Fluid* AGARD CP-584.
- Holbrook, G. T., D. M. Dunham, and G. C. Greene (1985). Vortex Wake Alleviation Studies With a Variable Twist Wing. NASA TP 2442.
- Huffaker, R. M., A. V. Jelalian, and J. A. L. Thomson (1970). Laser-Doppler System for Detection of Aircraft Trailing Vortices. *Proceedings of the IEEE* 58(3), 322–326.
- Jacobs, E. N. and A. Sherman (1937). Airfoil Section Characteristics as Affected by Variations of the Reynolds Number. NACA 586.
- Jeffrey, D. R. M. and D. W. Hurst (1996). Aerodynamics of the Gurney Flap. AIAA Paper 96-2418-CP.
- Jordan, F. L. J. (1983). Flow Visualization of the Wake of a Transport Aircraft Model With Lateral-Control Oscillations. NASA TM-84623.
- Keane, M., D. Buckton, and M. Redfern (2002). Axial Detection of Aircraft Wake Vortices Using Doppler Lidar. *Journal of Aircraft* 39(5), 850–861.
- Khorrami, M. R. (1991). On the Viscous Modes of the Instability of a Trailing Line Vortex. *Journal of Fluid Mechanics* 225, 197–212.
- Laporte, F. and A. Corjon (2000, May). Direct Numerical Simulations of the Elliptic Instability of a Vortex Pair. *Physics of Fluids* 12(5), 1016–1031.
- Leonard, A. (1980). Vortex Methods for Flow Simulation. *Journal of Computational Physics* 37, 289–335.

- Leonard, A. (1985). Computing Three-Dimensional Flows with Vortex Elements. *Journal of Computational Physics* 17, 523–559.
- Leweke, T. and C. H. K. Williamson (1998). Cooperative Elliptic Instability of a Vortex Pair. *Journal of Fluid Mechanics* 360, 85–119.
- Lezius, D. K. (1975). Unstable Wing Vortex Rollup Induced by Lift Tailoring in the Wing-Tip Region. In *Proceedings of the Aircraft Wake Vortices Conference - Vol. 1* DOT/FAA/SD-92/1.1.
- Mack, G. R. (1996). Wake Vortices' Effects and the Need for Prompt Action—A U.S. View. In *The Characterisation and Modification of Wakes from Lifting Vehicles in Fluid* AGARD CP-584.
- Myose, R., M. Papadakis, and I. Heron (1998). Gurney Flap Experiments on Airfoils, Wings, and Reflection Plane Model. *Journal of Aircraft* 35(2), 206–211.
- Orlandi, P., G. F. Carnevale, S. K. Lele, and K. Shariff (1998). DNS study of Stability of Trailing Vortices. Center for Turbulence Research Proceedings of the Summer Program.
- Orlandi, P., G. F. Carnevale, S. K. Lele, and K. Shariff (2001). Thermal Perturbation of Trailing Vortices. *European Journal of Mechanics B - Fluids* 20, 511–524.
- Ortega, J. M., R. L. Bristol, and Ö. Savas (2002). Wake Alleviation Properties of Triangular-Flapped Wings. *AIAA Journal* 40(4), 709–721.
- Ortega, J. M., R. L. Bristol, and Ö. Savas (2003). Experimental Study of the Instability of Unequal-Strength Counter-Rotating Vortex Pairs. *Journal of Fluid Mechanics* 474, 35–84.
- Özger, E., I. Schell, and D. Jacob (2001). On the Structure and Attenuation of an Aircraft Wake. *Journal of Aircraft* 38(5), 878–887.
- Park, B. (2002). *Miniaturization of Functional Mechanisms with SDM Processing*. Ph. D. thesis, Stanford University, Stanford, CA.
- Patterson, J. C. (1975). Vortex Attenuation Obtained in the Langley Vortex Research Facility. *Journal of Aircraft* 12(9), 745–749.
- Pauley, W. R. (1988). *Fluid Dynamics and Heat Transfer Effects of Streamwise Vortices embedded in a Turbulent Boundary Layer*. Ph. D. thesis, Stanford University.

- Raffel, M., C. E. Willert, and J. Kompenhans (1998). *Particle Image Velocimetry: A Practical Guide*. Springer.
- Rebours, R., L. K. Kliment, and K. Rokhsaz (2004). Forced Response of a Vortex Filament Pair Measured in a Water Tunnel. *Journal of Aircraft* 41(5), 1163–1168.
- Rennich, S. C. (1997). *Accelerated Destruction of Aircraft Wake Vortices*. Ph. D. thesis, Stanford University, Stanford, CA.
- Rennich, S. C. and S. K. Lele (1999). Method for Accelerating the Destruction of Aircraft Wake Vortices. *Journal of Aircraft* 36(2), 398–404.
- Rossow, V. J. (1975). Theoretical Study of Lift Generated Vortex Wakes Designed to Avoid Rollup. *AIAA Journal* 13(4), 476–484.
- Rossow, V. J. (1977). Convective Merging of Vortex Cores in Lift-Generated Wakes. *Journal of Aircraft* 14(3), 283–290.
- Rossow, V. J. (1978). Effect of Wing Fins of Lift-Generated Wakes. *Journal of Aircraft* 15(3), 160–167.
- Rossow, V. J. (1986). Wake Hazard Alleviation Associated with Roll Oscillations of Wake-Generating Aircraft. *Journal of Aircraft* 23(6), 484–491.
- Rossow, V. J. (1987). Prospects for Destructive Self-Induced Interactions in a Vortex Pair. *Journal of Aircraft* 24(7), 433–440.
- Rossow, V. J. (1999). Lift-Generated Vortex Wakes of Subsonic Transport Aircraft. *Progress in Aerospace Sciences* 35, 507–660.
- Roth, G. I. and J. Katz (2001). Five Techniques for Increasing the Speed and Accuracy of PIV interrogation. *Measurement Science and Technology* 12, 238–245.
- Rubin, W. L. (2000). Radar-Acoustic Detection of Aircraft Wake Vortices. *Journal of Atmospheric and Oceanic Technology* 17, 1058–1065.
- Rubin, W. L., D. C. Burnham, E. A. Spitzer, and R. P. Rudis (2000). Robust Low Cost Airport Wake Vortex Sensor. *Journal of Aircraft* 37(3), 377–382.
- Schell, I., E. Özger, and D. Jacob (2000). Influence of Different Flap Settings on the Wake-Vortex Structure of a Rectangular Wing with Flaps and Means of Alleviation with Wing Fins. *Aerospace Science and Technology* 4, 79–90.

- Schöll, R. H., C. Buxel, and G. Neuwerth (2006). Influence of Spanwise Loading and Fins on Extended Near-Field Vortex Wake. AIAA Paper 2006-62.
- Shariff, K. and A. Wray (2002). Analysis of the Radar Reflectivity of Aircraft Vortex Wakes. *Journal of Fluid Mechanics* 463, 121–161.
- Simpson, R. G., N. A. Ahmed, and R. D. Archer (2002). Near Field Study of Vortex Attenuation Using Wing-Tip Blowing. *The Aeronautical Journal*, 117–120.
- Singh, P. I. and M. S. Uberoi (1976). Experiments on Vortex Stability. *Physics of Fluids* 19(12), 1858–1863.
- Solovitz, S. A. (2002). *Experimental Aerodynamics of Mesoscale Trailing-Edge Actuators*. Ph. D. thesis, Stanford University, Stanford, CA.
- Solovitz, S. A. and J. K. Eaton (2004a). Dynamic Flow Response due to Motion of Partial-Span Gurney-type Flaps. *AIAA Journal* 42(9), 1729–1736.
- Solovitz, S. A. and J. K. Eaton (2004b). Spanwise Response Variation for Partial-Span Gurney-Type Flaps. *AIAA Journal* 42(8), 1640–1643.
- Spalart, P. R. (1998). Airplane Trailing Vortices. *Annual Review of Fluid Mechanics* 30, 107–138.
- Spalart, P. R. and A. A. Wray (1996). Initiation of the Crow Instability by Atmospheric Turbulence. In *The Characterisation and Modification of Wakes from Lifting Vehicles in Fluid* AGARD CP-584.
- Spreiter, J. R. and A. H. Sacks (1951). The Rolling Up of the Trailing Vortex Sheet and Its Effect on the Downwash Behind Wings. *Journal of Aeronautical Sciences*, 21–32.
- Stumpf, E. (2004). Numerical Study of Four-Vortex Aircraft Wakes and Layout of corresponding High-Lift Configurations. AIAA Paper 2004-1067.
- Tanaka, S., M. Kaibara, and A. Tanaka (1978). Decay and Modification of Trailing Vortex. *Bulletin of the JSME* 21(151), 98–103.
- Thomas, P. J. and D. Auerbach (1994). The Observation of the Simultaneous Development of a Long- and Short-Wave Instability Mode on a Vortex Pair. *Journal of Fluid Mechanics* 265, 289–302.
- Thomson, J. A. L. and J. C. S. Meng (1976). Scanning Laser Doppler Velocimeter System Simulation for Sensing Aircraft Wake Vortices. *Journal of Aircraft* 13(8), 605–613.

- Traub, L. W., S. Mani, and O. K. Rediniotis (1998). Application of the Vortex Breakdown Phenomenon in the Attenuation of Trailing Vortices. *The Aeronautical Journal* 102, 439–444.
- Treaster, A. L. and A. M. Yocum (1979). The Calibration and Application of Five-hole Probes. *ISA Transactions* 18, 23–34.
- van Dam, C. P. and D. T. Yen (1999). Gurney Flap Experiments on Airfoils and Wings. *Journal of Aircraft* 36(2), 484–486.
- Widnall, S. E. (1975). The Structure and Dynamics of Vortex Filaments. *Annual Review of Fluid Mechanics* 7, 141–165.
- Zhou, Y. and H. J. Zhang (2004). Wing-Tip Vortex Measurement with Particle Image Velocimetry. AIAA Paper 2004-2433.